Semiquinone-Bridged *bis*-Dithiazolyls as Neutral Radical Conductors

by

Xin Yu

A thesis
presented to the University of Waterloo
in fulfillment of the
thesis requirement for the degree of
Master of Science
in
Chemistry

Waterloo, Ontario, Canada, 2011

Author's Declaration

I hereby declare that I am the sole author of this thesis. This is a true copy of the thesis, including any required final revisions, as accepted by my examiners.

I understand that my thesis may be made electronically available to the public.

Abstract:

Radicals are potential building blocks to prepare conductive and magnetic materials. In order to achieve high conductivity, materials displaying a large bandwidth *W* and a low on-site Coulomb repulsion energy *U* must be generated.

Semiquinone-bridged *bis*-1,2,3-dithiazolyl radicals (R = Cl, Ph, Me and the MeCN adduct of R = Cl) represent a new family of resonance stabilized neutral radical for use in the design of single-component conductive materials were prepared and fully characterized. In solid state these radicals remain as unassociated (monomers) in the solid state and typically form superimposed alternating π-stacks or slipped π-stacks, arranged in several different space groups. The predominate intermolecular interactions are S···N′ and / or S···O′ contacts, which increase the dimensionality from one dimensional π-stacked systems (*i.e.,* poor lateral overlap) to two dimensional systems in the solid state. Thus the semiquinone-bridged *bis*-dithiazolyl radicals exhibit a significant decrease in activation energy (*ca.* 0.1 – 0.2 eV) and the conductivity is two to three orders of magnitude (*ca.* $\sigma \approx 10^{-5} - 10^{-2}$ S cm^{-1}) higher in comparison to the previously reported pyridine based systems. This high conductivity is attributed to the low on-site Coulomb repulsion energies (*U*) which were estimated from the solution cell potentials (E_{PC}) obtained from CV measurements and improved bandwidth (*W*) from the S···N′ and / or S···O′ interactions. Furthermore, the all sulphur containing semiquinone-bridged *bis*-dithiazolyls have the lowest activation energies and the highest conductivity under ambient conditions compared with other all sulfur nitrogen based radicals known to date.

The semiquinone-bridged *bis*-dithiazolyl (R = Cl) orderes as spin-canted antiferromagnets, $T_N = 8$ K, and displayed large coercivity (80 Oe). The ZFC-FC measurement at low field (*i.e., H* = 100 Oe)

established the phase transition temperatures and the spontaneous magnetization was used to estimate the spin canting angles (~ 0.14°). In the case of R = Ph, the antiparallel alignment of the ferromagnetic coupled chains leads to a spin-canted antiferromagnet (T_N = 4.5 K), which undergo a unique field induced spin flop transition. The MeCN solvated of R = Cl behaves as a simple paramagnet at room temperature with bulk antiferromagnetic interactions, but no observed magnetic ordering from 2-300 K.

Acknowledgments

I would like to take this opportunity to thank all the people who helped me get to where I am today. First and foremost I would like to thank Dr. Richard Oakley who gave me the opportunity to join his research group as a new graduate student. Thank you for your supervision and all the help, support and encouragement you have provided during my stay in Waterloo. Furthermore, I am really grateful for all the knowledge I have obtained and the skills that I have developed here, which I am sure will benefit me throughout my career in chemistry in the future.

I would also like to thank all of the Oakley group members for their help during my M.Sc. program and your kindness has made my life here much more enjoyable. I am grateful to Dr. Aaron Mailman for his assistance and help during my M.Sc. project. The knowledge and help you brought to the team really made my research much more enjoyable and certainly made the work go more smoothly.

I would also like to thank all of the Kleinke group members, especially to Dr. Raj Sankar for his help with the conductivity measurements and powder crystallography, as well as Dr. Jalil Assoud, Dr. Craig Robertson, Dr. Charles Campana and Dr. Bruce Noll for single X-ray crystallography; Dr. Richard Smith for mass spectrometry; and Dr. Paul Dube for all the magnetic measurements. I would also like to extend my gratitude to my committee members: Dr. Holger Kleinke and Dr. Sonny Lee for all their help along the way.

Last but not least, I am especially grateful to my family for all your support during my studies in Canada during past 8 years. Without your support I probably would have given up studying in Canada long time ago. Thank you Steve and Yuhang as my great roommates, who brought me lots of happiness and memorable moments as a “family” during my stay in Waterloo.

This thesis is dedicated to my family, especially to my grandma.

Table of Contents

Chapter 3 Crystallography

References

List of Tables

List of Figures

List of Uncaptioned Figures

Figures are numbered sequentially in each chapter. The numerical prefix in the figure label corresponds to the chapter in which the figure may be found. For example, a figure in Chapter 1 will be assigned the prefix **1-**. The same figure may appear in multiple chapters, having the appropriate prefix.

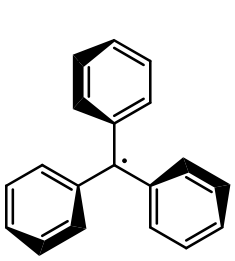

1-1

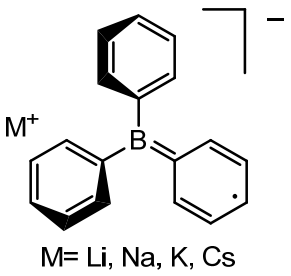

1-2

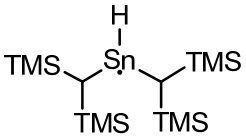

1-3

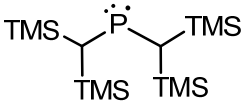

1-4

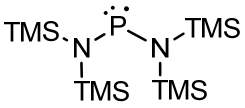

1-5

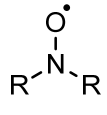

1-6

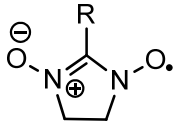

1-7

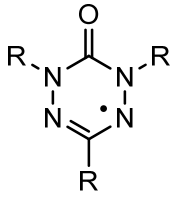

1-8

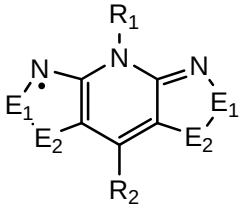

	1-9	1-10	1-11	1-12
E_1	S	S	Se	Se
E_2	S	Se	S	Se

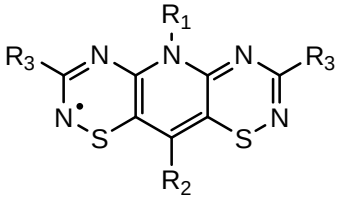

1-13

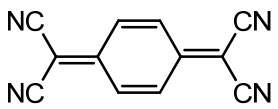

1-14

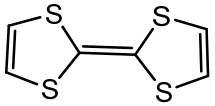

1-15

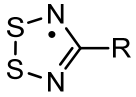

1-16

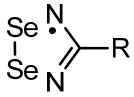

1-17

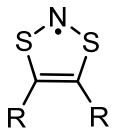

1-18

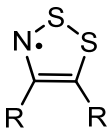

1-19

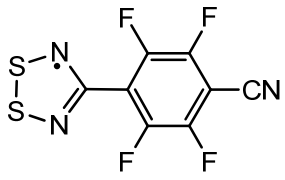

1-20

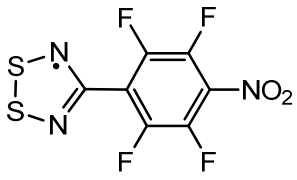

1-21

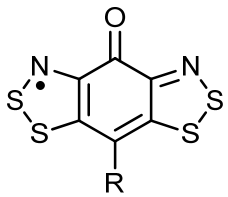

1-22

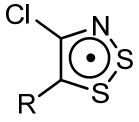

2-1

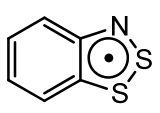

2-2

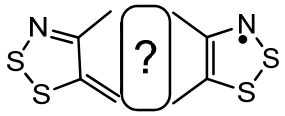

2-3

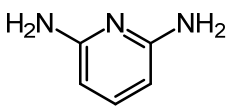

2-4

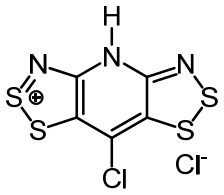

2-5

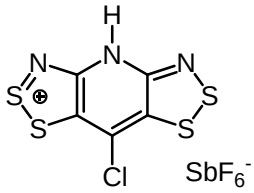

2-6

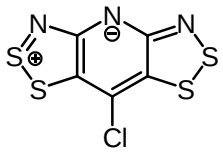

2-7

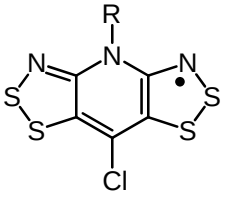

2-8

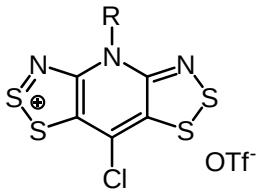

[**2-8**][OTf]

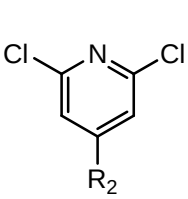

2-9

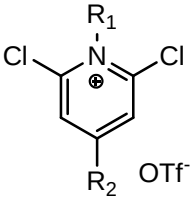

2-10

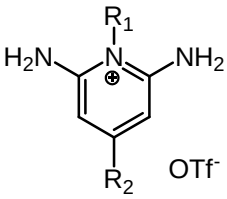

2-11

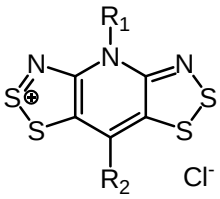

2-12

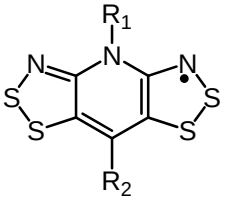

2-13

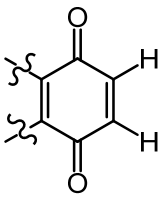

2-14

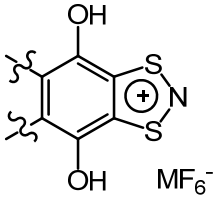

2-15 (M= As, Sb)

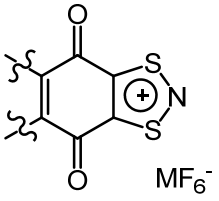

2-16

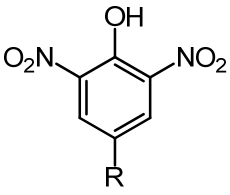

2-17

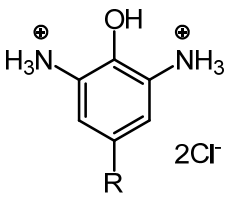

2-18

	a	b	c	d	e	f
R	H	Cl	Br	Ph	Me	Et

for **2-17** to **2-19**

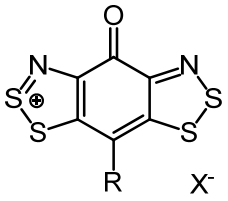

[**2-19**][X]

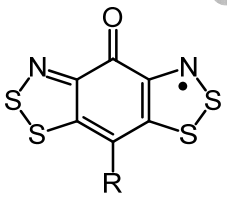

2-19

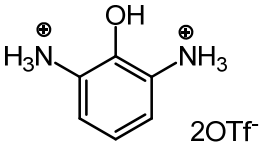

2-20

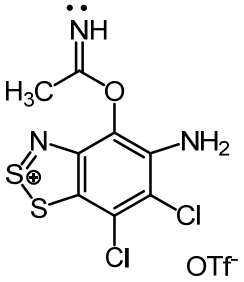

2-21

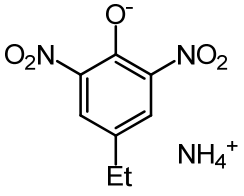

2-22

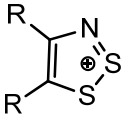

2-23

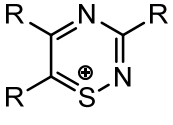

2-24

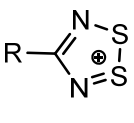

2-25

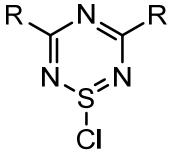

2-26

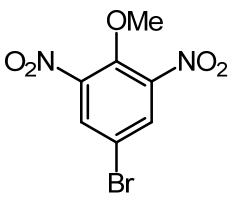

2-27

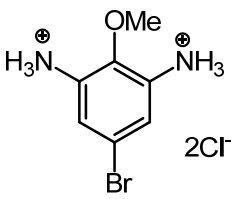

2-28

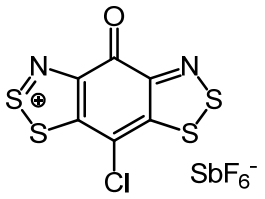

[**3-1**][SbF_6]

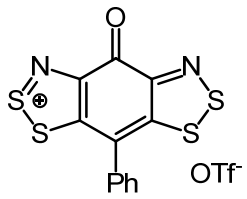

[**3-3**][OTf]

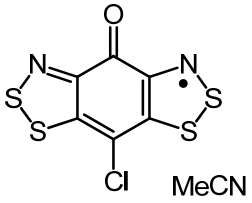

3-1 • MeCN

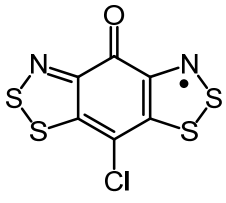

3-1

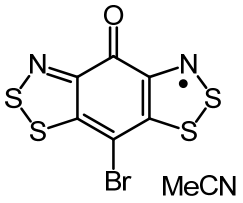

3-2 • MeCN

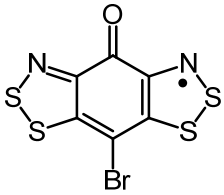

3-2

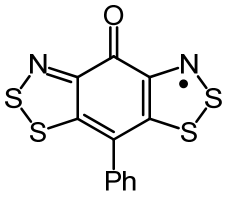

3-3

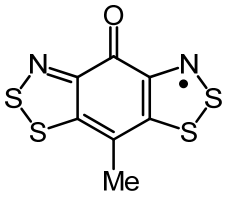

3-4

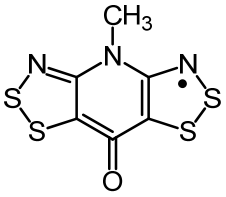

3-5

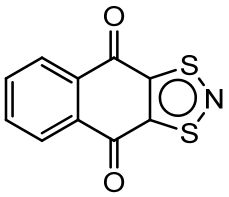

3-6

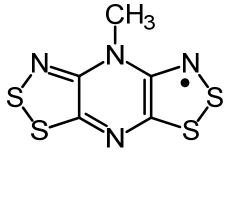

3-7

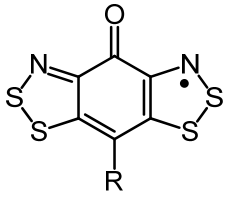

4-1

	a	b	c	d
R	Cl	Br	Me	Ph

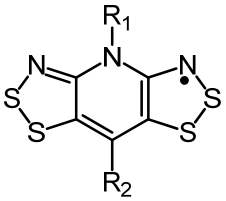

4-2

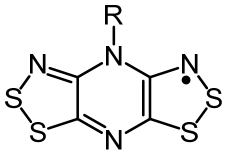

4-3

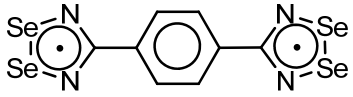

5-1

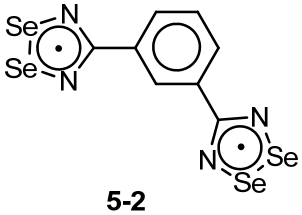

5-2

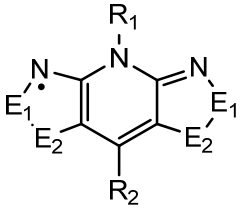

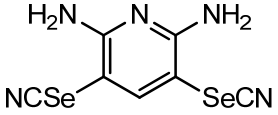

5-7

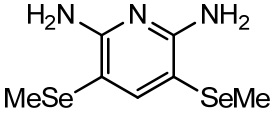

5-8

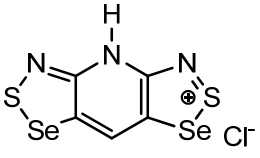

5-9

	5-3	**5-4**	**5-5**	**5-6**
E_1	S	S	Se	Se
E_2	S	Se	S	Se

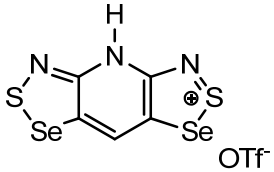

5-10

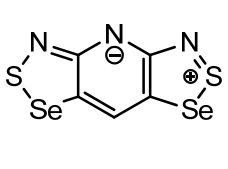

5-11

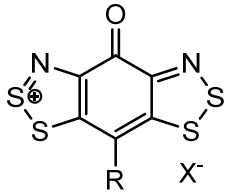

[**5-12**]$^+$

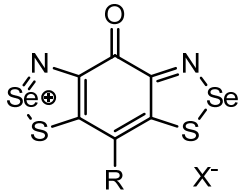

[**5-13**]$^+$

List of Abbreviations

a	crystallographic unit cell axis; hyperfine coupling constants
^{1}H	proton
Å	Angstrom
$A^{\cdot -}$	radical anion
AFM	antiferromagnetic
anal.	analysis
b	crystallographic unit cell axis
BB	semiquinone-bridged *bis*-dithiazolyl
BP	pyridne bridged *bis*-dithiazolyl
bp	boiling point
br	broad (IR peak descriptor)
c	crystallographic unit cell axis
C	Curie constant
calcd.	calculated
CB	conduction band
CDW	Charge-density-wave
cm^{-1}	reciprocal centimetres
CO	crystal orbital
CV	cyclic voltammetry
D	dimensionality, as in 1D or 3D; doublet (NMR peak descriptor)
$D^{\cdot +}$	radical cation
DCE	dichloroethane
DCM	dichloromethane
dec.	decomposition
DFT	density funcitonal theory
DMSO	dimethylsulfoxide
DTA	dithiazolyl
DTDA	dithiadiazolyl
e	charge of each carrier
E	chalcogen, either sulfur or selenium
E	energy
E1	chalcogen in the 1-position of the *bis*-dithiazolyl framework, sulfur or selenium
$E_{1/2}^{(ox)}$	oxidation potential
$E_{1/2}^{(red)}$	reduction potential
E2	chalcogen in the 2-position of the *bis*-dithiazolyl framework, sulfur or selenium
EA	electron affinity
E_{cell}	electrochemical cell potential,

EHT	extended Hückel theory
emu	electromagnetic unit
E_{pc}	cathodic peak potential
EPR	electron paramagnetic resonance
ESI-MS	electrospray ionization mass spectrometry
Et	ethyl
EtCN	propionitrile
eV	electron volt
ϕ	atomic orbital
f	degree of band filling
FC	field cooled
FM	ferromagnetic
g	g-factor (EPR descriptor)
g	gram
GPa	gigapascal, unit of pressure
H	applied magnetic field
h	hour
H_C	hysteresis (coercivity or coercivity field)
Hz	Herz
IP	ionization potential
IR	infrared
$\boldsymbol{J}$	exchange parameter
J	total angular momentum quantum number
j	quantum number labels the Bloch state for particle on the ring model
k	wavevector labels the Bloch state for straight chain model
K	Kelvin
L	total orbital angular momentum number
L	liter
lit.	literature
M	level of magnetization
m	medium (IR peak descriptor); multiplet (NMR descriptor)
M	molecular weight
Me	methyl
MeCN	acetonitrile
min	minute
mL	millilitre
mmol	millimole
mol	mole
mp	melting point
M_r	Remanent magnetization (remanence)
M_{sat}	saturation magnetization

mT	millitesla
n	number of charge carrier; ring size
N_A	Avogadro constant
NMR	nuclear magnetic resonance
º	degree
ºC	degree centigrade
Oe	Oersted
OTf	trifluoromethanesulfonate (triflate)
Ph	phenyl group
R	distance from origin in Bloch function for straight chain model
R	general substituent group
r_{cov}	covalent radius
S	Siemens ($1S = 1\Omega^{-1}$); singlet state
s	strong (IR peak descriptor); singlet (NMR peak descriptor); second
S	spin quantum number; orbital overlap
S^2	multiplicity
SOMO	singly occupied molecular orbital
T_C	Curie temperature
TCNQ	tetracyano-*p*-quinodimethane
TDA	thiadiazolyl
TDAE	tetrakis(dimethylamino)ethylene
T	temperature
TMPDA	tetramethyl propylenediamine
TMS	trimethylsilyl
T_N	Néel temperature
TSF	tetraselenafulvalene
TTF	tetrathiafulvalene
U	on-site Coulomb repulsion energy
u_m	atomic wavefunction
UV-Vis	ultraviolet-visible spectroscopy
V	potential, volume
V	volt
VB	valence band
vs	very strong (IR peak descriptor)
vs.	versus
W	bandwidth
w	weak (IR peak descriptor)
x	Cartesian coordinate
XRD	X-ray diffraction
y	Cartesian coordinate
z	Cartesian coordinate

Z	number of asymmetric units per unit cell (multiplicity)
ZFC	zero field cooled
α	columbic parameter
β	Bohr magneton, crystallographic axis angle; resonance integral
δ	chemical shift in ppm; mean separation of molecules in a slipped stack
ΔH_{disp}	gas-phase disproportional enthalpy
θ	Weiss constant
λ	wavelength
μ	mobility of charge carrier; molecular magnetic moment, absorption coefficient
μA	microamps
π	orbital symmetry
ρ	electrical resistivity; spin density, density
σ	orbital symmetry
σ	electric conductivity
σ_{RT}	room temperature conductivity
τ	angle between the mean plane of the heterocyclic backbone and the stacking axis
υ	frequency
χ	magnetic susceptibility
χ_{dia}	diamagnetism
χ_{TIP}	temperature independent paramagnetism
$\hat{H}$	Hamiltonian

Chapter 1

Introduction

1.1 Introduction

Radicals are defined as a class of molecules with at least one unpaired electron, and are usually considered to be extremely unstable and reactive.[1] They are widely used in organic chemistry and are particularly important for industrial processes. The unpaired electron can act as either a nucleophile or an electrophile to initiate a variety of organic reactions and polymerization processes. The lifetime for this type of radical is usually on the order of minutes.[2] There are also a number of long-lived Main Group radicals based on the first row elements, *i.e.,* C, N and O. For example, simple molecules like O_2, NO and NO_2 all have unpaired electrons, and have been well known for a long time.[3]

Depending on the lifetime of the radicals, they can be divided into three categories, (i) stable radicals, (ii) persistent radicals, and (iii) transient radicals. Stable radicals usually refer to species that can be isolated and, under inert atmosphere, are stable indefinitely at room temperature.[3] By contrast, persistent radicals have half-lives that vary from seconds to a year, whereas transient radicals have half-lives of less than 10^{-3} second.[4]

In 1900, the first stable organic radical **1-1** was isolated by Moses Gomberg.[5] It is stabilized both electronically and sterically. The phenyl rings with large electron density are attached to the central tertiary carbon. The π-electrons on the phenyl ring can donate electron density to the central carbon; as a result the unpaired electron is stabilized. Meanwhile, the bulky groups occupy enough space to prevent reactions at the carbon center.

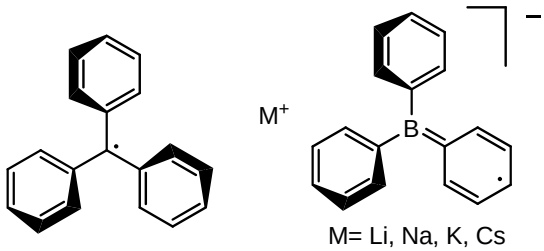

1-1 **1-2**

During the past few decades, several classes of stable Main Group inorganic radicals have been synthesized and characterized following the idea of electronic and steric stablization. These radicals usually involve Group 13, 14, 15 and 16 elements.[3] For instance, the triphenylboron radical anion **1-2** was generated by reduction of BPh_3 by alkali metals (M = Li, Na, K, Cs).[6] The tin-centered radical $SnH\{CHSi[(CH_3)_3]_2\}_2$ **1-3** was prepared photochemically,[7] as were the first stable phosphorus-based radicals **1-4** and **1-5**.[8] Radicals based on sulfur and selenium will be discussed later.

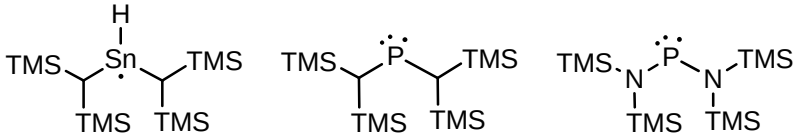

1-3 **1-4** **1-5**

TMS= trimethylsilyl

As a result of the presence of the unpaired electron, some radicals display interesting properties, and have been actively studied for many technological applications. For instance, they are widely used in spin labeling,[9] EPR (Electron Paramagnetic Resonance) imaging,[10] as radical polymerization catalysts,[11] organic ferromagnets,[12] molecular conductors,[13] liquid crystalline magnetic materials,[14] and information storage devices.[15] Also some radicals can serve as spin bearing ligands, which coordinate to metals and form ferrimagnetic materials.[16]

The Oakley group focuses on the design and synthesis of nitrogen-sulfur (-N=S-) and nitrogen-selenium (-N=Se-) based radicals, with a view to generating solid state materials that display magnetic and conductive properties.[17] This idea originated from the successful development of N / O radical based materials, *i.e.,* nitronyls **1-6**,[18] nitronyl nitroxides **1-7**,[19] and verdazyls **1-8**.[20]

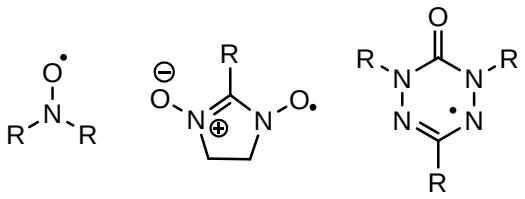

1-6 **1-7** **1-8**

The elements sulfur and selenium are, like oxygen, members of Group 16 (VI A) of the Periodic Table. In principle, for N / S, N / Se based radical building blocks, the unpaired electrons can serve as both a charge carrier and a magnetic coupler. In the most recent research in the Oakley group, families of resonance stabilized *bis*-DTA (dithiazolyl) radicals **1-9** to **1-12** and *bis*-TDA (thiadiazinyl) radicals **1-13** were developed.[13b] Fine-tuning of the exocyclic R-groups in these materials allows for modification of the packing in the solid state, a process which can affect the electronic and magnetic properties of the system.[21] In addition, substitution of S with Se, leads to an increase in intermolecular orbital overlap, which can enhance conductivity and alter magnetic properties.[22]

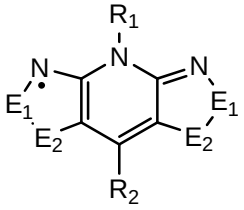

	1-9	**1-10**	**1-11**	**1-12**
E_1	S	S	Se	Se
E_2	S	Se	S	Se

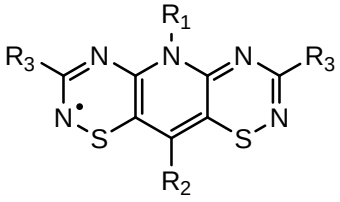

1-13

1.2 Band Theory - LCAO Approach[23]

In order to understand the electronic properties of these radical based materials it is important to examine the band theory, which can be developed from a particle-on-a-ring model with a periodic potential. The picture that emerges from this model is however incomplete, as will be discussed in subsequent sections. In the particle on a ring model, at each periodic point on this ring the potential is the same (*i.e.,* $V_{(\theta)} = V_{(\theta+2\pi/n)}$, $\theta = 2\pi/n$), as illustrated in Figure 1.1.

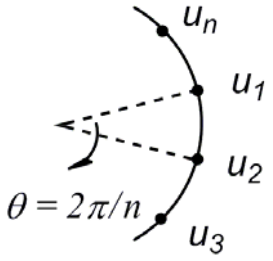

Figure 1.1. A particle on a ring of periodic potential.

The wavefunction of the particle (electron) is given by the Bloch function shown in equation 1.1. In this equation u_m is the atomic or molecular wavefunction at each point m, where m is the site label, where m = 1, 2, 3, …, n; and j = 0, 1, 2, …, n-1, where j is the quantum number that labels the Bloch state. From a chemical point of view, each site on this ring can be considered as an atom or molecule, and n is the total number of atoms or molecules on this ring. Therefore the particle-on-the-ring model is good for describing molecular orbitals for cyclic π systems. The solutions to this equation are pure angular momentum states (*i.e.,* moving waves), thus the sums and differences are taken to obtain standing waves which gives the wavefunctions of the molecular orbitals.

$$\psi_j = \frac{1}{\sqrt{n}} \sum_{m=1}^{n} \exp\left(\frac{2\pi i j m}{n}\right) u_m \qquad \textbf{(1.1)}$$

According to the Schrödinger equation $\hat{H}\psi = E\psi$, the energy of each wavefunction can be calculated following equation 1.2. For a normalized wavefunction, $\int \psi^* \psi d\tau = 1$.

$$E = \frac{\int \psi^* \hat{H} \psi d\tau}{\int \psi^* \psi d\tau} \qquad \textbf{(1.2)}$$

In order to evaluate the energy, we define β as the resonance integral (given by equation 1.3), which is related to the orbital overlap, and the Coulomb parameter α as shown in equation 1.4,

$$\beta = \int u_{m-1} \hat{H} u_m d\tau = \int u_{m+1} \hat{H} u_m d\tau \qquad \textbf{(1.3)}$$

$$\alpha = \int u_m \hat{H} u_m d\tau \qquad \textbf{(1.4)}$$

In this tight-binding approximation, where only the interactions between nearest neighbors are considered, the energy of each Bloch function is given by equation 1.5. It is clear that the maximum and minimum orbital energy of a ring is independent of the ring size. All the energy levels of the orbitals are confined to the values between $\alpha \pm 2\beta$, which yields the maximum energy dispersion of 4β.

$$E_j = \alpha + 2\beta \cos(\frac{2\pi j}{n}) \qquad \textbf{(1.5)}$$

The relative energy of molecular orbitals for a ring system can now be sketched out as shown in Figure 1.2. With increasing the ring size (*i.e., n* increases), the energy difference between the orbitals decreases. For large *n*, a nearly continous energy band with a width of 4β is produced.

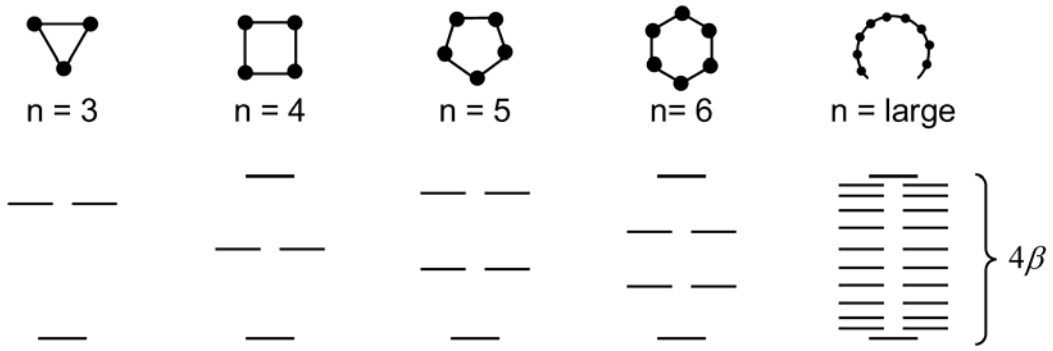

Figure 1.2. Relative orbital energy levels for ring systems.

In this limit, the radius of the ring becomes so large that the curvature approaches zero. Thus a finite section of the ring can be treated as a one dimensional chain, as illustrated in Figure 1.3.

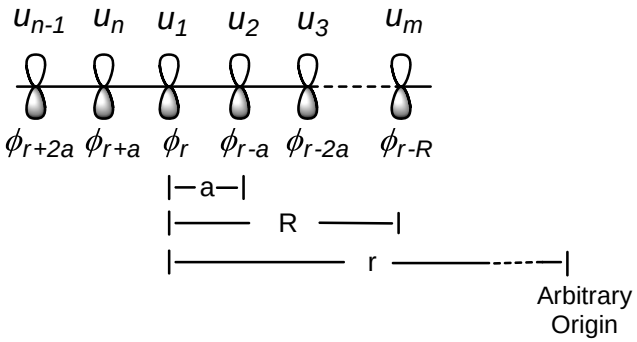

Figure 1.3. One dimensional chain with periodic potential.

In this model, the periodic potential positions are defined in terms of the distance from some arbitrary origin, where $R = ma$. The Bloch function should then be rewritten as equation 1.6 and the energy is given by equation 1.7. The wavevector k labels the Bloch states and has units of reciprocal distance, which satisfy the condition of $-\frac{\pi}{a} < k \leq \frac{\pi}{a}$.

$$\psi_k = \frac{1}{\sqrt{n}} \sum_{m=1}^{n} \exp(ikma)\phi_{(r-ma)} \tag{1.6}$$

$$E_k = \alpha + 2\beta\cos(ka) \tag{1.7}$$

Commonly the energies are mapped out over the $k = (0 \ldots \pi/a)$ continuum, giving dispersion curves. A typical dispersion curve of a theoretical one dimensional infinite chain of atoms, each of which has s, p_x, p_y and p_z orbitals, is illustrated in Figure 1.4. At $k = 0$, all the atomic orbitals are in phase, which yield bonding orbitals for σ_s and $\pi_{px,y}$ and antibonding orbitals for σ_{pz}. At $k = \pi/a$ all the orbitals are out of phase, thus the bonding properties of this chain is reversed. In general the antibonding orbitals have higher energy than the bonding orbitals for a given shell. At $k = \pi/2a$ the Bloch state energy is equal to the atomic energy.

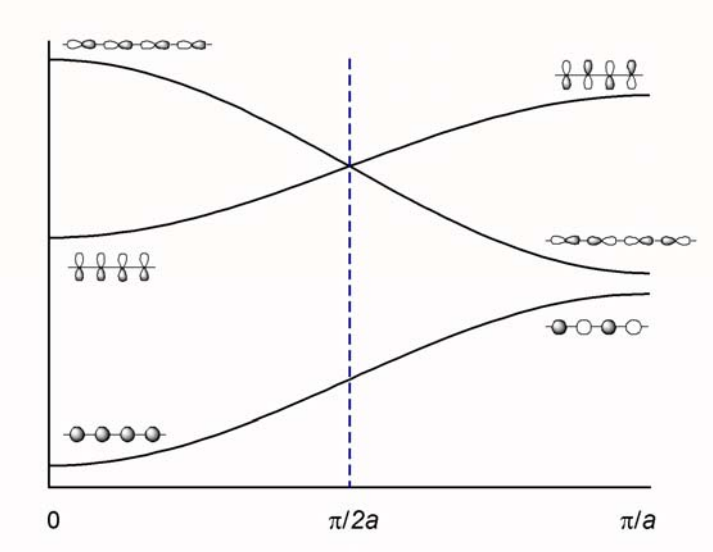

Figure 1.4. Dispersion curve and orbital overlap of σ and π orbitals.

In a solid, the highest energy of filling in the ground state is defined as Fermi level. The density of state (DOS) is the number of states in a small energy increment δE.

1.3 Energy Bands[24]

In the solid state, the overlap between orbitals gives rise to energy bands and the forbidden regions between the bands as referred to as band gaps. The highest filled band is called the Valence Band (VB) and the first (lowest) empty band is named the Conduction Band (CB). Depending on the size of the band gaps and the filling of the bands, materials can be generally divided into the following categories: metal, insulator, semi-metal and semi-conductor as illustrated in Figure 1.5.

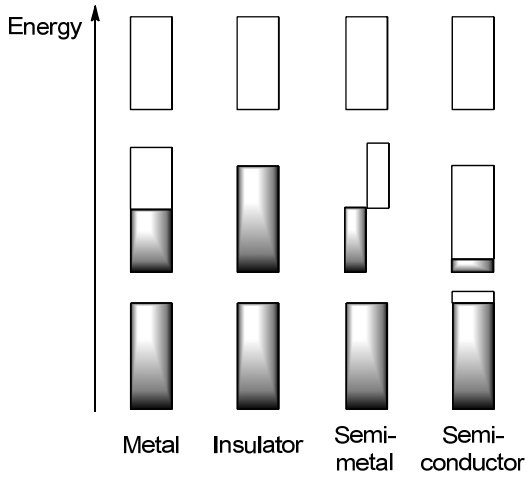

Figure 1.5. Schematic energy diagram of different materials.

The electrical conductivity (σ) of a material is defined as the products of the number of charge carriers (n), the charge of each carrier (e) and the mobility of the charge carriers (μ) (shown in equation 1.8).

$$\sigma = n|e|\mu \tag{1.8}$$

In general, metals satisfy the two critical requirements for creating conductive materials, which are (a) a large number of charge carriers n and (b) a pathway to allow for the flow of the charge carriers giving a large mobility μ.

Semiconductors and insulators both have a filled valence band and an empty conduction band, but are distinguished by the size of their band gaps. Semiconductors have a relatively small band gap. When external thermal energy is applied, electrons in the Valence Band can be excited to the Conducting Band generating charge carriers. In an insulator, the large band gap prevents the excitation of valence electrons at ordinary temperatures, therefore its conductivity is low.

1.4 Charge Density Wave (CDW)[23]

According to band theory, a one-dimensional (1D) array of hypothetical atoms with partially filled orbitals should exhibit metallic conductivity. However, in real materials this is not always the case, because such a system is susceptible to a Perierls distortion also known as a charge density wave (CDW) driven distortion. As a result, the atom positions are periodically distorted and the order of the evenly spaced 1D array is broken. This type of distortion is observed in some partially filled 1D systems. Consider the half filled system (*i.e.,* a π-stack of radicals) as an example, which is an infinite chain with periodic potential and has one unpaired electron per site (shown in Figure 1.6a). In the undistorted array, all the molecules are evenly spaced in a lattice with unit cell length *a*. In the most energetically favorable distorted array (as shown in Figure 1.6b), the molecules form dimers and the unit cell length becomes 2*a*.

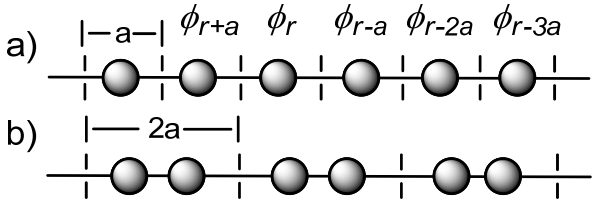

Figure 1.6. Lattice parameters for (a) a regular array and (b) a Peirels distorted array.

The effect of Peierls distortion on the dispersion curve of half filled system is illustrated in Figure 1.7.

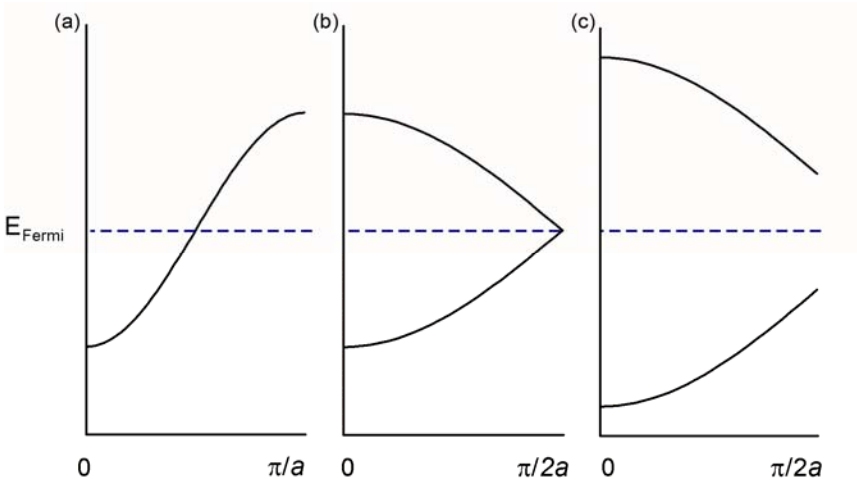

Figure 1.7. Effects of Periels distortion on a half filled system: (a) regular array, (b) doubled unit cell, (c) distorted array.

For a regular 1D chain, the dispersion curve is shown as Figure 1.7a. A Peierls distortion can be considered as two processes: (1) doubling of the unit cell length and (2) formation of dimers. Upon doubling the unit cell length, the reciprocal vector is halved and the dispersion curve is mapped from k = 0 to $k = \pi/2a$ to produce two bands without a band gap (as shown in Figure 1.7b). As the molecules distort from the original position by a distance Δx, the distortion introduces two resonance integrals β_1 and β_2. When $|\beta_1| > |\beta_2|$, the energy at the boundary is shown in equation 1.9. Therefore, a band gap is created at Fermi level with $E_{gap} = 2(\beta_2 - \beta_1)$ as shown in Figure 1.7c.

$$\begin{aligned} k &= 0 \qquad & E &= \alpha \pm (\beta_1 + \beta_2) \\ k &= \pi / 2a \qquad & E &= \alpha \pm (\beta_1 - \beta_2) \end{aligned} \tag{1.9}$$

From a conductivity point of view, Peierls distortion is one of the major problems associated with creating conductors using radicals. In order to overcome this problem, high pressure and high temperature can be applied to decrease the level of distortion. Under ambient conditions, increasing the dimensionality of the material can also increase the stability towards CDW driven distortion.

1.5 Hopping Model of Conductivity and Mott Insulators

In principle, metallic conductivity should be observed in half-filled systems, like radical arrays, if they do not succumb to Peierls instability. However this is not always the case, as electron-electron repulsion creates a large barrier to electron transfer in some materials. This barrier is referred to as the onsite Coulomb repulsion energy (U), and is an intrinsic complication for any $f = ½$ system. The origin of this barrier can be understood with reference to the simple electron hopping model illustrated in Figure 1.8. Thus, when $f = ½$, there is one electron per site, and electron transfer requires moving an electron from one site onto an already occupied site (orbital). This process must overcome a high on-site Coulomb repulsion energy (U), and will require a large charge transfer integral or resonance interaction (β) between neighboring orbitals in order to achieve high conductivity. By contrast, in a $f = ¼$ system, or indeed in any system with band-filling other than $f = ½$, charge transfer can take place to a vacant orbital and, as a result, the Coulomb repulsion barrier is much lower.

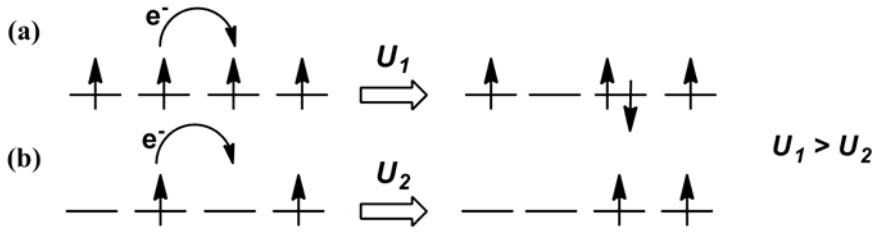

Figure 1.8. On-site Coulomb repulsion energy (U) for (a) $f = ½$ and (b) $f = ¼$ systems.

Systems possessing $f = ½$ band electronic structures, in which the electrons are essentially trapped on separate sites, are referred to as Mott insulators.[25] In order to overcome the on-site Coulomb barrier associated with such systems, a large bandwidth W (where $W = 4\beta$) is required.[26] Thus, in general, a large W / U ratio leads to good conductivity, and a small W / U ratio results in poor conductivity.

1.6 Charge Transfer Salts - The First Organic Conductors

As a result of the absence of charge carriers in pure, single component, closed shell molecules, their room temperature conductivity is low. However, the co-crystallization of two closed shell materials, one an electron donor (D) and the other an electron acceptor (A), can give rise to conductive materials, as the process of charge transfer between the two species creates charge carriers. Moreover, in the case of π-donors and π-acceptors, the formation of extended π-stacked arrays of donors and acceptors can give rise to effective pathways for charge transport. These types of materials, which are customarily defined as charge transfer salts, have been extensively studied since the mid-1950s.[27] In a typical charge transfer salt, charge transfer generates radical cations ($D^{\cdot+}$) and anions ($A^{\cdot-}$), as in Scheme 1.1, and these open shell species form π-stacked structures which allow for transport.

Scheme 1.1

In the early 1960s, the discovery of the powerful π-acceptor TCNQ (tetracyano-*p*-quinodimethane) **1-14**[28] led to major improvements in the conductivity of charge transfer salts.[29] Then, in 1972, the sulfur-based π-donor TTF (tetrathiafulvalene) **1-15** was discovered, and this allowed for the development of many new charge transfer materials with much higher conductivities.[30] In particular the salt [TTF][TCNQ] displayed a conductivity (σ) of 1.47×10^4 S cm^{-1} at 66 K.[31] Compared with values of $\sigma \sim 10^{-10}$ S cm^{-1} at room temperature for most closed shell organic materials and 10^{-2} S cm^{-1} at room temperature for other charge transfer salts,[27] the performance of [TTF][TCNQ] was remarkable, and this finding became a benchmark in the development of organic conductive materials. Figure 1.9 shows the slipped π-stack structure of [TTF][TCNQ], and illustrates the effect of charge transfer on the degree of band-filling of the energy bands associated with the donor and acceptor π-stacks. The unusually high conductivity for this material arises from the partial charge transfer between the donor and acceptor, that is, less than one electron per molecule. In this way the ½ -filled band, which is susceptible to CDW instabilities.

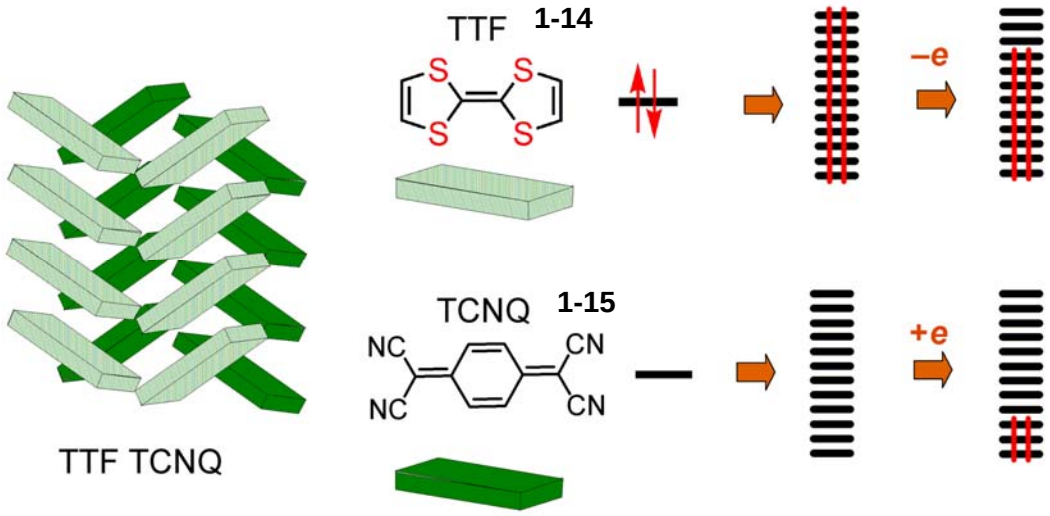

Figure 1.9. Slipped π-stacks of [TTF][TCNQ] (left), and the effect of charge transfer between TTF and TCNQ on bandfilling of donor and acceptor sub-bands.

In the early stages of developing TCNQ based charge transfer salts, 1:1 cation-to-anion ratios were avoided. Commonly, 1:2 ratio of cation to TCNQ anion, *i.e.,* $[Et_3NH][TCNQ]_2$, was used to achieve a ¼-filled energy band,[27] and high conductivity could be achieved by promoting strong π-orbital overlap, which afforded a good conduction pathway. Within this context, replacing sulfur in TTF with its heavier congener selenium gave a tetraselenium heterocyclic donor, tetraselenafulvalene (TSF), which remained highly conductive even at extremely low temperature in a 1:1 ratio with TCNQ.[27]

1.7 Neutral Radicals - Single Component Organic Conductors

In 1975, Robert Haddon proposed that neutral π-radicals might serve as useful building blocks for conducting materials instead of charge transfer salts.[13a] In principle, the unpaired electrons in a neutral π-radical should be capable of serving as charge carriers. Essentially, the unpaired electrons in these materials form a half-filled energy band in the solid state, similar to that found in an elemental metal such as sodium.[13b] However, high conductivities in these systems would require strong intermolecular interactions and a large solid state bandwidth *W* to overcome the high on-site Coulomb repulsion energy

U associated with a $f = ½$ system. This concept is illustrated in Figure 1.10b, which shows the development of a $f = ½$ energy band by the overlap of Singly Occupied Molecular Orbitals (SOMOs) on neighboring molecules within a superimposed π-stack of radicals. Estimating the value of *U* is difficult, but useful trends can be developed within a series of compounds by comparing the values of their gas-phase disproportion enthalpy, ΔH_{disp} (the difference between the ionization potential (*IP*) and electron affinity (*EA*)). Solution based estimates, using the electrochemical cell potential, E_{cell}, the difference between oxidation potential ($E_{1/2}^{(ox)}$) and reduction potential ($E_{1/2}^{(red)}$),[13a,27] can also be employed. These ideas are expressed in equation 1.10. Values of ΔH_{disp} and E_{cell} can be either calculated or measured easily.

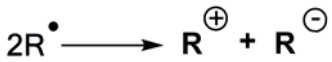

$$\Delta H_{disp} = IP - EA$$
$$E_{cell} = E_{1/2}^{(ox)} - E_{1/2}^{(red)} \qquad \textbf{(1.10)}$$

Figure 1.10 also shows the two major problems associated with designing neutral radical conductors. The first problem, illustrated in Figure 1.10c, is the Mott insulator trap described above, which arises from the high on-site Coulomb repulsion energy associated with the ½-filled band structure which is basic to the neutral radical paradigm. The second, shown in Figure 1.10d and also described above, is the charge-density-wave (CDW) or Peierls distortion which can easily occur in this type of one-dimensional system. For the past 30 years, all work on the design of conductive materials based on neutral radicals has involved attempts to address these two fundamental design challenges.

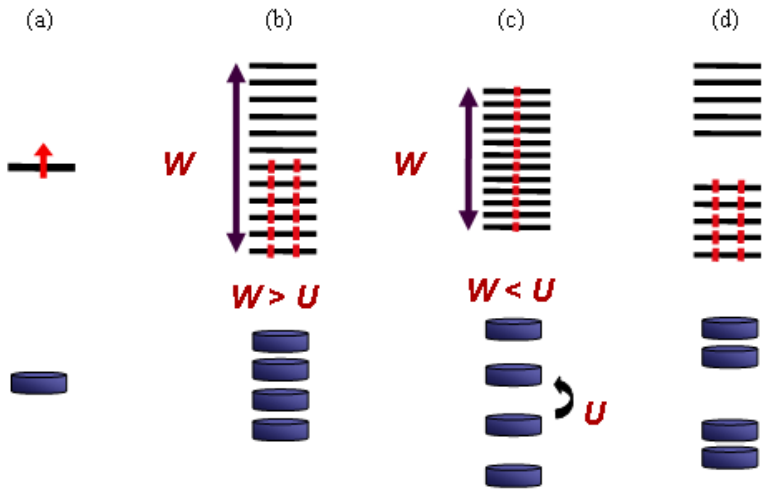

Figure 1.10. Energy levels of (a) a single π-radical, (b) a metallic state, (c) a Mott insulator and (d) a Peierls distorted π-radical.

1.8 Development of S-N Based Conducting Radicals

For many years the Oakley group has been working on the design of neutral radical conductors using electron-rich sulfur / selenium-nitrogen heterocycles. The reason for using these radicals, as opposed to all carbon or simple nitrogen based radicals, is that the presence of the heavy heteroatom (S or Se) should provide better intermolecular orbital overlap, a feature needed to overcome the high on-site Coulomb repulsion and promote good conductivity.[13b]

The initial focus of work in the Oakley laboratory was on molecules based on the 1,2,3,5-DTDA (dithiadiazolyl) framework **1-16** and its selenium analogue **1-17**. While structures displaying the desired π-stacking could be achieved, the relatively localized spin distributions in these radicals caused them to undergo a Peierls distortion, that is, they dimerized in the solid state.[32] Thus there were no electrons available to transfer charge, and the conductivity for the S-based materials were extremely low.[33] However, the Se-based compounds showed excellent semi-conductive behavior, and partial oxidation of both the S- and Se-based radicals with iodine and bromine afforded charge transfer salts with good conductivity (σ_{RT} > 100 S cm^{-1}).[17b,34]

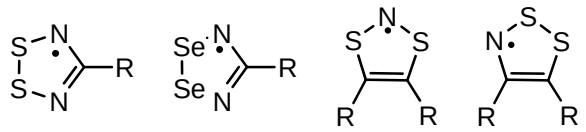

1-16 **1-17** **1-18** **1-19**

In the mid-1990s attention was moved to 1,3,2- and 1,2,3-DTA radicals **1-18**, **1-19**. In most cases of 1,3,2-DTA radicals **1-18** are fairly stable, and often do not dimerize in the solid state or solution phase.[35] However the intermolecular S···S distances along the π-stacking direction are rather long (*ca.* 3.6 - 3.7 Å).[35] In comparison these distances are close to the non-bonding van der Waals contact (*ca.* 4.0 Å)[36] and longer than the S···S distance found in DTDA dimers (*ca.* 3.0 Å)[37]. Hence the orbital overlap is poor and high conductivities for this type of radical were not reached.

About 15 years ago, the Oakley group began work on 1,2,3-DTA radicals **1-19**. These systems are isoelectronic to 1,3,2-DTA and 1,2,3,5-DTDA radicals, possessing seven π-electrons. Initial structural studies indicated that this type of radical also suffered from a tendency to dimerize in the solid state.[38] However, one of the attributes of these systems was the fact that the value of ΔH_{disp} and E_{cell} could be reduced by the attachment of electron withdrawing substituents. As a result, these systems provided the potential for improved conductivity, and indeed one of the best thiazyl radical conductors ever characterized stemmed from these ideas.[38-39]

Continuing efforts to improve molecular ion energetics eventually led to the development of resonance stabilized bisdithiazolyl radicals such as **1-9**. These materials enjoyed much better ion energetics (lower values of ΔH_{disp} and E_{cell}), by virtue of the delocalization of spin across the entire molecule. Moreover, the higher delocalization energy also led to structures in which dimerization was avoided, although some examples of lateral σ-dimerization, as shown below in Scheme 1.2, have been observed.[40]

Scheme 1.2

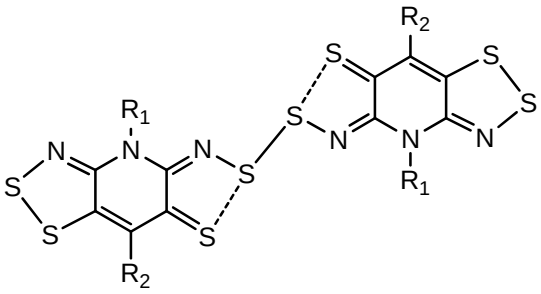

From a structural perspective, these radicals tend to crystallize in slipped π-stack arrays, as illustrated in Figure 1.11. Stack slippage, which is driven in part by the steric bulk of the R_1 and R_2 groups, leads to a decrease in intra-stack orbital overlap, as a result of which both the electronic bandwidth and conductivity are reduced. For these systems bandwidth can be increased, and conductivity enhanced, by partially eliminating the steric effects of the R_1/R_2 groups, so as to allow superimposed stacking.[41]

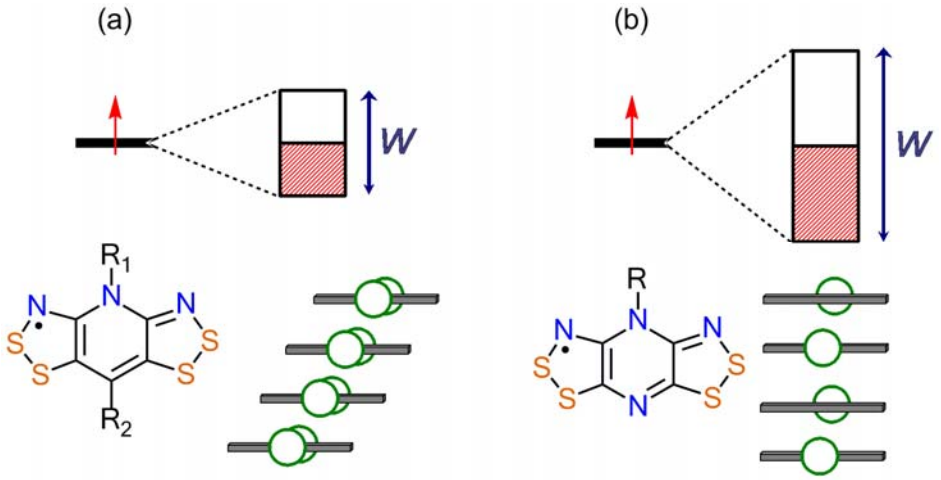

Figure 1.11. Bandwidth trends associated with slipped (a) and superimposed (b) π-stacks.

Alternatively, bandwidth and hence conductivity can be increased by the incorporation of selenium in place of sulfur. Synthetic methods to these resonance stabilized heavy atom radicals have been developed over the last five years,[42] and these have allowed the design of a wide range of radicals with different solid state structures. Typically these materials **1-10** to **1-12** display conductivities two to

three orders of magnitude higher than those observed for the related sulfur based compounds **1-9**.[42a,43] In addition, these materials also exhibit interesting magnetic properties, which will be discussed in the following sections.

1.9 Radicals as Magnets

Magnetism is a valued property of matter, one that has been in use for over 1000 years.[44] Magnetic materials can be classified according to the way that the spin of unpaired electrons present in open shell atoms and molecules interact with each other. Some of the possibilities are illustrated schematically in Figure 1.12. In a closed shell or diamagnetic material there are no unpaired spins, but such materials do nonetheless experience a very weak repulsion to an external field due to induced orbital motion of the electrons. These residual diamagnetic effects are, in fact, present in all matter, regardless of whether other forms of magnetism are observed. In materials possessing unpaired electrons, various forms of spin alignment are possible. In an ideal paramagnetic substance there are no magnetic interactions between the spins, which behave essentially independently from one another. In the presence of a magnetic field there is a temperature dependent orientation of some of the spins by the field. This orientation is lost when the field is removed. In a ferromagnetically ordered material, such as iron or nickel, all the spins are aligned in parallel, while in an antiferromagnetic substance an alternating alignment of the moments is found. There are, in addition, more exotic forms of magnetism, including ferrimagnetism, which consists of an antiferromagnetic ordering of moments of unequal magnitude. Canted antiferromagnetism, or weak ferromagnetism, arises when the alignment of the spins in a material which is essentially antiferromagnetic is tipped or canted, so as to produce a net bulk magnetic moment. This phenomenon is usually found in materials possessing polar space groups.

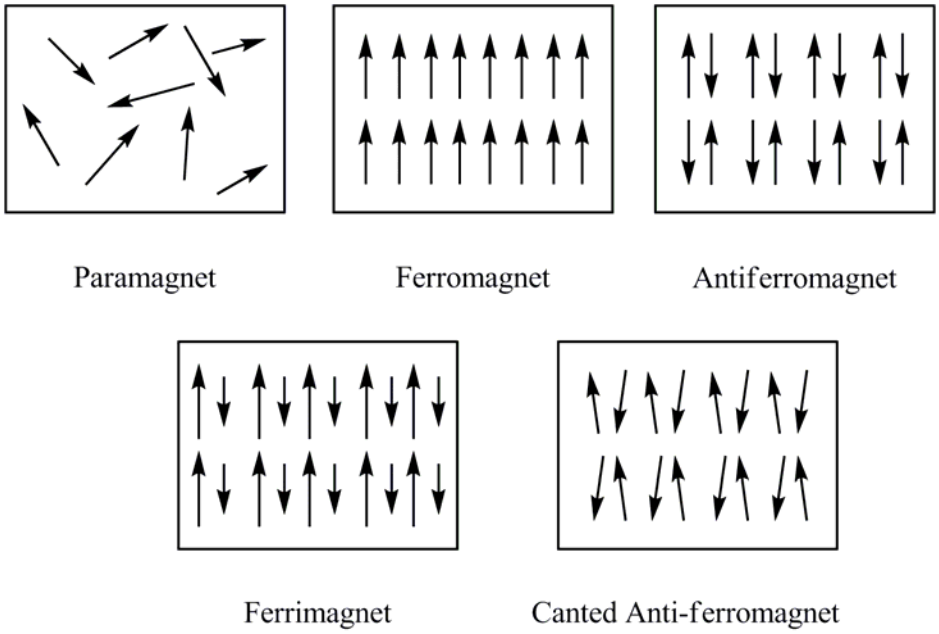

Figure 1.12. Schematic diagram illustrating spin orientations for different types of magnetism.

1.10 Magnetic Susceptibility[44]

The response of a material to a magnetic field is usually described in terms of its bulk magnetic susceptibility $\chi = M / H$, where M represents the level of magnetization of the material in an applied magnetic field H. For typical ferromagnetic species, the magnetic susceptibility varies with temperature as shown in Figure 1.13. At high temperatures, they become paramagnetic. The critical temperature for ferromagnets is called the Curie temperature (T_C), which is also known as the ordering temperature. Similar phenomena can also be observed in an antiferromagnetic system. With decreasing temperature, the susceptibility increases to a maximum and then decreases. The maximum temperature is defined as the Néel temperature (T_N). For paramagnetic materials on the other hand, have an inverse linear relationship with temperature. Diamagnetic materials, where all the electrons are paired, have small negative χ values.[45]

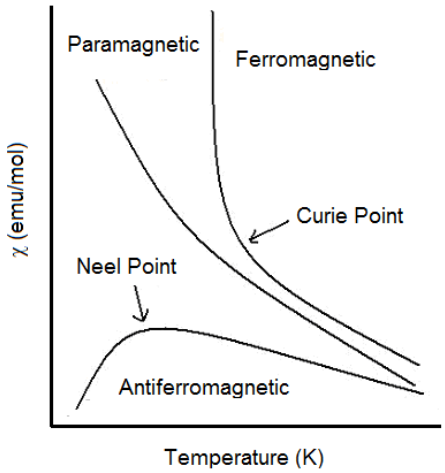

Figure 1.13. Susceptibility response of changing temperature of different types of magnetism.

For paramagnets, the relationship between χ and absolute temperature (T) is described by the Curie Law (shown in equation 1.11). The Curie constant (C) is given by equation 1.12, where N_A is the Avogadro constant, μ is the molecular magnetic moment and k is the Boltzmann constant. The Curie Law is the magnetic analogue of the ideal gas law, which only applies when there are no intermolecular interactions.

$$\chi = \frac{C}{T} \tag{1.11}$$

$$C = \frac{N_A \mu^2}{3k} \tag{1.12}$$

In the presence of magnetic exchange pathways which provide magnetic communication between neighboring molecules, the material may exhibit ferromagnetism or antiferromagnetism. In this situation, the Curie-Weiss Law is used, as shown in equation 1.13. The Weiss constant θ (defined in equation 1.14) takes into account the magnetic exchange interactions between electrons which are defined in terms of the exchange parameter ***J***. In this equation S is the total spin quantum number.

$$\chi = \frac{C}{(T - \theta)} \tag{1.13}$$

$$\theta = \frac{zJS(S+1)}{3k} \tag{1.14}$$

A plot of $1/\chi$ as a function of temperature for the Curie-Weiss Law yields a straight line with slope equal to $1/C$ and $-\theta/C$ as the intercept (illustrated in Figure 1.14a). For a ferromagnetic material, the electrons in neighboring molecules are aligned parallel (↑↑) and both J and θ are positive, while in antiferromagnetic materials the anti-parallel alignment (↑↓) of spins is associated with negative J and θ values.[35]

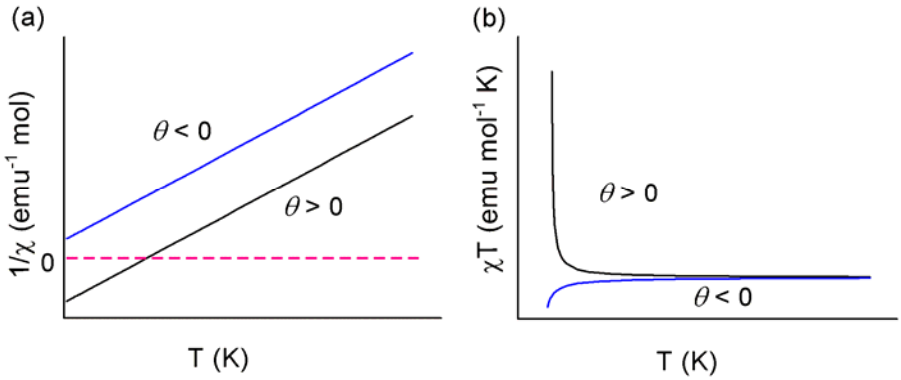

Figure 1.14. Plots of (a) $1/\chi$ as a function of temperature and (b) χT as a function of temperature for Curie-Weiss Law with positive (black) and negative (blue) Weiss constants.

Commonly, magnetic data is presented as a plot of χT *vs.* T in order to facilitate observation of small changes in susceptibility with temperature. In these plots, a positive θ leads to an increase in to χT value, while a negative θ results in a decrease in the χT value upon cooling (shown in Figure 1.14b).

The magnetic susceptibility can be measured in a number of ways. Commonly it is measured by a superconducting quantum interference device (SQUID). The experimental data consists of the sum of three components as shown in equation 1.15. Diamagnetism (χ_{dia}) as mentioned earlier is always there and has a negative value. It can be accounted for by several ways, for example measure the susceptibility of empty sample holder, and use Pascal′s constant to calculate the value.

$$\chi_{exp} = \chi_{dia} + \chi_{sample} + \chi_{TIP} \qquad \textbf{(1.15)}$$

Temperature independent paramagnetism (χ_{TIP}), which arises from the mixing between different states, is usually small and has positive sign. Usually this term is assumed to be zero. Another form of temperature independent paramagnetism is called Pauli paramagnetism, which is observed in the

materials that display metallic conductivities. After correcting for both χ_{dia} and χ_{TIP} terms, χ_{sample} can now be extracted from the experimental data.

1.11 Saturation Magnetization[44]

For paramagnetic materials, the susceptibility χ is independent of field when the field is weak, that is to say, the magnetization M increases linearly with field H. When H becomes large, the magnetization (M) of the system reaches saturation. The saturation magnetization (M_{sat}) can be calculated following equation 1.16. Since M_{sat} is usually expressed in the unit of $N\beta$, its value is simply given by gS, where S is the total spin angular momentum quantum number.

$$M_{sat} = N_A g S \beta \qquad \textbf{(1.16)}$$

The g value can be estimated by equation 1.17. When there is only spin contribution (*i.e.,* total orbital angular momentum quantum number $L = 0$, total angular momentum quantum number $J = L + S = S$), g is predicted to be 2, but the real value is equal to 2.002 for a free electron. When there is spin orbit coupling, g value can dramatically deviate from 2.

$$g = 1 + \frac{S(S+1) - L(L+1) + J(J+1)}{2J(J+1)} \qquad \textbf{(1.17)}$$

The magnetic moment (μ) then can be calculated using $\mu = \mu_{eff}\beta$, where $\mu_{eff} = g\sqrt{J(J+1)}$. For paramagnetic materials, χT is proportional to the square of μ_{eff} (equation 1.18) . Thus for a given S (assume $g = 2$), a plot of χT *vs.* T should reach a standard number in the high temperature region, regardless of whether it is a ferromagnets or antiferromagnets. This is often used to check the purity of the sample. For example, for a pure sample of $S = ½$ radicals with one unpaired electron, χT should reach 0.375 emu mol^{-1} K at high temperature (*i.e.*, room temperature). The presence of closed-shell impurities will reduce this value.

$$\mu_{eff} = \sqrt{\frac{3k\chi T}{N_A \beta^2}} \approx \sqrt{8\chi T} \qquad \textbf{(1.18)}$$

For ferromagnetic materials, magnetization increases rapidly with increasing field, until all of the spins are co-aligned. At this point the magnetization becomes saturated. If the field is removed, some, but not all the ordering, is lost. The residual magnetization when $H = 0$ is referred to as the remnant magnetization M_r. In order to reduce the value of M to zero, that is to destroy the alignment of the spins, a reverse field must be applied. The magnitude of the reverse field required to quench the magnetization is referred to as the coercive field H_c.[46] Forward and backward cycling of the magnetic field affords a magnetic hysteresis loop, which is characterized by the values of M_r and H_c. The so-called hardness of a magnet is proportional to the H_c value - a hard magnet has a large H_c value, while a soft magnet has a small H_c value. The typical hysteresis loops of hard and soft magnets are illustrated in Figure 1.15. The magnitude of H_c is an important parameter in determining the potential applications of a magnetic material. Hard magnets, for example, are required for data storage, while soft magnets find applications in transformers.

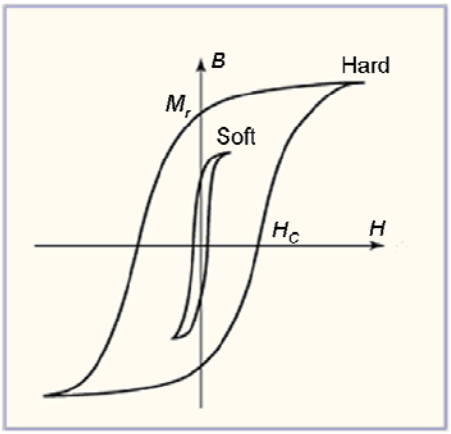

Figure 1.15. Hysteresis loops for soft and hard magnets.

At a microscopic level, the magnitude and sign of magnetic exchange interactions can be related to the overlap between SOMO orbitals.[47] Ferromagnetic exchange is observed when the net overlap between orbitals is zero, which is defined as orthogonal overlap. Mathematically this condition can be represented as equation 1.19.

$$\int \phi^* \phi d\tau = 1 \qquad \int \phi\varphi d\tau = 0 \tag{1.19}$$

In order to achieve orthogonal overlap, there must be equivalent amounts of bonding and anti-bonding character between two overlapped orbitals, shown in Figure 1.16. Mathematically the two orbitals are orthogonal, the overlap integral *S* is equal to zero, which is given by $S = \int \psi_i^* \psi_j d\tau = 0$. When $S = 0$, the material orders ferromagnetically. On the other hand, a strong bonding ($S > 0$) or antibonding overlap ($S < 0$) would give rise to antiferromagnetic exchange. Since the condition for ferromagnetic interactions is very strict, radical based ferromagnts are very rare (see below).

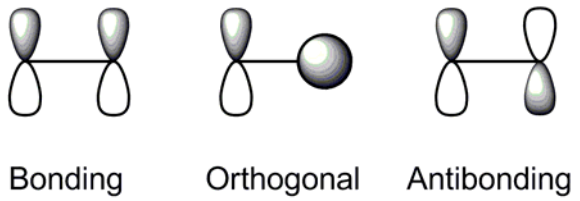

Figure 1.16. Model orbital overlaps, with bonding, orthogonal and antibonding interactions.

1.12 Development of S-N Based Radical Magnets

The pursuit of radical-based magnetic materials has been ongoing for several decades.[35] One of the goals has been to control the packing of radicals in the solid state so that the magnetic exchange interactions between them are ferromagnetic. Extensive work on the magnetic properties of localized, light heteroatom radicals, such as nitroxyls, nitronyl nitroxides, verdazyls, and dithiadiazolyls, has yielded a few examples that order ferromagnetically.[35,48] The ordering temperatures (T_C) of these materials are, however, well under 5 K, and the coercive fields (H_c) are never more than a few Oersted. Spin-canted antiferromagnetic ordering (weak ferromagnetism) has been observed in an oxoverdazyl at 5.4 K,[49] and also in the dithiadiazolyl **1-20** at 36 K.[50] Replacing the cyano group of **1-20** with a nitro group gave species **1-21** exhibiting ferromagnetic ordering at 1.32 K.[51]

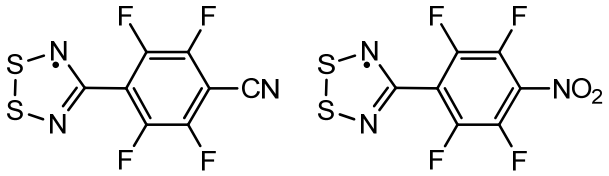

1-20 **1-21**

Work in the Oakley group on bisdithiazolyls and their selenium containing analogues has led to the discovery of some materials with remarkable properties, including metamagnetism,[52] spin-canted anti-ferromagnetism[53] and ferromagnetism.[54] The ferromagnetic materials have evoked particular interest, as their ordering temperatures (the highest of which is 17 K) are an order of magnitude higher than observed for any other non-metal radical based magnetic material. In addition, their coercive fields are 2 to 3 orders of magnitude greater than observed before in an organic material, the highest of which is 1320 Oe at 2 K.

Recent studies of the pressure dependence of the structure and magnetic properties of **1-12** (R_1 = Et, R_2 = Cl) showed that under pressure there was a change in the degree of π-stack slippage. As a result the overlap between the SOMO of the adjacent radicals changed from bonding to orthogonal overlap then to antibonding with increasing pressure, as shown in Figure 1.17. Consistently, magnetic susceptibility measurements indicated that T_C initially rose to a maximum of 21 K near 0.9 GPa, but with increasing pressure, the T_C value retreated back to the original value of 16 K at ~ 4 GPa.[55]

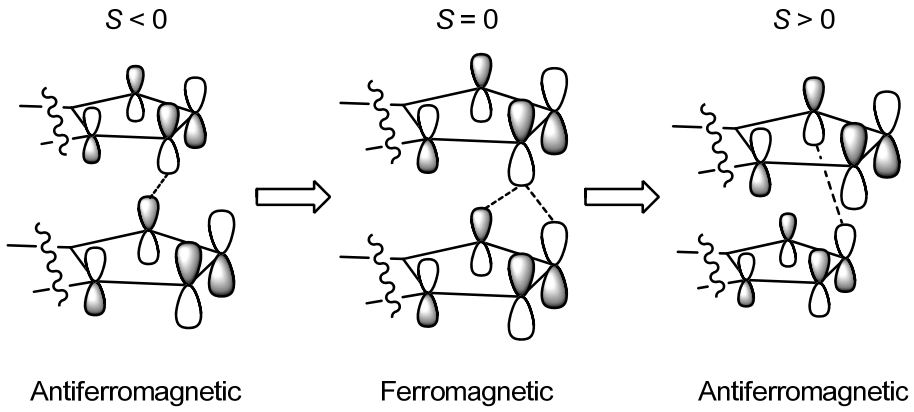

Figure 1.17. Schematic diagram of SOMO orbital overlap change as increase pressure.

This latter work demonstrates the importance of studying and understanding the complex relationships among molecular structure, crystal structure and transport properties of molecular radicals. These issues are central to the research work in my M.Sc. studies.

1.13 Thesis Scope

Recently the Passmore group has reported a family of 1,4-quinone bridged *mono*- and *bis*-1,3,2-DTA radicals, biradicals and radical cations.[56] These materials either dimerize in the solid state or cannot be easily isolated. Conductivity and magnetic studies have shown that most of them are Mott insulators and antiferromagnets. However, the close packing of these quininoid based systems, in principle, should give rise to strong π-overlaps, which could enhance the bandwidth *W* and increase the conductivity. This led to the development of semiquinone-bridged *bis*-dithiazolyl radicals **1-22** as potential building blocks to achieve high conductivity and exhibit interesting magnetic properties.

During my graduate work, a family of **1-22** radicals has been prepared, characterized and studied. The synthetic details and characterization of this family of compounds are presented in Chapter 2 in this thesis and crystallographic data (single crystal X-ray crystallography or powder X-ray crystallography) are reported in Chapter 3. Chapter 4 is dedicated to transport and magnetic property studies of these radicals. The preliminary results of the preparation of the Se analogue of **1-22** are summarized in Chapter 5 along with some on-going progress and potential future work.

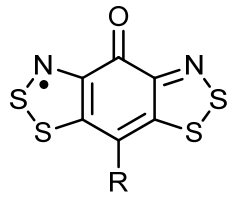

1-22

Chapter 2

Synthesis

2.1 Introduction

Monofunctional 1,2,3-dithiazolyl (1,2,3-DTA) radicals have been known for over 30 years,[1] however until recently they were little more than spectroscopic curiosities.[2] Typically there are two ways to prepare this ring system, (i) the cyclo-condensation reaction of an aromatic amine with sulphur monochloride (S_2Cl_2) which was first reported by Herz (equation 2.1),[3] and (ii) the addition reaction of S_2Cl_2 to an aliphatic nitrile (Appel's method (equation 2.2)).[4]

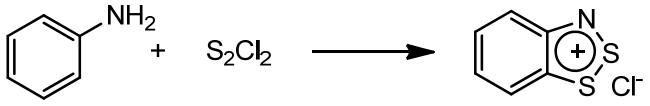

(2.1)

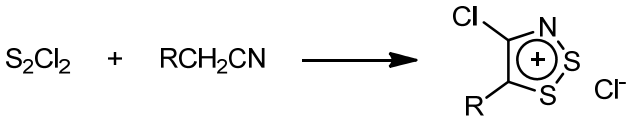

(2.2)

While the 1,2,3-dithiazolyl radicals were first observed in solution by EPR spectroscopy in the 1980s,[2] it was not until 1999 that Barclay *et.al.* isolated the first stable 1,2,3-DTA radical (**2-1**, R = C_6F_5).[5] The benzo-1,2,3-DTA (**2-2**) can be generated in solution by chemical or electrochemical reduction,[2] but is highly reactive and the isolation of this compound has not been reported. During the past 10 years, the Oakley group has prepared and structurally characterized a series of bifunctional 1,2,3-DTA radicals (**2-3**). These radicals are resonance stabilized and typically remain unassociated in the solid state, a feature which leads to interesting transport and magnetic properties.[6]

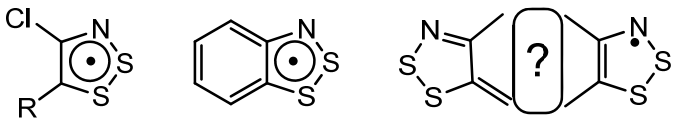

2-1 **2-2** **2-3**

The pyridyl based *bis*-dithiazolyl (R_2BPR_1, **2-13**) radicals can be prepared in several synthetic steps, starting from the 2,6-diaminopyridine. The double Herz cyclocondensation reaction of S_2Cl_2 with 2,6-diaminopyridine leads to [**2-5**][Cl], which is metathesized to give **2-6**. Proton Sponge is then used to prepare the zwitterion **2-7**, followed by alkylation to afford [**2-8**][OTf] and a subsequent reduction to give the radicals **2-8**. Chlorination occurs at the 4-position of the pyridine ring during the double Herz reaction with high yield (shown in Scheme 2.1).[6a]

Scheme 2.1

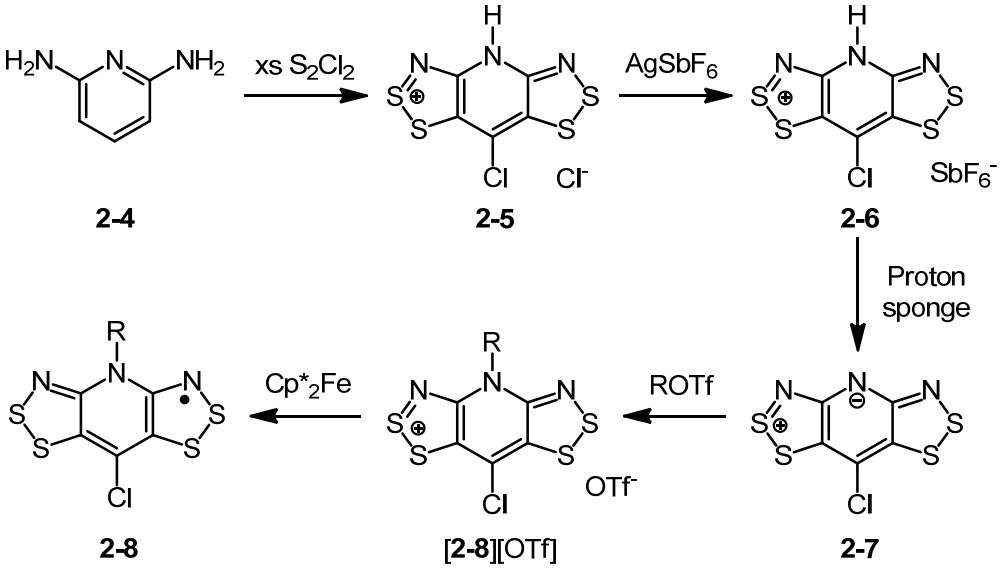

2-4 **2-5** **2-6** **2-7** **2-8** [**2-8**][OTf]

The exploration of this framework has led to a variety of R_1 (alkyl groups) and R_2 (halogens and methyl and phenyl groups) which are prepared by a double Herz reaction on the alkylated 2,6-diaminopyridine, as shown in Scheme 2.2, to give the bifunctional cyclic system. In the case of R_2 = Br, the Br atom was attached after the double Herz reaction.[7]

Scheme 2.2

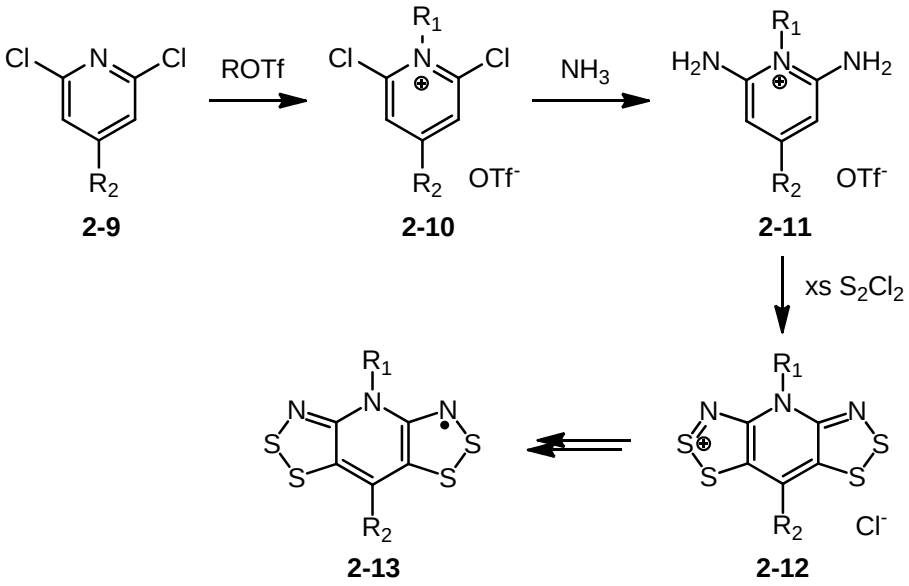

In 2005, Passmore *et. al.* first reported the quinone based 1,3,2-dithiazolylium (DTA) cations (**2-16**), and their corresponding radicals.[8] A new class of 1,4-quinone based 1,3,2-DTA radicals and radical cations were reported since then. In general, the corresponding cations can be prepared from readily available starting materials by a cycloaddition reaction and oxidative dehydrogenation with $SNS^{+}MF_6^{-}$ (M = As, Sb) in liquid SO_2, leading to the hydroquinone fused 1,3,2-DTA cations (**2-15**). The 1,4-benzoquinone fused 1,3,2-DTA cations (**2-16**) were then prepared by oxidation with AsF_5 in the presence of triethylamine (as shown in Scheme 2.3).[9]

Scheme 2.3

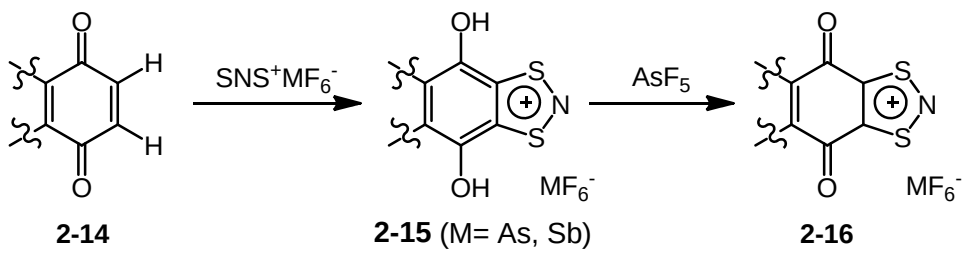

2.2 General Procedures

Semiquinone-bridged *bis*-dithiazolyls (RBBO, **2-19**) are isolobal to the pyridyl based *bis*-dithiazolyl (R_2BPR_1, **2-13**) radicals, and in principle a similar synthetic route can be employed. The first derivative of this family to be prepared was R = Cl. In the pyridine-birdged framework, under reflux condition in MeCN a double Herz reaction on 2,6-diaminopyridine (**2-11**) gives chlorinated *bis*-DTA chloride. Following the same logic, under reflux conditions, the double Herz reaction on 2,6-diaminophenol *bis*-hydrochloride (**2-18a**), which was prepared according to the literature procedure,[10] led to [**2-19b**][Cl] (shown in Scheme 2.4).

Scheme 2.4

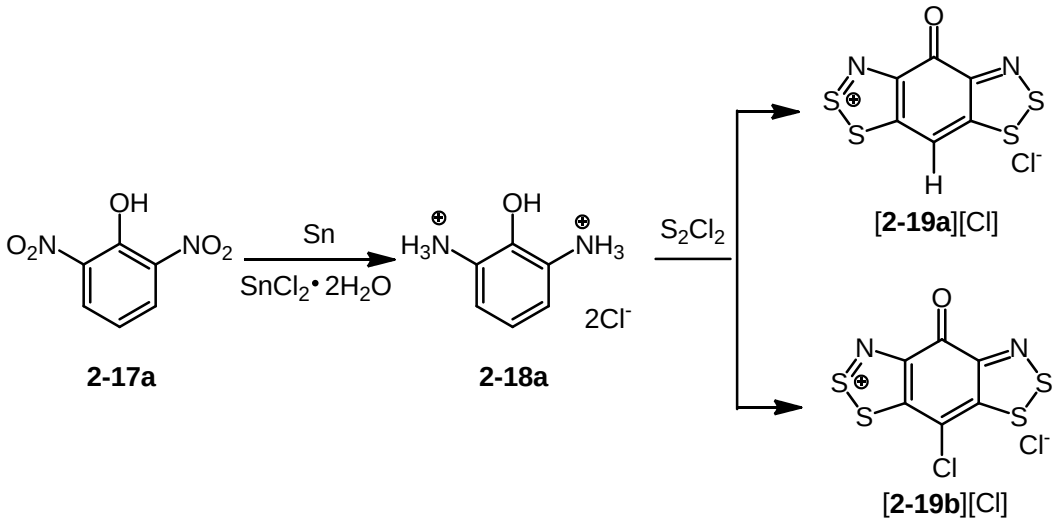

However, the reaction did not give 100 % of the desired product, [**2-19b**][Cl]. Instead, a 2:1 mixture of [**2-19b**][Cl] and [**2-19a**][Cl] was observed. After metathesis of the mixture of chloride salts with $GaCl_3$ to give the soluble gallates, all the [**2-19a**][$GaCl_4$] was converted to [**2-19b**][$GaCl_4$] using freshly prepared $PhICl_2$. Pure [**2-19a**][Cl] can be prepared by cold double Herz reaction at -35 °C in the presence of NEt_3.

Alternatively, the metathesis of 2,6-diaminophenol *bis*-hydrochloride (**2-18a**) with silver trifluoromethanesulfonate (sliver triflate, AgOTf) in MeCN gave the soluble 2,6-diaminophenol as a *bis*-triflate salt (**2-20**). The subsequent double Herz reaction with S_2Cl_2 in refluxing MeCN gave a mixture of [**2-19b**][OTf] and a OTf^- salt of an iminoester which results from a Pinner reaction between **2-20** and the solvent MeCN, according to Scheme 2.5. The chlorination of phenol in the 5-position prevents the cyclocondensation reaction of the Pinner adduct (**2-21**) with S_2Cl_2. However triturating the isolated solid with acetic acid removes the soluble Pinner salt and allows isolation of [**2-19b**][OTf].

Scheme 2.5

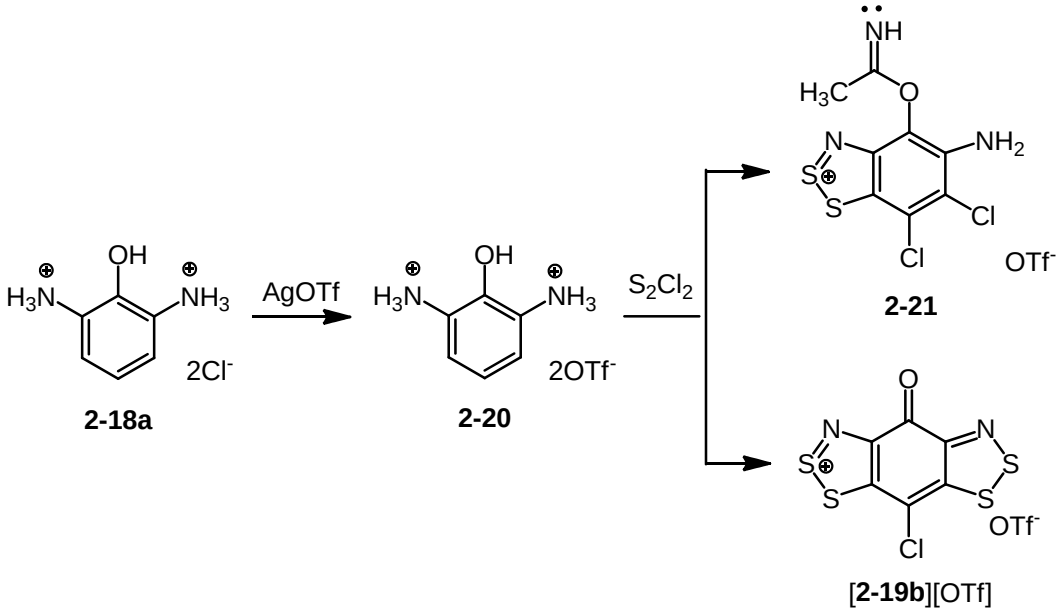

2-18a **2-20** **2-21** [**2-19b**][OTf]

Since the 2,6-dinitrophenol (**2-17a**) is very expensive, an efficient synthetic route to a salt of [**2-19b**]$^+$ was developed starting from 4-chlorophenol (**2-17b**) (see Section 2.2), and a general synthetic route to a series of 4-substituted semiquinone bridged *bis*-dithiazolyls (RBBO) was designed as shown in Scheme 2.6.

Scheme 2.6

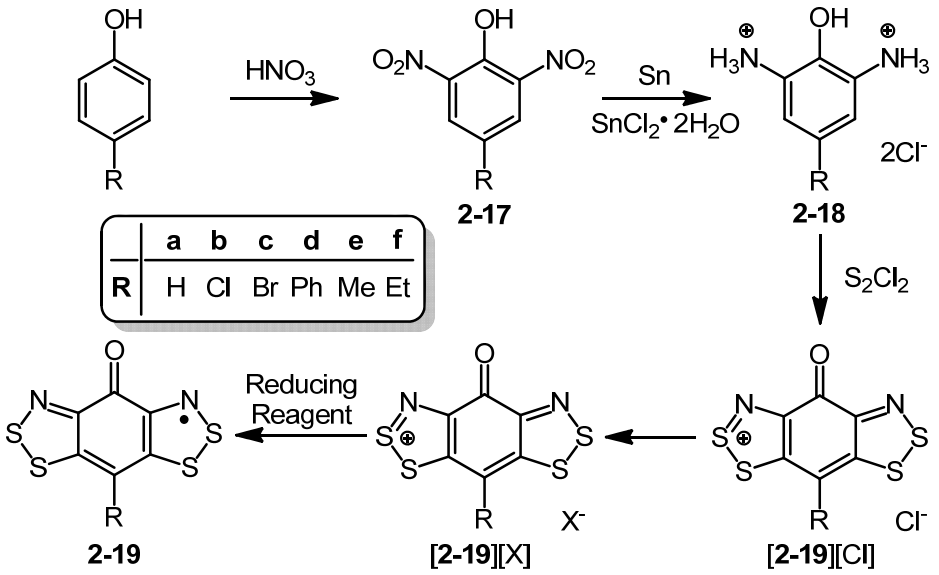

The nitration of 4-substituted phenol with HNO_3 gave 4-substituted 2,6-dinitrophenol (**2-17**), which was subsequently reduced to 4-substituted 2,6-diaminophenol *bis*-hydrochloride (**2-18**). A double Herz cyclocondensation of the latter with sulfur monochloride (S_2Cl_2) in refluxing MeCN then afforded the semiquinone-bridged *bis*-DTA chloride ([**2-19**][Cl]), which could be converted by a metathesis reaction into soluble semiquinone-bridged *bis*-DTA salts ([**2-19**][X]). All these salts give a dark purple solution in MeCN, which have a maximum absorption in the green color range in the UV-visible spectrum. The radicals (**2-19**) were prepared by reducing the soluble salts ([**2-19**][X]) with ferrocene derivatives (*i.e.,* $(Me_nCp)_2Fe$, n = 1, 4, 5).

2.2.1 Nitration Reaction

Classically the nitration of aromatics involves nitric acid (HNO_3), nitrogen oxide gas or NO_2^+ salts in the presence of a strong acid (*i.e.,* concentrated sulfuric acid (H_2SO_4), poly-phosphoric acid *etc.*).[11] These methods are widely used in industry, however, they produce a large amount of nitrogen oxide and acid waste.[11-12] A variety of new methods have been developed that involve the use of

heterogeneous catalysts, which are easily recycled, and help minimize acid waste, however most of these catalysts are transition metal based (*e.g.,* $Zn(NO_3)_2(N_2O_4)_2$) and are not commercially available. In addition, these types of nitration reactions are usually only used in small scale reactions (*i.e.,* ~ 1 mmol of starting material).[13] Considering the dinitro compounds are the starting material for a multi-step synthesis of RBBO radicals, the traditional method (with HNO_3) was used to prepare 4-substituted 2,6-dinitrophenol in large quantities, with the exception of R = H and Me (**2-17a**, **e**) both of which commercially available.

A variety of synthetic methodologies for the preparation of 4-chloro-2,6-dinitrophenol (**2-17a**) have been reported in the literature.[14] Following the traditional method, using HNO_3, it can be prepared by nitrating 4-chlorophenol with HNO_3 in dichloromethane (DCM) at ambient temperature for 45 min to give 4-chloro-2,6-dinitrophenol. When the nitration reaction is carried out in chloroform at low temperature (*e.g.,* -60 °C), *ipso* nitration (*i.e.,* 4-chloro-4-nitrocyclohexa-2,5-dienone) is observed, which undergoes a rapid rearrangement at higher temperature to give 4-chloro-2-nitrophenol.[15] The 4-chloro-2-nitrophenol can be prepared using HNO_3 in acetic acid solution at 40 °C for 1 h.[16] In our case, the 4-chlorophenol was nitrated with diluted 68 % HNO_3 in acetic acid to give 4-chloro-2-nitrophenol. The reaction mixture was stirred at room temperature with a water bath and poured onto crushed ice after 30 min to yield a light yellow crystalline product. The solid was collected by filtration and the ^1H NMR spectrum was consistent with reported 4-chloro-2-nitrophenol.[15] The addition of 98 % H_2SO_4 to a suspension of 4-chloro-2-nitrophenol in HNO_3 at 0 °C gave 4-chloro-2,6-dinitrophenol. The overall isolated yield for the stepwise nitration of 4-chlorophenol to 4-chloro-2,6-dinitrophenol was *ca.* 75 %. It was also found that 4-chloro-2,6-dinitrophenol could be achieved by heating a mixture of HNO_3 and 4-chlorophenol in acetic acid at 70 – 80 °C for 45 min to yield 4-chloro-2,6-dinitrophenol in 85 % isolated yield. When the reaction was performed at lower temperature, a mixture of 4-chloro-2-nitrophenol and 4-chloro-2,6-dinitrophenol was produced, due to their low solubility in acetic acid. The ^1H NMR chemical shifts were consistent with the reported chemical shift in the literature.[15]

The previously reported nitration of 4-bromophenol was carried out with 68 % HNO_3 in acetic acid at 70 °C for 10 min, leading to 4-bromo-2,6-dinitrophenol (**2-17c**). Several attempts to repeat this procedure did not lead to the expected product 4-bromo-2,6-dinitrophenol. However, a yellow crystalline solid was isolated, which was consistent with 4-bromo-2,5-dinitrophenol (mp 51 – 52 °C) based on ^{1}H NMR. Therefore, the stepwise nitration of 4-bromophenol was carried out analogously to 4-chlorophenol. The nitration of 4-bromophenol with 68 % HNO_3 was carried out in acetic acid at 0 °C for 1 h to give a mixture of 4-bromo-2-nitrophenol and 4-bromo-2,6-dinitrophenol. The mixture was recrystallized from a 1:1 mixture of dichloromethane and pentane to give yellow needles of analytically pure 4-bromo-2-nitrophenol (mp 87-89 °C; lit.[17] mp 87 °C) in *ca.* 80 % yield. The subsequent nitration of 4-bromo-2-nitrophenol in a mixture of HNO_3 and H_2SO_4 at a carefully controlled temperature of 50 °C gave a mixture of 4-bromo-2,6-dinitrophenol (**2-17c**) and picric acid (~ 7 : 3 respectively). Repeated recrystallization from 80 % ethanol led to analytically pure 4-bromo-2,6-dinitrophenol (mp 74.5-75 °C; lit.[18] mp 74.5 °C).

The nitration of 4-phenylphenol was carried out by a modified literature procedure,[19] using a mixture of HNO_3 and H_2SO_4 instead of 15 M HNO_3 (white fuming nitric acid) in acetic acid as previously reported. This led to 2,6-dinitro-4-phenylphenol (**2-17d**) in high yield (*ca.* 90 %) and subsequent recrystallization from hot acetone gave light yellow blocks (mp 153-154 °C; lit. mp 155-157 °C), and the ^{1}H NMR was consistent with the literature spectrum.[19]

The previously reported nitration of 4-ethylphenol with HNO_3 in acetic acid gave 4-ethyl-2,6-dinitrophenol in 60 % isolated yield, however, because of the low melting point (*i.e.*, 36 °C), the corresponding morpholine and cyclohexylamine salts were isolated and characterized in unspecified yield.[20] The nitration of 4-ethylphenol in dichloromethane (DCM) with HNO_3 at 0 °C for 1 h led to 4-ethyl-2,6-dinitrophenol (**2-17f**) in essentially quantitative yield (by ^{1}H NMR) and subsequent passing of ammonia gas through the solution led to the isolation of the corresponding ammonium salt (**2-22**) by

filtration (shown in Scheme 2.7). Recrystallization of the ammonium salt from 50 % ethanol gave orange needles in *ca.* 70 % overall yield.

Scheme 2.7

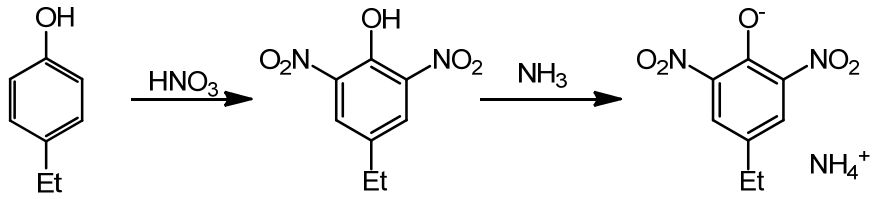

2-17f **2-22**

2.2.2 Tin Reduction

The reduction of nitro compounds is a synthetically useful route to amines and the literature is replete with examples of the reduction of one or more nitro moieties in the same molecule. The most effective synthetic methodologies involve catalytic hydrogenation over Pd / C with H_2 gas at high pressure[21] or using hydrazine in the presence of inexpensive metals (*e.g.,* Mg, Zn),[22] however these methods are typically effective only in small scale reactions. Alternatively the nitro group can be reduced to the free amine in high yield by sodium hydrosulfide[23] or sodium hydrosulfite[19,24] under basic conditions. Another common procedure for the large scale reduction of nitro moieties to amines (as their hydrochloride salt) in the literature involves $SnCl_2$ and / or Sn as the reducing reagent in the presence of acid, however the isolated yields are typically lower than the other methods (*e.g.,* hydrogenation over Pd / C with H_2 gas) discussed above.[25] In the case of the 4-substituted 2,6-diaminophenol compounds, the free amine can be rapidly oxidized in the presence of air,[19] which is one drawback of performing the reduction under basic conditions. Thus, the 2,6-diaminophenol *bis*-hydrochloride compounds were prepared by the reduction of their corresponding 4-substituted 2,6-dinitrophenol with Sn powder in the presence of $SnCl_2 \cdot 2H_2O$ in 36 % HCl.

At room temperature the dinitro compounds and $SnCl_2 \cdot 2H_2O$ were suspended in HCl. The reaction mixture was cooled to 0 °C and Sn powder was added in small portions. In solution, Sn reacts with HCl to give $SnCl_2$, which is a two-electron reducing agent, to give diaminophenol. The addition of $SnCl_2 \cdot 2H_2O$, which initiates the reaction, speeds up the reaction and helps maintain the solution acidity. Once all the Sn had reacted, the reaction mixture was allowed to warm to room temperature and was stirred for an additional hour, to give a yellow solution. Typically the reaction was preformed on a 0.1 mol scale of 4-substituted 2,6-dinitrophenol to isolate the desired products in larger quantity and moderate to high yield (*ca.* 60-80 %), compared with other methods discussed above. This general methodology was readily applied to R = H, Cl, Br, Me and Et, however the work up procedures were slightly different for each case, since the 4-substituded 2,6-diaminophenol *bis*-hydrochlorides (**2-18**) have different solubility. In the case of R = Cl and Br, bubbling HCl gas through the reaction mixture at 0 °C caused the product to precipitate as a white solid. The solid was washed with 36 % HCl and recrystallized from diluted HCl solution to yield white needles in *ca.* 60 % yield. The solubility of 2,6-diamino-4-methylphenol *bis*-hydrochloride (**2-18e**) in HCl solution was so high that bubbling HCl through the solution did not precipitate the product. Therefore the volatiles were distilled off under reduced pressure to leave a beige solid. The solid was slurried with a small volume of 36 % HCl to dissolve the Sn (IV) side-products and the crude product was collected by filtration. Repeated recrystallization of the crude product from diluted HCl gave white needles which were dried in vacuo at 110 °C overnight.

The reduction of the ammonium salt of 2,6-dinitro-4-ethylphenol (**2-22**) with Sn and $SnCl_2 \cdot 2H_2O$ led to a precipitate of NH_4Cl, (because of the low solubility of NH_4Cl in HCl,) which was removed by filtration, and 2,6-diamino-4-ethylphenol *bis*-hydrochloride (**2-18f**) was isolated as a white precipitate after bubbling HCl gas through the solution at 0 °C. The ^1H NMR of the isolated precipitate displayed a triplet at 7.14 ppm (J = 51 Hz) which is assigned to NH_4Cl. The crude product was dissolved in 95 % ethanol and the sparingly soluble NH_4Cl (0.6 g in 100 mL ethanol at 19 ºC)[26] was removed by filtration.

The ethanol was removed under reduced pressure and the off white solid was recrystallized by slowly cooling a hot solution of 4-ethyl-2,6-diaminophenol *bis*-hydrochloride (**2-18f**) in dilute HCl, to give white needles in *ca.* 65 % yield.

The reduction of 2,6-dinitro-4-phenylphenol (**2-17d**) with $Na_2S_2O_4$[19] or the small scale reduction with Pd/C in the presence of hydrazine monohydrate[21b] has previously been reported. The reduction with $Na_2S_2O_4$ however, could not be reproduced. A Sn reduction in acidic ethanol led to 2,6-diamino-4-phenylphenol *bis*-hydrochloride (**2-18d**) with moderate yield. Attempts to perform the Sn reduction 2,6-dinitro-4-phenylphenol in a suspension in HCl were unsuccessful because of the poor solubility and reactivity of 2,6-dinitro-4-phenylphenol compared to R = H, Cl, Br, Me, Et 2,6-dinitrophenols. The reduction of 2,6-dinitro-4-phenylphenol with $SnCl_2 \cdot 2H_2O$ and Sn in an ethanol and 36 % HCl mixture (4:1 v:v) with stirring at 0 °C was allowed to gradually warm to room temperature. Once all the Sn had reacted, the reaction mixture was refluxed for 3 h, then concentrated to 25 mL and cooled to room temperature. The solution was allowed to stand for 24 h at room temperature leading to 2,6-diamino-4-phenylphenol *bis*-hydrochloride as microcrystalline white solid, which was collected by filtration. Recrystallization of crude product from diluted HCl led to white needles in *ca.* 70 % yield.

2.2.3 Double Herz Condensation Reaction

The cyclocondensation of sulfur monochloride (S_2Cl_2) with aromatic amines to give dithiazolium chloride salts was first reported by Richard Herz in 1922.[3,27] Similar cyclocondensation reaction of S_2Cl_2 or SCl_2 with amines, amidines *etc.* leads to a wide range of sulfur-nitrogen ring systems, *i.e.*, preparation of 1,2,3-dithiazolylium salts (**2-23**),[6a] 1,2,4-thiadiazinylium salts (**2-24**),[28] 1,2,3,5-dithiadiazolylium salts (**2-25**),[29] and 1-chloro-1,2,4,6-thiatriazines (**2-26**).[30]

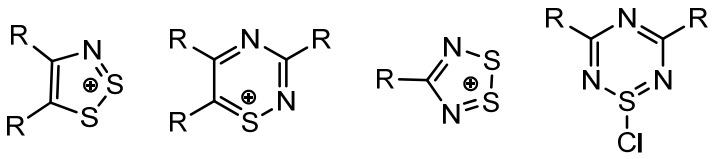

2-23 **2-24** **2-25** **2-26**

The preparations of the BP framework by the double Herz cyclocondensation reactions of S_2Cl_2 with 2,6-diaminopyridines (**2-11**) were typically performed in refluxing MeCN for 12-16 h. In solution, the cyclocondensation of S_2Cl_2 with 2,6-diaminopyridines readily occurs in the presence of NEt_3 in MeCN at 0 °C without chlorination at R_2, but chlorination is observed in the absence of NEt_3 leading to a mixture of R_2 = H and Cl.[6b] This is due to the formation of complexes of tertiary amines and S_2Cl_2 in solution which are good sulfuration reagents but poor chlorination reagents.[31]

The cyclocondensation of S_2Cl_2 with 4-substituted 2,6-diaminophenol *bis*-hydrochlorides (**2-18**) in refluxing MeCN over 8-16 h gave the chloride salt of the semiquinone-bridged *bis*-dithiazolyl ([**2-19**][Cl]) as a purple-black precipitate. The solid was collected by filtration under N_2, washed with MeCN, hot dichloroethane (DCE) and CS_2 to remove all the residual sulfur halides and sulfur, and finally dried *in vacuo*. In general the chloride salt was isolated in high (*ca.* 80 %) yield and this procedure was applied to a wide range of R-groups. According to our previous experience with the BP framework, the double Herz reaction of 2,6-diaminopyridine at low temperature avoided chlorination. The double Herz reaction of 2,6-diaminophenol *bis*-hydrochloride (**2-18a**) was first performed at 0 ºC in the presence of NEt_3, in dry MeCN for 4h, which led to a mixture of [**2-19a**][Cl] and [**2-19b**][Cl]. When the double Herz reaction was carried out in the presence of NEt_3 at -35 ºC, just above the freezing point of MeCN, only [**2-19a**][Cl] was obtained, based on Electro-Spray Ionization Mass Spectrometry (ESI-MS) of its gallate salt.

In the case of R = Br, the double Herz reaction between 0-20 ºC led to a mixture of [**2-19b**][Cl] and [**2-19c**][Cl] after 4 h because of the thermodynamically more favourable C-Cl bond (*c.f.* $E_{C\text{-}Cl}$ = 327.2 kJ/mol, $E_{C\text{-}Br}$ = 285 kJ/mol)[32]. Following a modified literature procedure,[33] as illustrated in Scheme 2.8, 4-bromo-2,6-dinitrophenol (**2-17c**) was methylated by refluxing a mixture of CH_3I in the presence of Ag_2O in dry $CHCl_3$ for 22 h. Recrystallization of the crude 4-bromo-2,6-dinitroanisole (**2-27**) from ethanol led to white needles in high yield (*ca.* 85 %), which can be subsequently reduced with $SnCl_2 \cdot 2H_2O$ and Sn metal (*vide supra*) to give the corresponding 4-bromo-2,6-diaminoanisole *bis*-hydrochloride (**2-28**) in *ca.* 60 % isolated yield.

Scheme 2.8

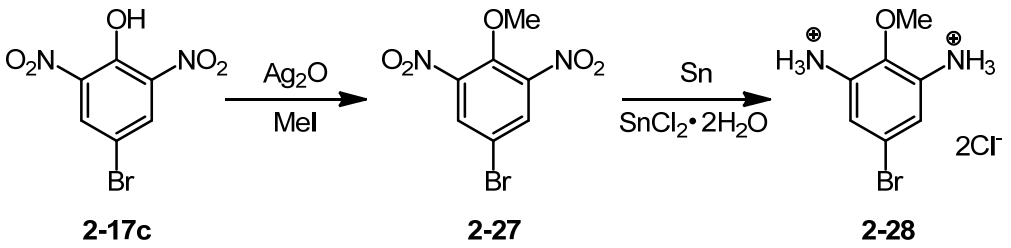

2-17c **2-27** **2-28**

The double Herz reaction of S_2Cl_2 with 4-bromo-2,6-diaminoanisole *bis*-hydrochloride (**2-28**) in refluxing MeCN overnight (8-16 h) gave a black precipitate of $[\mathbf{2\text{-}19c}]^+$ as the chloride salt in 80 % yield. The ESI-MS of $[\mathbf{2\text{-}19c}]^+$ as a triflate salt indicated the presence of small quantities of $[\mathbf{2\text{-}19a}]^+$ (less than 5 % by mass) which were formed during the double Herz reaction.

2.2.4 Metathesis Reaction

The double Herz reaction described above gives the desired chloride salt of RBBO which has negligible solubility in MeCN, however, the double Herz reaction is known to give rise to a number of by-products.[34] The metathesis of the chloride salt of RBBO obtained from the double Herz reaction with a silver salt (*e.g.,* AgOTf) or Lewis acid (*e.g.,* $NOSbF_6$) leads to the more soluble salts (*i.e.,* SbF_6^-, OTf^-,

BF_4^-, $GaCl_4^-$) which can be readily recrystallized from organic solvents (*i.e.,* MeCN, propionitrile (EtCN)) and are typically of high purity.

Typically, the OTf^- salt was chosen as the anion for the semiquinone-bridged framework based on its intermediate solubility in MeCN. Metathesis of [**2-19**][Cl] with AgOTf at reflux in MeCN for 1 h gives a dark purple solution. After all the AgCl was removed by filtration, the solvent was flash distilled off and the microcrystalline solid was triturated with an acetic acid and DCM mixture to remove unreacted AgOTf. Repeat recrystallization of crude [**2-19**][OTf] from saturated MeCN solutions led to analytically pure [**2-19**][OTf]. In some cases (*i.e.,* R = Cl, Br, Ph), the more soluble SbF_6^- salts were also prepared by treatment with $AgSbF_6$ or $NOSbF_6$ and the reasons will be discussed in the following sections (*i.e.,* reductions to the radicals, Se insertions). The SbF_6^- salts were prepared by the metathesis reactions of [**2-19**][Cl] with $NOSbF_6$ or $AgSbF_6$ at reflux in MeCN for 1 h, yielded a dark purple solution. After all the insoluble material was removed by filtration, the solvent was flash distilled off to leave a crystalline solid which was subsequently triturated with an acetic acid and DCM mixture and recrystallized from MeCN and/or EtCN.

The metathesis of [**2-19c**][Cl] with AgOTf gave [**2-19c**][OTf], which can be recrystallized to achieve high purity. A bromide salt was subsequently precipitated from [**2-19c**][OTf] using tetrabutylammonium bromide ($^nBu_4NBr$), to give pure [**2-19c**][Br]. The SbF_6^- salt can be prepared by metathesis of [**2-19c**][Br] with $NOSbF_6$, however, the presence of NO led to the substitution of Br by NO_2. Therefore $AgSbF_6$ was used instead of $NOSbF_6$ to perform the metathesis of [**2-19c**][Br] to give pure [**2-19c**][SbF_6] following the procedure previously described above.

The solubility of the alkyl substituted (*i.e.,* R = Me, Et) salt ([**2-19**][X]) in both MeCN and EtCN are much higher compared with the halogen substituted materials, especially for R = Et. The recrystallization of [**2-19f**][OTf] was attempted from both MeCN and EtCN, but it was not successful

due to the high solubility. A less soluble BF_4^- salt ([**2-19f**][BF_4]) was prepared by metathesis of [**2-19f**][Cl] with $NOBF_4$ in MeCN following the procedure described above. However the solubility was still too high to allow recrystallization, and a suitable counter anion is yet to be found.

2.3 Electrochemistry

The cyclic voltammetry of the semiquinone-bridged *bis*-dithiazolylium (R= Cl, Ph, Me) as the OTf^- salts were measured in MeCN solution, with 0.1 M $^nBu_4NPF_6$ as supporting electrolyte. The R = Cl, Ph, Me salts exhibit a reversible +1/0 couple, and an irreversible -1/0 couple. The cell potentials were estimated from the difference in the two cathodic peak potentials, using $E_{cell} = E_{pc}^{(0/+1)} - E_{pc}^{(-1/0)}$. The voltammograms are illustrated in Figure 2.1, and the E_{PC} and E_{cell} of R = Cl, Ph, Me are compared in Table 2.1.

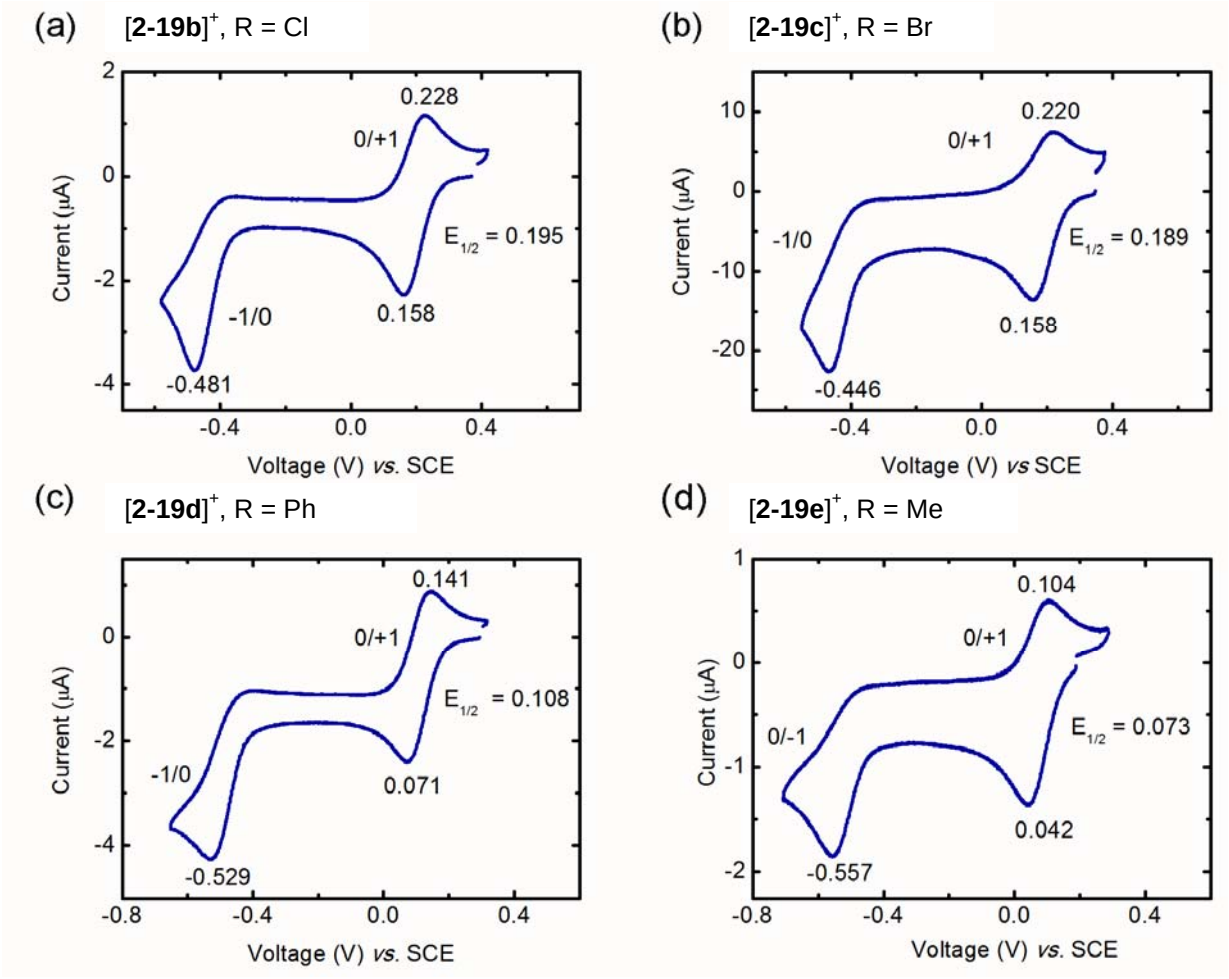

Figure 2.1. CV scans on solution of (a) [**2-19b**][OTf], (b) [**2-19c**][OTf], (c) [**2-19d**][OTf] and (d) [**2-19e**][OTf] in MeCN, using $^{n}BuPF_6$ as electrolyte and referenced to SCE.

Table 2.1. The cell potentials of **2-19 b, c, d, e** (R = Cl, Br, Ph, Me) in MeCN, compared with **2-12** (R_1 = Me, and R_2 = Cl).

	2-19				**2-12**
	Cl	Br	Ph	Me	R_1= Me, R_2 = Cl
$E_{pc}^{(+1/0)}$ (V)	0.158	0.158	0.071	0.042	$E_{1/2}^{(+1/0)}$ = 0.005 V
$E_{pc}^{(-1/0)}$ (V)	-0.481	-0.446	-0.529	-0.557	$E_{1/2}^{(-1/0)}$ = -0.835 V
E_{cell} (V)	0.639	0.604	0.600	0.599	E_{cell} = 0.840 V

As discussed in Chapter 1, the solution cell potential (E_{cell}) may be used to estimate the on-site Coulomb repulsion energy, U. [**2-19**]$^+$ (R = Cl, Br, Ph and Me) have smaller E_{cell}, (see Table 2.1) which were estimated from the difference between the cathodic potentials of the -1/0 and +1/0 couple, compared to the $E_{cell} \approx 0.8$ V[35] for the pyridine-bridged systems ([**2-12**]$^+$). Therefore, it is expected the lower E_{cell} and thus smaller U for the BB system should lead to better conductivity in the solid state than the BP framwork.

2.4 Preparation of the Radicals

Single crystals of X-ray quality were grown by slow diffusion of the solution of the cations (as their OTf^- or SbF_6^- salts) into a solution of a ferrocene derivative in an H-cell, which is described in the Appendix A.1.2. Octamethylferrocene ($E_{1/2}^{(+1/0)}$ = -0.038 V *vs.* SCE)[36] was chosen as the reducing reagent based on cyclic voltammetry, with the exception of [**2-19b**]·MeCN, which required dimethylferrocene ($E_{1/2}^{(+1/0)}$ = 0.263 V *vs.* SCE),[37] and [**2-19e**], which required decamethylferrocene ($E_{1/2}^{(+1/0)}$ = -0.131 V *vs.* SCE)[38] to perform the bulk reduction to increase the yield. All of the radicals formed lustrous black needles by the H-cell diffusion method; however attempts to obtain crystals by temperature gradient vacuum sublimation were unsuccessful because of thermal decomposition of the radical.

Even though based on the CV, **2-19b** radicals can be prepared by reduction with octamethylferrocene, the reduction of [**2-19b**][OTf] with octamethylferrocene in MeCN led to a microcrystalline solid of solvated radical (*i.e.,* ClBBO·MeCN adduct). The infrared spectrum had a sharp peak at 2246 cm^{-1} which is characteristic of a C≡N stretch (lit. 2250 cm^{-1})[39] and suggested the radical was solvated. Although the reduction potential of dimethylferrocene ($E_{1/2}^{(+1/0)}$ = 0.263 V *vs.* SCE)[37] is slightly lower than **2-19b** (*c.f.* $E_{1/2}^{(0/+1)}$ = 0.158 V *vs.* SCE), the reduction of [**2-19b**][OTf]

with dimethylferrocene led to single crystals of ClBBO·MeCN suitable for single crystal X-ray diffraction (XRD), which confirmed the presence of MeCN in the crystal lattice.

The salt of [**2-19b**][SbF_6] was prepared following the procedure described above (Section 2.4.4), however recrystallization of crude [**2-19b**][SbF_6] from MeCN led to solvated material, as shown by infrared spectrum and single X-ray crystallography. Therefore, the crude [**2-19b**][SbF_6] was recrystallized from EtCN to yield metallic green plate-like crystals, which were not solvated. The non-solvated radical was obtained by reduction of [**2-19b**][SbF_6] with octamethylferrocene in EtCN, due to the low solubility of the OTf^- salt in EtCN. In the case of R = Br, it behaves the same as R = Cl, therefore the solvated (**2-19c**·MeCN) and nonsolvated radicals (**2-19c**) were prepared the same way as the R = Cl species (**2-19b**·MeCN and **2-19b**).

Reduction of [**2-19e**][OTf] with octamethylferrocene by the H-cell diffusion method led to microcrystalline material, however several small crystals that were suitable for single crystal crystallography were isolated and the structure of the **2-19e** radical was obtained. The bulk reduction of [**2-19e**][OTf] with dicamethylferrocene in freeze-pump-thaw degassed MeCN for one hour led to a microcrystalline solid which has a comparable powder XRD pattern with the simulated powder pattern of the single crystal X-ray structure. In addition, the H-cell and bulk reduction product were both sparingly soluble in DCM and toluene and an EPR spectrum could not be obtained.

2.5 EPR Spectroscopy

The electron paramagnetic resonance (EPR) spectra of **2-19b** and **2-19d** were obtained in degassed DCM and toluene solution, respectively. In general, a five-line pattern was observed for both **2-19b** and **2-19d**, due to the hyperfine coupling between the unpaired electron and the two equivalent ^{14}N atoms. The spectra were simulated by Simfonia and WinSim software to obtain accurate hyperfine

coupling constants and g-values, which are reported in Table 2.2. Both the experimental and simulated spectra of **2-19b** and **2-19d** are illustrated in Figure 2.2.

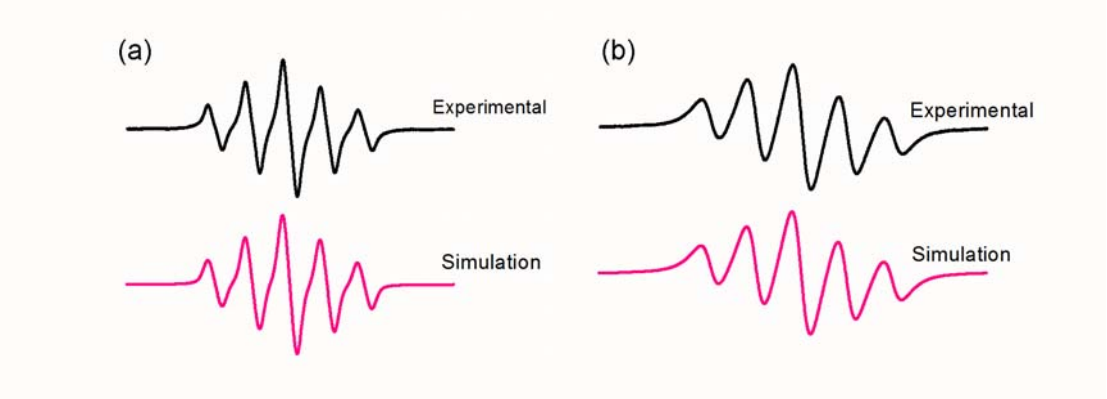

Figure 2.2. EPR spectra of (a) **2-19b** (in DCM) and (b) **2-19d** (in toluene) and their simulations with sweep width of 30 G.

Table 2.2. EPR measurements: *g*-values, hyperfine coupling constant and simulation parameters of **2-19b** in DCM and **2-19d** in toluene.

	2-19b	**2-19d**
g	2.0089	2.0092
a_N (G)	3.43	3.52
a_R (G)	0.32	0.8/0.3/0.5 (o,m,p)
L/G	0.7	0.75
LW (G)	0.3	0.85

For **2-19b**, in addition to the coupling to N (a_N = 3.43 G), there is a small hyperfine coupling to Cl (a_{Cl} = 0.323 G) which contributes to the line broadening. The hyperfine coupling to the protons of the Ph substituent in **2-19d** were not directly observed, but are estimated from the simulated EPR spectrum and also contribute to the observed line broadening in the experimental EPR spectrum. For both of these radicals, their *g*-value is slightly larger than the expected *g*-value for the free electron (g = 2.002), a difference that may be ascribed to spin-orbit coupling. From these two samples of semi-quinone based systems, the values of a_N are similar to that observed for **2-13** (R_1 = Me, R_2 = Ph) (0.320

mT),[6c] suggesting a similar spin distribution for the two systems. The solution EPR for **2-19c** and **2-19e** could not be obtained, due to its low solubility in organic solvents. However, in the case of **2-19e** the *in situ* reduction of [**2-19e**][OTf] with Zn gave a quartet of 1:3:5:3:1 quintet consistent with coupling to the proton of the methyl group (CH_3) and two equivalent N atoms. The spectrum had a very poor signal-to-noise ratio, and the signal could not be observed after 10 min, presumably because of the association of the radicals in solution.

In addition the spin distribution in these semiquinone-bridged radicals (**2-19**) has been obtained by means of Density Functional Theory (DFT) calculations at the UB3LYP/6-311G(d,p) level. Illustrations of the Kohn-Sham spin density surfaces of **2-19b** and **2-13** (R_1 = Me, R_2 = Cl) are shown in Figure 2.3, which indicate they are isolobal to each other.

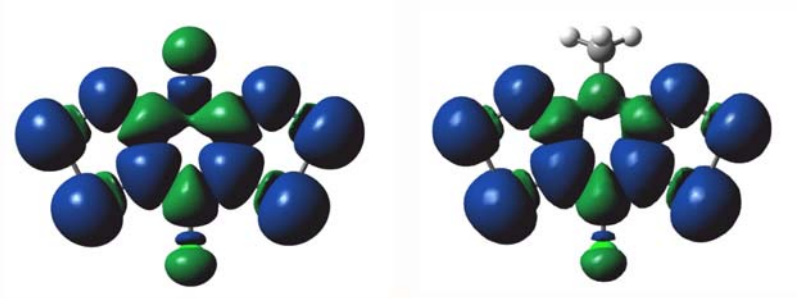

Figure 2.3. Calculated spin density surfaces of **2-19b** (left) and **2-13** (R1 = Me, R2 = Cl) (right).

2.6 Experimental Details

2.6.1 Preparation of 4-Substituted 2,6-Dinitrophenols (2-17)

Preparation of 4-chloro-2,6-dinitrophenol, 2-17b. Nitric acid (97 mL, 93.7 g, 1.49 mol) was added dropwise to a solution of 4-chlorophenol (45.0 g, 0.350 mol) in 300 mL of glacial acetic acid to yield a dark orange solution at room temperature. The mixture was stirred at 75 °C for 30 min and then poured on to crushed ice. The light yellow solid was collected by filtration, washed with H_2O and dried

in air to give 66.9 g (0.306 mol, 87 % yield), mp 79-80 °C (lit.[40] 80-81°C). ^{1}H NMR ($CDCl_3$) δ: 8.29 (s, 2H, Ph), 11.40 (s, 1H, OH).

Preparation of 4-bromo-2-nitrophenol. Nitric acid (6 mL, 5.79 g, 0.092 mol) was added dropwise to a solution of 4-bromophenol (14.5 g, 83.6 mmol) in 80 mL glacial acetic acid at room temperature over 5 min with stirring. The yellow solution was cooled in an ice-water bath for 45 min with stirring to give a yellow precipitate under a yellow-orange solution. The mixture was poured onto 400 mL of crushed ice. The solid was collected by filtration, washed with H_2O and dried in air to give 16.7 g (76.4 mmol, 91 % yield) of 4-bromo-2-nitrophenol. Recrystallization from dichloromethane/pentane gave yellow needles, mp 87-89 °C (lit.[17] 87 °C). ^{1}H NMR ($CDCl_3$) δ: 7.06 (d, J = 9 Hz, 1H, Ph), 7.74 (dd, J_1 = 9 Hz, J_2 = 3 Hz, 1H, Ph), 8.23 (d, J = 3 Hz, 1H, Ph), 10.46 (s, 1H, OH).

Preparation of 4-bromo-2,6-dinitrophenol, 2-17c. 4-bromo-2-nitrophenol (10.9 g, 0.050 mol) was suspended in 100 mL of HNO_3 and 40 mL H_2SO_4 was slowly added to the stirred mixture to give an orange solution. The temperature of the mixture was maintained below 50 ^{o}C with a water bath. The solution was stirred for 30 min and then poured onto 300 mL of crushed ice and allowed to stand until the ice melts. The yellow solid was collected by filtration, washed with H_2O to neutral and dried in air to give 9.43 g (0.036 mol, 72 % yield) of crude 4-bromo-2,6-dinitrophenol. Repeated crystallization from aqueous ethanol led to pure 4-bromo-2,6-dinitrophenol, mp 74.5-75 °C (lit.[18] 74.5 °C). ^{1}H NMR ($CDCl_3$): δ 8.42 (s, 2H, Ph), 11.31 (s, 1H, OH).

Preparation of 4-bromo-2,6-dinitroanisole, 2-27. A mixture of 4-bromo-2,6-dinitrophenol (8.78 g, 33.4 mmol), Ag_2O (7.35 g, 31.7 mmol) and MeI (3 mL, 48.2 mmol) in 150 mL of dry chloroform was refluxed at 60 °C for 22 h. The insoluble solid was removed by filtration, and all the solvent was removed under reduced pressure to give a light brown solid. Recrystallization from ethanol afforded

off-white needles of 4-bromo-2,6-dinitroanisole (8.48 g, 30.6 mmol, 92 % yield). ^{1}H NMR ($CDCl_3$) δ: 4.04 (s, 3H, Me), 8.14 (s, 2H, Ph).

Preparation of 2,6-dinitro-4-phenylphenol, 2-17d.[19] Concentrated nitric acid (20.0 mL, 19.3 g, 0.306 mol) was slowly added to a stirred suspension of 4-phenylphenol (20.2 g, 0.119 mol) in glacial acetic acid (100 mL). The reaction mixture was held in an ice/water bath for 45 min, then was poured onto 400 mL of crushed ice. The product was precipitated out as a bright yellow solid which was collected by filtration, yield 28.6 g (0.11 mol, 93 % yield), and recrystallized from acetone, mp 152-154 (lit.[19] 155-157 °C). ^{1}H NMR ($CDCl_3$) δ: 7.58-7.45 (m, 5H, Ar), 8.52 (s, 2H, Ar), 11.40 (s, 1H, OH).

Preparation of 4-ethyl-2,6-dinitrophenol, 2-17f and its ammonium salt, 2-22. HNO_3 (20 mL, 28.4 g, 0.451 mol) was added drop wise to a dichloromethane solution (80 mL) of 4-ethylphenol (20.8 g, 0.170 mol) at 0 °C to yield a dark orange solution. After stirring for 1 h, the solution was allowed to warm to room temperature and an additional 5 mL of HNO_3 was added. After 30 min of stirring at room temperature, 50 mL of water was added and the organic phase extracted with DCM. ^{1}H NMR ($CDCl_3$) δ: 1.28 (t, J = 7.5 Hz, 3H, CH_3), 2.72 (q, J = 7.5 Hz, 2H, CH_2), 8.14 (s, 2H, Ph), 11.28 (s, 1H, OH).

The ammonium salt (**2-22**) was prepared by bubbling NH_3 gas through the DCM solution at 0 °C to give orange brown precipitate. The solid was collected by filtration and recrystallized from aqueous ethanol to give 26.8 g (0.116 mol, 96 % yield) orange needles. ^{1}H NMR (DMSO) δ: 1.07 (t, J = 7.5 Hz, 3H, CH_3), 2.42 (q, J = 7.5 Hz, 2H, CH_2), 7.21 (s, 4H, NH_4), 7.63 (s, 2H, Ph). IR (cm^{-1}): 3203 (m, b), 1635 (s), 1621 (s), 1539 (vs), 1405 (s), 1364 (s), 1336 (s), 1271 (s), 1235 (vs), 1109 (w), 1067 (w), 937 (w), 914 (s), 902 (m), 824 (m), 784 (s), 754 (m), 716 (s), 596 (w), 506 (w).

2.6.2 Preparation of 4-Substituted 2,6-Diaminophenol *bis*-Hydrochloride (2-18)

Preparation of 2,6-diaminophenol bis-hydrochloride, 2-18a.[10] To a suspension of 2,6-dinitrophenol (4.00 g, 2.17 mmol) in 75 mL of concentrated HCl $SnCl_2 \cdot 2H_2O$ (2.46 g, 1.18 mmol) was added. The mixture was cooled on an ice-water bath and Sn powder (6.50 g, 5.47 mmol) was added slowly with vigorous stirring. When all the Sn had reacted, the reaction mixture was brought to boil for 1.5 h with adding 40 mL of HCl to give a brown solution. The brown solution was cooled in an ice-water bath to yield an off-white solid which was collected by filtration and washed with isopropanol. The isolated solid was recrystallized from 1:1 mixture of concentrated HCl and water to give the 2,6-diaminophenol *bis*-hydrochloride (2.23 g, 1.13 mmol, 52 % yield) as white needles which were dried *in vacuo* at 110 °C overnight, mp > 250 °C. ^{1}H NMR (DMSO) δ: 6.84 (t, 7.8 Hz, 1H, Ar), 6.95 (d, 7.8 Hz, 2H, Ar). IR (cm^{-1}): 3080 (s, br), 2638 (s, br), 1634 (s), 1613 (m), 1572 (s), 1557 (s), 1537 (vs), 1487 (s), 1404 (m), 1355 (m), 1316 (s), 1280 (s), 1228 (s), 1166 (w), 1132 (m), 1115 (m), 1068 (w), 1039 (w), 946 (w), 838 (m), 783 (s), 722 (s), 687 (w), 596 (m), 564 (m), 497 (m).

Preparation of 2,6-diamino-4-chlorophenol bis-hydrochloride, 2-18b. At 0 °C, a mixture of 4-chloro-2,6-dinitrophenol (25.1 g, 0.115 mol) and $SnCl_2 \cdot 2H_2O$ (26.1 g, 0.116 mol) was suspended in 100 mL of concentrated HCl. Sn powder (31.4 g, 0.264 mol) was added in three portions. After most of the Sn powder was reacted, HCl gas was passed through the cloudy solution for 2 min at room temperature. The reaction mixture was then stirred at 0 °C for additional 1 h. The precipitate was collected by filtration and washed with 20 mL of concentrated HCl. The solid was then recrystallized twice from a 1:1 (v:v) mixture of concentrated HCl and water. The off-white solid was dried at 110 °C under vacuum, yield 15.7 g (0.0679 mol, 59 % yield) white needles of product, mp 240 °C (dec.). Anal. Calcd. for $C_6H_9Cl_3N_2O$: C, 31.13; H, 3.29; N, 12.10. Found: C, 31.38; H, 3.71; N, 12.26. ^{1}H NMR (DMSO) δ: 6.72 (s, 2H, Ph), 7.61 (s, 7H, NH_3, OH). IR (cm^{-1}): 3417 (s, br), 1635 (s), 1570 (s), 1309 (s), 1267 (m), 1245 (s), 1219 (m), 1122 (w), 1061 (w), 973 (w), 903 (w), 863 (s), 762 (m), 716 (s), 601 (m), 536 (m).

Preparation of 4-bromo-2,6-diaminoanisole bis-hydrochloride, 2-28. 4-bromo-2,6-diaminoanisole *bis*-hydrochloride was prepared by the same method as 2,6-diamino-4-chlorophenol *bis*-hydrochloride, by slowly adding Sn powder (10.8 g, 0.091 mol) to a suspension of 4-bromo-2,6-dinitroanisole (10.0 g, 0.036 mol) and $SnCl_2 \cdot 2H_2O$ (8.21 g, 0.036 mol) in concentrated HCl (100 mL) at 0 °C. The mixture was stirred until the effervescence subsided, and allowed to warm to room temperature. A white precipitate was collected by filtration, washed with 2 × 20 mL concentrated HCl, air dried and recrystallized from 100 mL 1:1 (v:v) mixture of H_2O concentrated HCl to give 7.33 g (0.025 mol, 70 % yield) of 4-bromo-2,6-diaminoanisole *bis*-hydrochloride as white needles, mp 170 °C (dec.) ^{1}H NMR (DMSO) δ: 3.66 (s, 3H, Me), 4.07 (s, b, 6H, $2NH_3$), 6.69 (s, 2H, Ph). IR (cm^{-1}): 2538 (s, br), 1973 (s, br), 1940 (s, br), 1691 (w), 1601 (m), 1651 (s), 1507 (w), 1289 (m), 1237 (s), 1149 (s), 1107 (w), 1068 (m), 1031(m), 970 (s), 882 (s), 860 (m), 757 (s), 700 (w), 590 (w), 567 (w), 519 (m), 442 (m), 410 (m).

Preparation of 2,6-diamino-4-phenylphenol bis-hydrochloride, 2-18d.[21b] Tin powder (9.39 g, 79.1 mmol) was added slowly to a slurry of 2,6-dinitro-4-phenylphenol (10.1 g, 38.8 mmol) and $SnCl_2 \cdot 2H_2O$ (10.1 g, 44.7 mmol) in a mixture of ethanol (100 mL) and concentrated HCl (30 mL) held at 0 °C. After 30 min the reaction mixture was allowed to warm to room temperature and the resulting light yellow solution boiled for 3 h, then concentrated and cooled to room temperature. After 24 h the white solid was filtered off, washed with concentrated HCl and recrystallized from 1:1 (v:v) HCl:H_2O to afford **6c** (7.64 g, 28.0 mmol, 72.0 %), mp 220 °C (dec.) ^{1}H NMR (DMSO) δ: 7.31 (t, J = 7.2 Hz, 1H, Ar), 7.42 (t, J = 7.2 Hz, 2H, Ar), 7.65 (d, J = 7.5 Hz, 2H, Ar), 8.30 (s, 2H, Ar). IR (cm^{-1}): 3425 (w, br), 3358 (w, br), 2553 (w, br), 1940 (w, br), 1644 (w), 1577 (w), 1513 (s), 1487 (vs), 1333 (m), 1288 (m), 1235 (m), 1199 (w), 1115 (w), 1074 (w), 1021 (w), 972 (w), 878 (w), 762 (w), 694 (w), 621 (w), 608 (w), 514 (w).

Preparation of 2,6-diamino-4-methylphenol bis-hydrochloride, 2-18e. Tin powder (12.7 g, 0.107 mmol) was added in three portions to a suspension of 2,6-dinitro-*p*-cresol (5.5 g, 25 mmol) in 50 mL of concentrated HCl at 0 °C. When effervescence had ceased the mixture was allowed to warm to room temperature, then filtered through glass wool and the solvent removed from the filtrate by flash evaporation. The remaining solid was washed with 10-15 mL of concentrated HCl, then redissolved in 10-15 mL of de-ionized water to give a pale yellow solution. HCl gas was slowly bubbled through the solution for ~ 15 min until a white crystalline solid formed. The solid was collected by filtration and air-dried. A second, smaller portion of white solid crystallized from the filtrate and was also collected by filtration. Yield 5.0 g, 85%, mp > 250 °C Anal. Calcd. for $C_7H_{12}N_2OCl_2$: C, 39.83; H, 5.73; N, 13.27. Found: C, 40.01; H, 5.61; N, 13.41. ^{1}H NMR (DMSO) δ: 2.11 (s, 3H), 6.05 (s, 2H).[41] IR (cm^{-1}): 2721 (s, br), 2598 (s, br), 1645 (w), 1574 (m), 1549 (m), 1518 (s), 1498 (s), 1316 (m), 1285 (W), 1261 (m), 1222 (m), 1154 (w), 1125 (w), 1062 (w), 971 (w), 953 (w), 855 (m), 847 (m), 783 (m), 601 (m), 576 (m), 515 (w).

Preparation of 2,6-diamino-4-ethylphenol bis-hydrochloride, 2-18f. 2,6-diamino-4-ethylphenol *bis*-hydrochloride was prepared by a method similar to that used for 2,6-diamino-4-chlorophenol *bis*-hydrochloride. At 0 °C Sn powder (13.0 g, 0.109 mol) was added slowly to a slurry of the amino salt of 4-ethyl-2,6-dinitrophenol (10.0 g, 43.64 mmol) and $SnCl_2 \cdot 2H_2O$ (9.94 g, 44.1 mmol) in 75 mL of concentrated HCl. After most of the Sn was reacted, the reaction mixture was allowed to warm to room temperature and the white precipitate was removed by filtration. The HCl was then removed by distillation under reduced pressure to give white solid, which was washed with 10 mL of HCl. The isolated solid was dissolved in 100 mL of ethanol, followed by filtering off the insoluble NH_4Cl and evaporating all the ethanol. The isolated white solid was recrystallized from a 1:2 mixture of H_2O and HCl, yield 6.41 g (28.5 mmol, 65 % yield) product as white needles, mp > 250 °C. ^{1}H NMR (DMSO) δ: 1.09 (t, J = 7.5 Hz, 3H, CH_3), 2.49 (q, J = 7.5 Hz, 2H, CH_2), 7.06 (s, 2H, Ph). IR (cm^{-1}): 2536 (s, br), 1916 (w, br), 1880 (w, br), 1781 (w), 1646 (m), 1613 (w), 1597 (m), 1558 (s), 1522 (s), 1329 (s), 1276

(s), 1256 (m), 1223 (s), 1151 (m), 1115 (m), 1092 (s), 1061 (s), 1007 (w), 959 (m), 924 (w), 884 (s), 776 (m), 613 (m), 580 (m), 561 (w), 531 (w), 502 (w).

2.6.3 Preparation of Semiquinone-bridged *bis*-DTA Chloride [2-19][Cl]

Preparation of [2-19a][Cl]. At -35 °C S_2Cl_2 (0.800 g, 5.92 mmol) in 10 mL of MeCN was added dropwise to a slurry of 2,6-diaminophenol *bis*-hydrochloride (0.251 g, 1.39 mmol) and NEt_3 (1.5 mL, 2.07 g, 20.4 mmol) in 20 mL of MeCN to yield a black precipitate. After the reaction mixture was stirred at -35 °C for 4 h, the solid was isolated by filtration, washed with hot DCE and dried *in vacuo* to give [**2-19a**][Cl] (0.353 g, 1.26 mmol, 90.5 % yield). IR (cm^{-1}): 1666 (m), 1576 (s), 1320 (s), 1279 (m), 1232 (m), 1094 (w), 819 (w), 770 (w), 607 (w), 593 (w), 485 (w).

Preparation of [2-19b][Cl]. A slurry of 2,6-diamino-4-chlorophenol bis-hydrochloride **2-2a** (4.01 g, 17.3 mmol) and sulfur monochloride (11.7 g, 86.6 mmol) in 150 mL MeCN was heated at gentle reflux overnight. The resulting blue/black precipitate of [**2-19b**][Cl] was filtered off, washed with MeCN, hot DCE and finally CS_2 to remove residual sulfur and sulfur chlorides, and dried *in vacuo*, yield 4.21 g (13.2 mmol, 77 % yield) of solid, mp > 250°C. IR (cm^{-1}): 1671 (s), 1279 (s), 1097 (m), 1019 (m), 834 (m), 819 (m), 777 (m), 763 (m), 733 (m), 621 (w), 607 (w), 487 (m), 469 (m).

Preparation of [2-19c][Cl]. **[2-19c][Cl]** was prepared by the similar method as **[ClBBO][Cl]** using To 4-bromo-2,6-diaminoanisole *bis*-hydrochloride (2.06 g, 7.09 mmol) in 100 mL of dry CH_3CN and 3.4 mL S_2Cl_2 (~5.75 g, 42.5 mmol) at reflux for 8 h. The brown solid was filtered, washed thoroughly and dried *in vacuo* to give 2.35 g (6.53 mmol, 90 % yield) of product. IR (cm^{-1}): 1687 (m), 1674 (m), 1661 (w), 1264 (s) 1189 (w), 1090 (m), 1030 (w), 1004 (w), 843 (w), 824 (w), 807 (w), 754 (s), 725 (m), 610 (w), 584 (w), 477 (m), 458 (m).

Preparation of [2-19d][Cl]. [**2-19d**][Cl] was prepared by the same method as [**2-19b**][Cl], using 2,6-diamino-4-phenylphenol *bis*-hydrochloride (5.53 g, 20.3 mmol) and sulfur monochloride (15.2 g, 0.112 mol) in 150 mL of refluxing MeCN overnight. The blue/black precipitate was filtered off, washed thoroughly and dried in vacuo, yield 6.13 g (17.2 mmol, 85 % yield) of product, mp > 250 °C. IR (cm^{-1}): 1668 (s), 1401 (vs), 1271 (s), 1103 (w), 824 (w), 784 (w), 734 (m), 688 (w), 551 (w), 514 (w), 487 (m).

Preparation of [2-19e][Cl]. [**2-19e**][Cl] was synthesised by the same method as [**2-19b**][Cl], refluxing 4-methyl-2,6-diaminophenol *bis*-hydrochloride (4.22 g, 19.9 mmol) in 250 mL of dry MeCN with 16 mL S_2Cl_2 (~ 27.0 g, 200 mmol) for 12 h. The purple-brown precipitate was filtered off, washed thoroughly and dried *in vacuo*, yield 5.22 g (17.1 mmol, 89 % yield) of product, mp > 250 °C. IR (cm^{-1}): 1669 (s), 1406 (s), 1583 (s), 1090 (w), 1002 (m), 950 (w), 913 (w), 846 (m), 783 (w), 756 (s), 656 (w), 489 (m), 471 (w).

Preparation of [2-19f][Cl]. [**2-19f**][Cl] was synthesised by the same method as [**2-19b**][Cl], using the ammonium salt of *2,6-diamino-4-ethylphenol bis-hydrochloride* (3.00 g, 13.3 mmol) and S_2Cl_2 (10.1 g, 75.0 mmol) in 150 mL of refluxing MeCN overnight, yield 3.483 g (11.3 mmol, 84.5 % yield), mp > 250 °C. IR (cm^{-1}): 1667 (s), 1425 (vs), 1280 (s), 1246 (m), 1040 (m), 844 (m), 801 (w), 639 (w), 519 (w), 487 (m).

2.6.4 Preparation of Soluble Semiquinone-bridged *bis*-DTA Salts [2-19][X]

Preparation of [2-19b][OTf]: Silver triflate (3.42 g, 13.3 mmol) was added to a slurry of crude [**2-19b**][Cl] (3.82 g, 12.1 mmol) in 150 mL MeCN. The resulting deep purple solution was gently heated for 1 hr, then filtered to remove AgCl, and the filtrate flash-distilled to leave crude [**2-19b**][OTf] as a dark purple solid. The product was crystallized from hot MeCN to afford metallic green needles (3.07 g, 7.15 mmol, 59 % yield), mp > 250 °C. Anal. Calcd. for $C_7ClF_3N_2O_4S_5$: C, 19.60; N, 6.53.

Found: C, 19.86; N, 6.61. IR (cm^{-1}): 1683 (s), 4180 (s), 1442 (s), 1412 (m), 1283 (m), 1267 (s), 1264 (s), 1248 (s), 1224 (s), 1175 (s), 1167 (s), 1102 (m), 1028 (s), 857 (w), 839 (m), 785 (m), 758 (w), 640 (m), 635 (m), 576 (w), 517 (m), 486 (w), 472 (w). UV-Vis: λ_{max} = 572 nm, $\varepsilon = 1.59 \times 10^4$ $L \cdot mol^{-1} \cdot cm^{-1}$.

Preparation of [2-19c][OTf]: [**2-19c**][OTf] was prepared by similar method as [**2-19b**][OTf]. To a suspension of [**2-19c**][Cl] (3.63 g, 10.1 mmol) in 150 mL of MeCN was added AgOTf (3.03 g, 11.8 mmol) to give a deep purple solution. The solution was gently heated for 1 h, hot filtered and the solvent removed by flash distillation to give a green-black solid (5.12 g, 10.8 mmol). The solid was repeatedly crystallized from hot MeCN to give metallic green microcrystals (3.77 g, 7.96 mmol, 79 % yield). Anal. Calcd. for $C_7BrF_3N_2O_4S_5$: C, 17.76; N, 5.92. Found: C, 17.90; N, 5.77. IR (cm^{-1}): 1680 (s), 1247 (s), 1222 (s), 1160 (s), 1097 (m), 1024 (s), 855 (w), 817 (m), 783 (m), 760 (m), 634 (m), 592 (w), 575 (w), 516 (m), 485 (w), 464 (w).

Preparation of [2-19c][Br]: A solution of $^nBu_4NBr$ (1.96 g, 6.08 mmol) in 20 mL of MeCN was added dropwise to a solution of [**2-19c**][OTf] (2.41 g, 5.07 mmol) in 80 mL MeCN with stirring at room temperature. A dark purple precipitate was collected by filtration after 1 h, washed 3 x 20 mL MeCN and dried *in vacuo* to give 2.02 g (5.02 mmol, 99 % yield) of [**2-19c**][Br]. IR (cm^{-1}): 1674 (s), 1267 (s), 1167 (m), 1098 (m), 1024 (m), 800 (w), 764 (m), 633 (w), 457 (w).

Preparation of [2-19c][SbF$_6$]. [**2-19c**][SbF_6] was prepared by a similar method as [**2-19b**][OTf]. To a suspension of [**2-19c**][Br] (2.03 g, 5.02 mmol) in 100 mL of dry MeCN was added $AgSbF_6$ (2.02 g, 5.88 mmol) to give a deep purple solution. The solution was gently refluxed for 1 hour, hot filtered and the solvent removed by flashed distillation to give a dark purple solid (2.41 g, 4.31 mmol, 86 % yield). The solid was repeatedly recrystallized from hot EtCN to give metallic green needles (2.20 g, 3.93 mmol, 92 % recovery), mp > 250°C. Anal. Calcd. for $C_6BrF_6N_2OS_4Sb$: C, 12.87; N, 5.00. Found: C, 13.11; N, 4.67. IR (cm^{-1}): 2251 (w), 1671 (s), 1281 (s), 1270 (s), 1107 (m), 1025 (m), 857 (w), 841 (m),

874 (m), 654 (s), 559 (w), 490 (w). UV-Vis: λ_{max} = 572 nm, ε = 1.69 × 10^4 L·mol^{-1}·cm^{-1}.

Preparation of [2-19d][OTf]: [**2-19d**][OTf] was prepared the same way as [**2-19b**][OTf] by adding AgOTf (5.31 g, 20.7 mmol) to [**2-19d**][Cl] (6.13 g, 17.2 mmol) in warm MeCN (150 mL). After removal of the AgCl and solvent, the crude product was crystallized from hot acetonitrile to give purple shards (3.22 g, 6.8 mmol, 72 % yield), mp > 250 °C. Anal. Calcd. for $C_{13}H_5F_3N_2O_4S_5$: C, 33.19; H, 1.07; N, 5.95. Found: C, 33.02; H, 1.15; N, 5.80. IR (cm^{-1}): 1690 (s), 1414 (vs), 1243 (s), 1222 (m), 1095 (m), 1024 (s), 899 (w), 845 (w), 825 (w), 763 (s), 730 (w), 694 (w), 635 (s), 563 (w), 514 (m), 478 (w). UV-Vis: λ_{max} = 577 nm, ε = 1.50 × 10^4 L·mol^{-1}·cm^{-1}.

Preparation of [2-19e][OTf]: [**2-19e**][OTf] was prepared the same way as [**2-19b**][OTf] by adding AgOTf (2.89 g, 11.2 mmol) to [**2-19e**][Cl] (2.96 g, 10.0 mmol) in warm MeCN (150 mL). After remove the AgCl and solvent, the crude product (3.86 g) was crystallized from hot MeCN to give purple shards (2.51 g, 6.15 mmol, 61 % yield), mp > 250 °C. Anal. Calcd. for $C_8H_3F_3N_2O_4S_5$: C, 23.52; H, 0.74; N, 6.86. Found: C, 23.36; H, 0.91; N, 7.00. IR (cm^{-1}): 1683 (s), 1409 (s), 1288 (s), 1270 (s), 1238 (s), 1159 (s), 1030 (s), 1006 (m), 853 (w), 762 (s)660 (m), 638 (s), 660 (m), 938 (s), 573(w), 515 (m), 485 (m), 468 (m). UV-vis: λ_{max} = 568 nm, ε = 1.52 × 10^4 L$mol^{-1}cm^{-1}$.

2.6.5 Preparation of the Radicals (2-19)

Preparation of 2-19b · MeCN. *Method 1. Bulk Material for Conductivity and Magnetic Measurements.* A solution of [**2-19b**][OTf] (214 mg, 0.50 mmol) in 30 mL of degassed MeCN (3 freeze-pump-thaw cycles) was inverted onto a solution of dimethylferrocene (163 mg, 0.50 mmol) in 100 mL of similarly degassed MeCN. After 30 m, the fine microcrystalline precipitate of **2-19** · MeCN

was filtered off, washed with 5 × 30 mL of MeCN and dried in vacuo. Yield 140 mg (0.44 mmol, 88%); mp > 250 °C. Anal. Calc. for $C_8H_3ClN_3OS_4$: C, 29.95; H, 0.94; N, 13.10. Found: C, 29.98; H, 1.02; N, 13.30. IR (cm^{-1}): 2246 (w, ν(CN), 1603 (s, br, ν(CO)), 1366 (w), 1311 (m, br), 1117 (m), 997 (m), 952 (m, br), 902 (w), 807 (w), 710 (s), 589 (w), 502 (m), 467 (w), 452 (m). *Method 2. Slow Diffusion for Single Crystals.* A solution [**2-19b**][SbF_6] (100 mg, 0.194 mmol) in 15 mL degassed (4 freeze-pump-thaw cycles) MeCN was allowed to diffuse slowly into a similarly degassed solution of dimethylferrocene (200 mg, 0.932 mmol) in 15 mL MeCN. After 15 h purple needles of **2-19b** · MeCN suitable for crystallographic work were collected, washed with MeCN, and dried under a stream of nitrogen.

Preparation of 2-19b. *Method 1. Bulk Material for Conductivity and Magnetic Measurements.* A solution of [**2-19b**][OTf] (0.313 g, 0.730 mmol) in 30 mL of degassed EtCN (3 freeze-pump-thaw cycles) was inverted onto solution of octamethylferrocene (316 mg, 1.09 mmol) in 100 mL of similarly degassed EtCN to yield a green solution with crystalline precipitate. After 2 h of stirring at room temperature, the purple microcrystalline product was filtered off, washed with EtCN and dried under vacuum, (0.174 g, 0.621 mmol, 85 % yield), mp > 250°C. Anal. Calcd. for $C_6ClN_2OS_4$: C, 25.76; N, 10.01. Found: C, 26.00; N, 9.81. IR (cm^{-1}): 1615 (s), 1115 (m), 994 (s), 905 (m), 831 (m), 811 (m), 734 (s), 604 (w), 584 (w), 499 (m), 465 (m), 445 (m). *Method 2. Slow Diffusion for Single Crystals.* A solution of [**2-19b**][SbF_6] (75 mg, 0.145 mmol) in 15 mL degassed (4 freeze-pump-thaw cycles) MeCN was allowed to diffuse slowly into a similarly degassed solution of octamethylferrocene (100 mg, 0.346 mmol) over a 6 h period, affording **2-19b** (20 mg, 0.071 mmol, 49 % yield) as very fine, hair-like needles.

Preparation of 2-19c·MeCN. The **2-19c**·MeCN radical was prepared in the same way as **2-19b**·MeCN by allowing a degassed EtCN solution (15 mL) of [**2-19c**][OTf] (75 mg, 0.16 mmol) to diffuse into a degassed EtCN solution (10 mL) of octamethylferrocene (26 mg, 0.24 mmol) over a 5 h period, yielding the radical (26 mg, 0.071 mmol, 44 % yield) as lustrous black needles. IR (cm^{-1}): 2246 (w), 1603 (s, br), 1301 (s), 1113 (m), 957 (m, br), 875 (m), 792 (w), 701 (s), 583 (w), 494 (w), 449 (m).

Preparation of 2-19c. The **2-19c** radical was prepared using the same methodology as the bulk reduction of **2-19b**, by allowing the degassed EtCN solution (25 mL) of [**2-19b**][SbF_6] (100 mg, 0.18 mmol) to filter onto octamethylferrocene (80 mg, 0.27 mmol). After 2 h of stirring at room temperature, the purple microcrystalline radical was filtered off, washed with EtCN and dried under vacuum, (43 mg, 0.13 mmol, 74% yield). Anal. Calcd. for $C_6BrN_2OS_4$: C, 22.23; N, 8.64. Found: C, 22.44; H, 0.60; N, 8.27. IR (cm^{-1}): 1621 (s, br), 1532 (m), 1307 (m), 1258 (m), 1108 (s), 981 (m), 879 (w), 830 (w), 796 (m), 732 (s), 722 (s), 709 (s), 583 (w), 492 (m), 471 (m), 447 (m).

Preparation of 2-19d. A solution of [**2-19d**][OTf] (0.100 g, 0.212 mmol) in 15 mL of degassed (4 freeze-pump-thaw cycles) was allowed to diffuse over a period of 15 h into a solution of octamethylferrocene (0.076 g, 0.27 mmol) in 10 mL of equally degassed MeCN. The lustrous black, needle-shaped crystals of **2-19d** were collected, washed with MeCN and dried under a flow of nitrogen. Yield 60 mg (0.19 mmol, 88 %); dec 190°C. Anal. Calcd. for $C_{12}H_5N_2OS_4$: C, 44.84; H, 1.57; N, 8.71. Found: C, 44.62; H, 1.76; N, 8.46. IR (cm^{-1}): 1608 (s), 1312 (m), 1176 (m), 1070 (w), 1033 (w), 975 (w), 834 (w), 738 (s), 721 (s), 693 (m), 651 (m), 488 (m), 450 (m).

Preparation of 2-19e. *Method 1. Bulk Material for Conductivity and Magnetic Measurements.* A solution of [**2-19e**][OTf] (250 mg, 0.613 mmol) in 75 mL of degassed MeCN (3 freeze-pump-thaw cycles) was filtered onto a solution of decamethylferrocene (210 mg, 0.944 mmol) in 175 mL of similarly degassed MeCN to yield a blue solution with crystalline precipitate. After 1 h of stirring at

room temperature, the purple microcrystalline product was filtered off, washed with MeCN and dried under vacuum, (69 mg, 0.266 mmol, 43 % yield), mp > 250 °C. Anal. Calcd. for $C_7H_3N_2OS_4$: C, 32.41; H, 1.17; N, 10.80. Found: C, 32.46; H, 1.17; N, 10.96. IR (cm^{-1}): 1575 (s, br), 1456 (s), 1377 (s), 1285 (s, br), 1134 (w), 1029 (w), 1066 (w), 825 (w), 768 (w), 727 (m), 681 (m), 634 (m), 503 (w), 471 (w), 438 (w). *Method 2. Slow Diffusion for Single Crystals.* A solution of [**2-19e**][OTf] (75 mg, 0.184 mmol) in 15 mL degassed (4 freeze-pump-thaw cycles) MeCN was allowed to diffuse slowly into a similarly degassed solution of octamethylferrocene (64 mg, 0.221 mmol) over a 6 h period, affording **2-19e** as microcrystalline solid with few single crystal, which was isolated for single crystallography.

Chapter 3

Crystallography

3.1 Introduction

The synthesis and spectroscopic characterization of a new family of semiquinone-bridged *bis*-dithiazolyls (RBBO) were described in Chapter 2. The present Chapter provides the details of the solid state structural characterization of these radicals, and includes results of crystallographic data obtained by either single crystal or powder X-ray diffraction (XRD) methods. In addition, and in order to assess the structural effects of changes in oxidation state on internal bond metrics, the structures of a pair of oxidized salts were also obtained. The results obtained from these structural investigations are central to the understanding of the transport and magnetic properties of the radicals.

As will become apparent, all the radicals **3-1** to **3-4** possess essentially the same planar molecular framework, but adopt markedly different packing patterns. In the solid state, the length of the C=O linkage in both the cations and the radicals suggests a double bond character, which is consistent with the IR evidence (e.g. ν (CO) > 1650 cm^{-1}). Indeed the C=O distance in all the radicals (*ca.* ~ 1.20 Å) is significantly shorter than in the zwitterions **3-5** (1.277(3) Å and 1.265(3) Å),[1] and comparable to those found in the radical **3-6** (1.213(4) Å and 1.205(4) Å).[2]

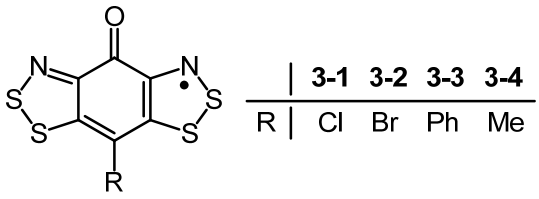

	3-1	3-2	3-3	3-4
R	Cl	Br	Ph	Me

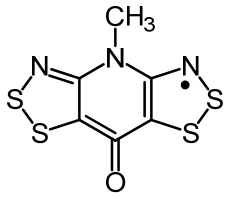

3-5

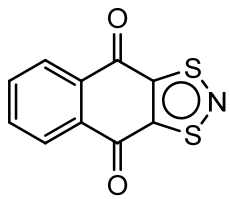

3-6

3.2 Crystal Structures of Cations

Crystals of [**3-1**][SbF_6]·MeCN and [**3-2**][OTf] suitable for single crystal X-ray diffraction were obtained by slow cooling of hot saturated MeCN solutions to -15 °C. Crystallographic data for [**3-1**][SbF_6]·MeCN and [**3-2**][OTf] are summarized in Table 3.1 and the selected bond lengths and angles are given in Table 3.2.

Table 3.1. Crystallographic parameters for cations.

Compound	[**3-1**][SbF_6]·MeCN	[**3-3**][OTf]
Formula	$C_8H_3ClF_6N_3OS_4Sb$	$C_{13}H_5F_3N_2O_4S_5$
M (g mol^{-1})	556.57	470.49
Temp (K)	296(2)	296(2)
λ (Å)	0.71073	0.71073
Space group	*Pbca*	$P2_1/c$
a (Å)	14.3729(7)	8.4534(4)
b (Å)	14.3342(7)	12.9782(6)
c (Å)	16.5005(8)	16.2121(7)
β (deg)	90	102.7620(10)
V (Å^3)	3399.5(3)	1734.69(14)
Z	8	4
ρ (calcd) (g cm^{-3})	2.179	1.802
μ (mm^{-1})	2.335	0.723
Data / restr. / parameters	4096 / 30 / 267	4183 / 0 / 300
R, R_w [I > 2σ(I)]	0.0458, 0.0803	0.0366, 0.0721

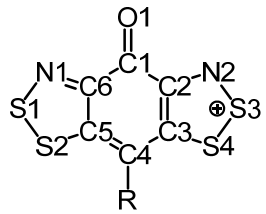

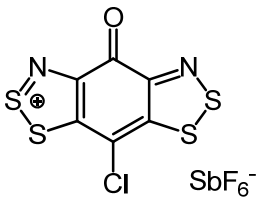

[3-1][SbF_6]

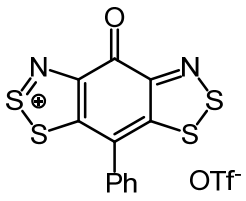

[3-3][OTf]

Table 3.2. Selected bond length (Å) and angles (º) of the cations.

	[**3-1**][SbF_6]·MeCN	[**3-3**][OTf]
S(1)-N(1)	1.595(3)	1.601(2)
S(1)-S(2)	2.0608(15)	2.0533(8)
S(3)-N(2)	1.591(4)	1.6101(19)
S(3)-S(4)	2.0632(16)	2.0695(8)
O(1)-C(1)	1.217(4)	1.204(2)
N(1)-S(1)-S(2)	98.66(13)	98.35(7)
C(5)-S(2)-S(1)	92.04(13)	92.54(6)
N(2)-S(3)-S(4)	98.68(14)	98.44(7)
C(3)-S(4)-S(3)	91.98(14)	92.32(7)
C(6)-N(1)-S(1)	116.7(3)	116.66(15)
C(2)-N(2)-S(3)	116.6(3)	116.36(14)

3.2.1 Structure of [3-1][SbF_6]·MeCN

[**3-1**][SbF_6]·MeCN crystallizes in an orthorhombic space group *Pbca*; in the unit cell all the cations and anions occupy the general positions with multiplicity $Z = 8$. The IR spectrum of this material indicated it was solvated, and consistent with this observation eight molecules of MeCN (one per cation) were found in the unit cell. The packing of the cations, anions and solvent molecules is illustrated in Figure 3.1; there was a small degree of rotational disorder of the F atoms of the anions, which has been removed for clarity. The cations are laced together with a series of intermolecular S···O′ contacts (d_1 = 2.791 Å and d_2 = 2.891 Å) and S···N′ contacts (d_3 = 2.948 Å and d_4 = 2.972 Å) with the solvent molecules.

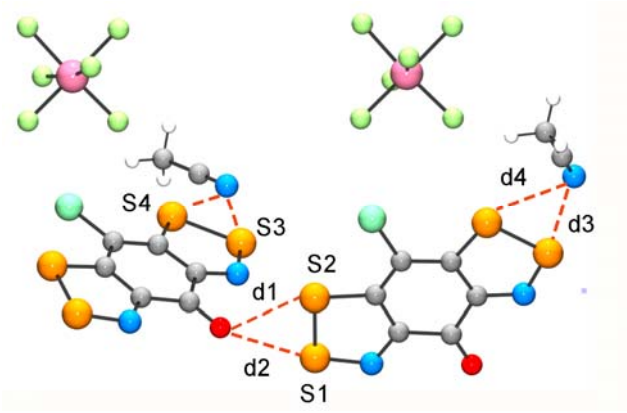

Figure 3.1. Packing of cations, anions and solvent molecules in [**3-1**][SbF_6]; intermolecular S···O′ and S···N′ contacts are shown with dashed lines.

3.2.2 Structure of [3-3][OTf]

[**3-3**][OTf] crystallizes in the monoclinic space group $P2_1/c$. The anion experiences rotational disorder and the cations form tilted stacks (as shown in Figure 3.2) with S···S′ and S···N′ interactions that are related by *c*-glides. Along the stacking axis (*b* axis) the cations are related by a 2_1 screw axis and the anions occupy the pockets between the cations. The mean plane through all atoms of cation, save the phenyl ring, is essentially planar, while the torsion angle between the mean planes of the backbone and the phenyl ring is 64.47°.

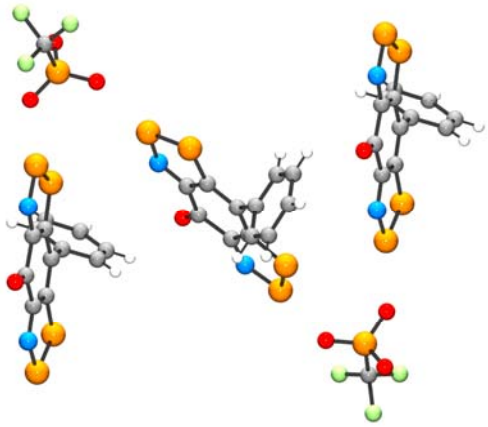

Figure 3.2. Packing of cations and anions in [**3-3**][OTf].

3.3 Crystal Structure of Radicals

The crystal structures of semiquinone-bridged radicals **3-1**, **3-3** and **3-4**, including the MeCN solvate of **3-1**, have been determined by single crystal X-ray diffraction. Because of the small size of the crystals of the unsolvated radical **3-1**, and the consequent paucity of reflections and relatively high R-values, we cross-checked the single crystal results by powder diffraction methods (see following section). At the same time this analysis confirmed the phase uniformity of the bulk material. The structural information for **3-4** originates from a single crystal gleaned from a co-diffusion reduction. As in the case of **3-1** the structure and phase purity of the bulk material was confirmed by powder diffraction analysis. Table 3.3 lists crystal data from single crystal work, and Figure 3.3 illustrates ORTEP drawings of the asymmetric units, and also provides the atom numbering schemes; selected intramolecular metrics are provided in Table 3.4. As may be seen in the table there are small increases in the S-S, S-N and S-C distances in the radical relative to those in the cations of **3-1** and **3-3** that can be related to the addition of an electron to an antibonding orbital.

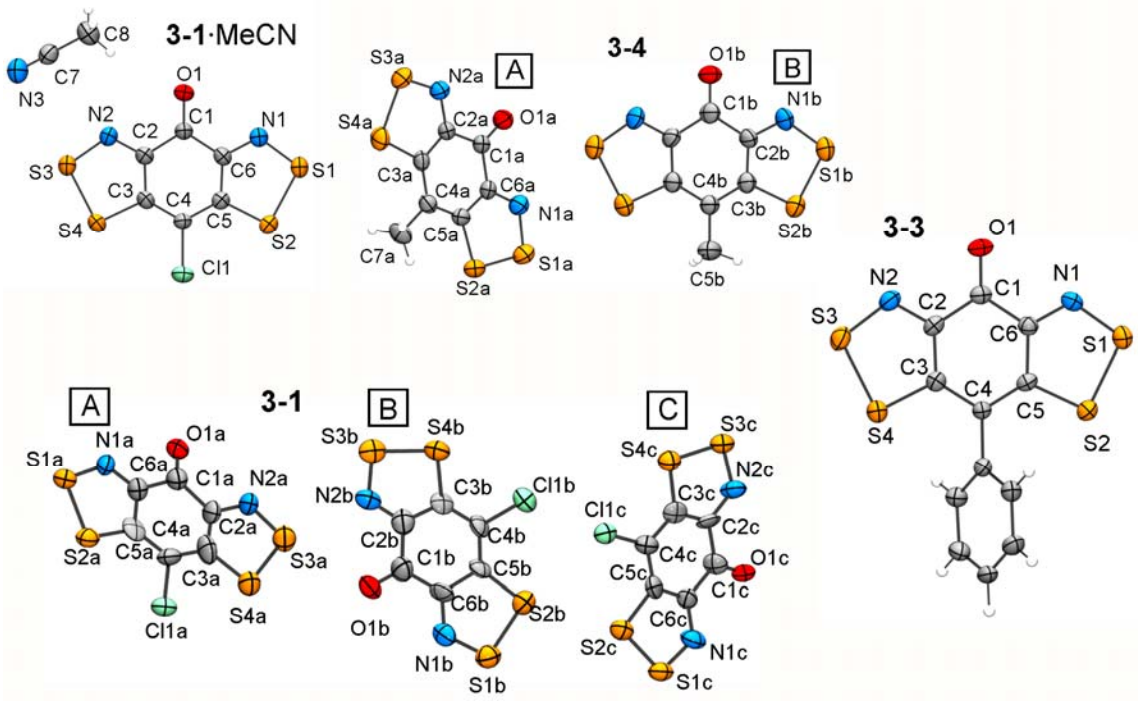

Figure 3.3. ORTEP drawings (50% probability ellipsoids) of the asymmetric units of **3-1**, **3-1**·MeCN, **3-3** and **3-4**, showing atom numbering scheme.

Table 3.3. Single crystal data for radicals.

Compound	**3-1**·MeCN	**3-1**	**3-3**	**3-4**
Formula	$C_8H_3ClN_3OS_4$	$C_6ClN_3OS_4$	$C_{12}H_5N_3OS_4$	$C_{10.5}H_{4.5}N_3O_{1.5}S_6$
M (g mol^{-1})	320.82	279.77	321.42	388.28
Temp (K)	300(2)	100(2)	296(2)	296(2)
λ (Å)	1.54178	1.54178	0.71073	0.71073
Space group	$Pna2_1$	$Pna2_1$	$P2_12_12_1$	$C2/c$
a (Å)	9.4913(3)	48.779(3)	6.8011(7)	25.828(3)
b (Å)	23.5986(8)	3.8228(2)	11.3785(12)	14.5799(14)
c (Å)	5.3124(2)	14.2036(9)	15.6252(16)	7.3586(7)
β (deg)	90	90	90	95.687(2)
V (Å^3)	1189.88(7)	2648.6(3)	1209.2(2)	2757.4(5)
Z	4	12	4	8
ρ (calc.) g cm^{-3}	1.791	2.105	1.766	1.871
μ (mm^{-1})	9.300	12.373	0.774	0.993
Data / restr. / par.	1770 / 1 / 155	2785/520/380	3431 / 0 / 174	4020 / 0 / 192
R [I > 2 σ(I)]	0.0216	0.0808	0.0547	0.0582
R_w [I > 2 σ(I)]	0.0561	0.2027	0.0739	0.0774

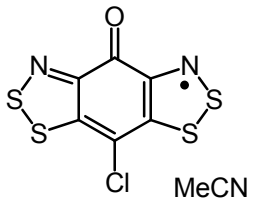

3-1• MeCN

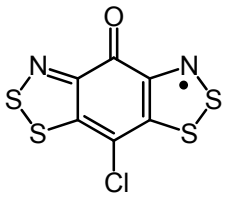

3-1

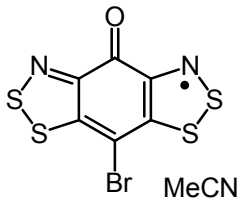

3-2• MeCN

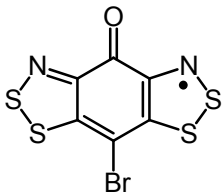

3-2

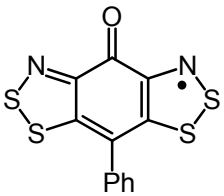

3-3

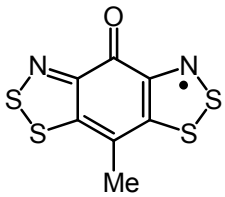

3-4

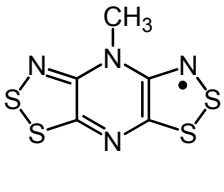

3-7

Table 3.4. Selected bond length (Å) and angles (º) in the radicals.

	3-1·MeCN	**3-1**		
		Molecule A	Molecule B	Molecule C
S(1)-N(1)	1.6236(19)	1.600(15)	1.600(16)	1.575(15)
S(1)-S(2)	2.0958(9)	2.103(6)	2.104(6)	2.102(6)
S(3)-N(2)	1.625(2)	1.582(15)	1.576(16)	1.624(15)
S(3)-S(4)	2.0913(10)	2.092(7)	2.100(8)	2.131(7)
O(1)-C(1)	1.216(3)	1.19(2)	1.22(2)	1.221(18)
N(1)-S(1)-S(2)	98.43(7)	98.1(6)	98.7(6)	100.3(6)
C(5)-S(2)-S(1)	91.15(8)	90.4(8)	91.6(6)	89.8(7)
N(2)-S(3)-S(4)	98.09(8)	98.5(6)	99.4(6)	98.3(6)
C(3)-S(4)-S(3)	91.43(8)	90.6(8)	91.6(6)	90.1(6)
C(6)-N(1)-S(1)	115.67(17)	117.8(14)	115.4(13)	115.4(12)
C(2)-N(2)-S(3)	116.43(16)	116.1(14)	118.6(14)	114.8(11)

Table 3.4. (continued) Selected bond length and angles of the radicals.

	3-2·MeCN	**3-3**	**3-4**	
			Molecule A	Molecule B
S(1)-N(1)	1.626(20)	1.634(3)	1.621(3)	1.620(3)
S(1)-S(2)	2.0926(9)	2.1046(12)	2.0762(16)	2.0931(15)
S(3)-N(2)	1.6255(2)	1.614(3)	1.619(3)	-----
S(3)-S(4)	2.096(23)	2.0847(13)	2.0991(15)	-----
O(1)-C(1)	1.216(16)	1.225(4)	1.222(4)	1.234(6)
N(1)-S(1)-S(2)	98.040(3)	99.18(11)	98.79(12)	98.06(12)
C(5)-S(2)-S(1)	91.49(2)	91.07(12)	92.23(13)	91.89(13)
N(2)-S(3)-S(4)	98.483(9)	98.68(11)	98.41(12)	-----
C(3)-S(4)-S(3)	91.15(30)	91.84(11)	91.26(13)	-----
C(6)-N(1)-S(1)	116.556(7)	114.5(2)	115.5(3)	116.7(3)
C(2)-N(2)-S(3)	115.554(5)	116.3(2)	115.8(3)	-----

3.3.1 Structure of 3-1·MeCN

The solvated **3-1**·MeCN radical crystallizes in the non-centrosymmetric orthorhombic space group $Pna2_1$ with $Z = 4$. In the unit cell, a series of intermolecular S···O′ (d_1 = 2.862 Å and d_2 = 2.786 Å) and S···N′ (3.291 Å) interactions laces the radicals into two sets of almost perpendicular (82.37°) ribbons (Figure 3.4) which are related by an *a*-glide plane. This produces a zig-zag arrangement of radicals along the ribbons, within the folds of which the acetonitrile solvate molecules are perfectly sequestered; these are locked in place by a series of short polar MeCN···S′ and MeC(N)···N′ interactions. There are no intermolecular contacts within the sum of the van der Waals radii[3] between radicals in neighboring π-stacks along the *b* axis, although there is one interaction (S1···S2′ = 3.750 Å) which may provide some electronic communication. These ribbons are packed in a superimposed slipped π-stack motif along the *c*-axis shown in Figure 3.5.

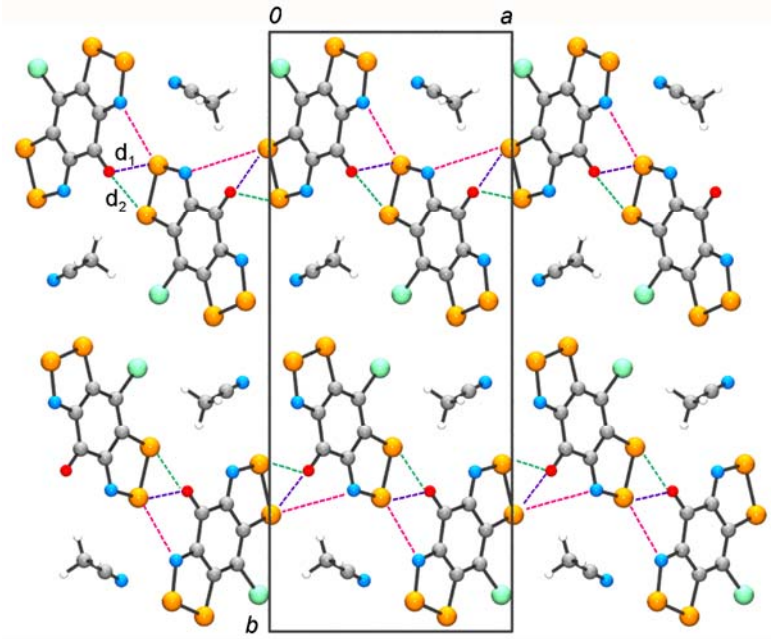

Figure 3.4. Unit cell of **3-1**·MeCN, viewed long the *c* axis, with intermolecular S···O′ and S···N′ contacts shown with dashed lines.

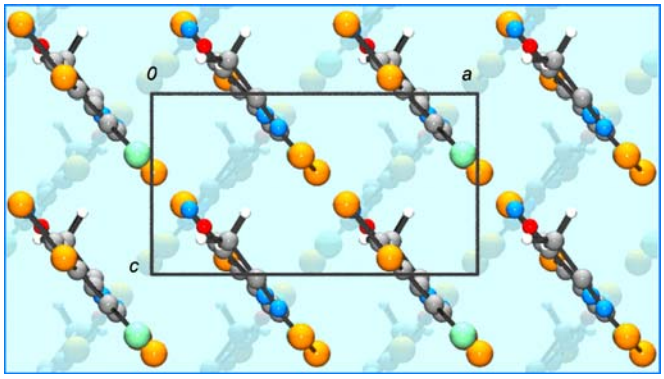

Figure 3.5. Unit cell of **3-1**·MeCN, viewed along *b* axis.

Inspection of the ribbon-like layers within the π-stacks of **3-1**·MeCN reveals some interesting features which may be compared to the herringbone structures observed for pyridine-bridged radicals. The mean planes (through all atoms) of the radicals along the π-stacks of **3-1** are separated by a distance δ = 3.497 Å, which is greater than the sum of the standard van der Waals radii of all atoms.[3] In contrast to the herringbone architecture found in pyridine-bridged systems, there is also a π-type overlap between radicals in neighboring stacks of **3-1**·MeCN, as illustrated in Figure 3.6 which benefits the transport properties. The electronic consequences of this are developed in Chapter 4.

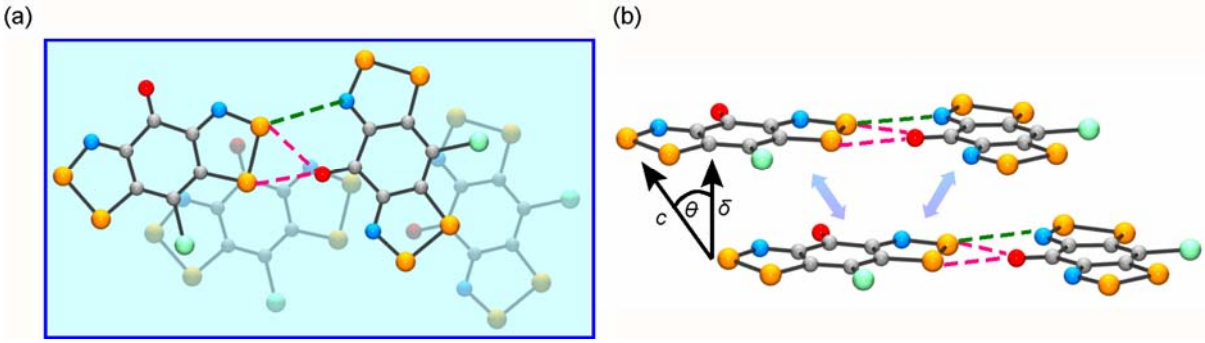

Figure 3.6. Slipped π-stacks of radicals in **3-1**·MeCN, viewed (a) perpendicular to the molecular planes and (b) from the side.

3.3.2 Structure of 3-1

Like the acetonitrile adduct **3-1**·MeCN, crystals of the unsolvated radical **3-1** (grown from propionitrile), belong to the polar orthorhombic space group $Pna2_1$. The crystal architectures of the two variants, however, are profoundly different. With 12 molecules per unit cell, there are three independent molecules (**A**, **B** and **C**) in the asymmetric unit and Z = 4of **3-1** as shown in Figure 3.7, and each of these forms the basis for an evenly spaced, slipped π-stack array of radicals running along the *y* direction. Figure 3.7 provides a unit cell drawing which shows the packing of the radicals (columns) in the *xz* plane. Also indicated in this drawing is the labyrinth of lateral intermolecular S···S′, S···O′ and S···N′ contacts that stitch the radicals together and all the contacts are within the sum of respective van der Waals separations. The overall structural motif can be described in terms of wave-like arrays of **C**-radicals running along the *z*-direction, neighboring radicals being related by a 2_1 axes at x = 0, ½, and linked by 4-center $(S\cdots N')_2$ bridges. The **B**-radicals also form wave-like arrays along the *z*-direction, but nearest neighbors are now related by the *n*-glides at x = ¼ and ¾, and are linked by S···O′ and S···N′ contacts. Finally, the **A**-radicals serve as bridges between these two chains, interacting strongly with each.

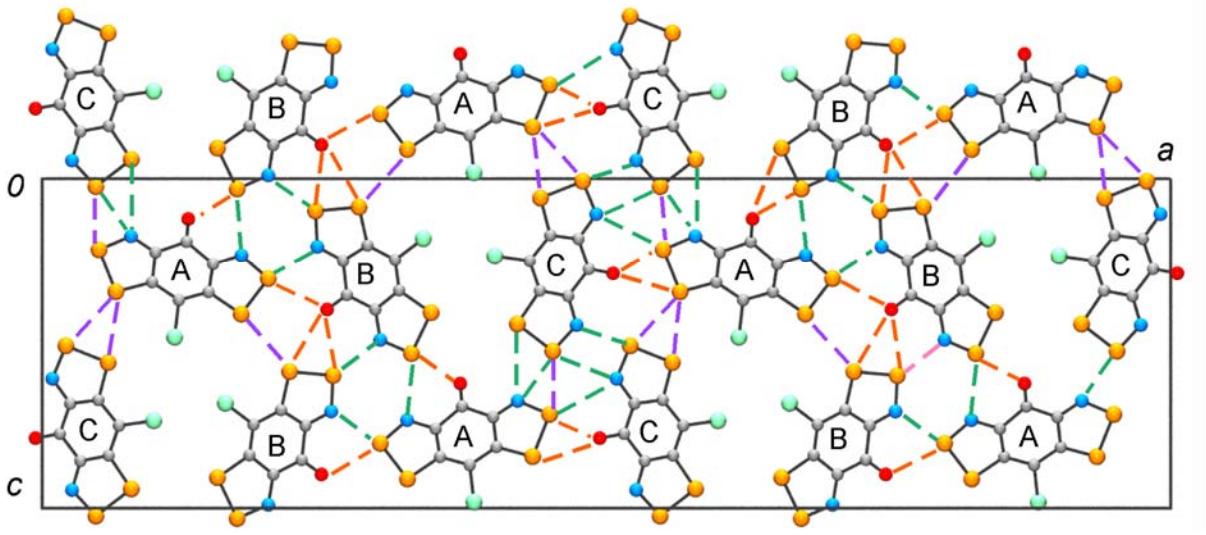

Figure 3.7. Packing of A, B and C radicals in the *xz* plane of the unit cell of **3-1** (unsolvated), showing lateral intermolecular S···S′ (green), S···O′ (orange) and S···N′ (purple) contacts.

Despite the rather oblique alignment of the slipped π-stacks, when viewed parallel to the *z* direction (Figure 3.8), it is apparent that the individual columns share common features. First, in all the three π-stacks the interplanar separation δ is closer than that formed in **3-1**·MeCN and near that observed in graphite.[4] Second, slippage of the radicals occurs almost exclusively by a longitudinal movement of neighboring radicals, as indicated by the value of *dy* in Table 3.5; the small value of *dx* coupled with the almost equal intermolecular S1···S2′ and S3···S4′ interactions indicates virtually no lateral slippage. Staggering of this type and to this degree has been seen before in π-stacked radicals of pyridine-bridged systems,[5] and is associated with weak overlap and antiferromagnetic exchange interactions.

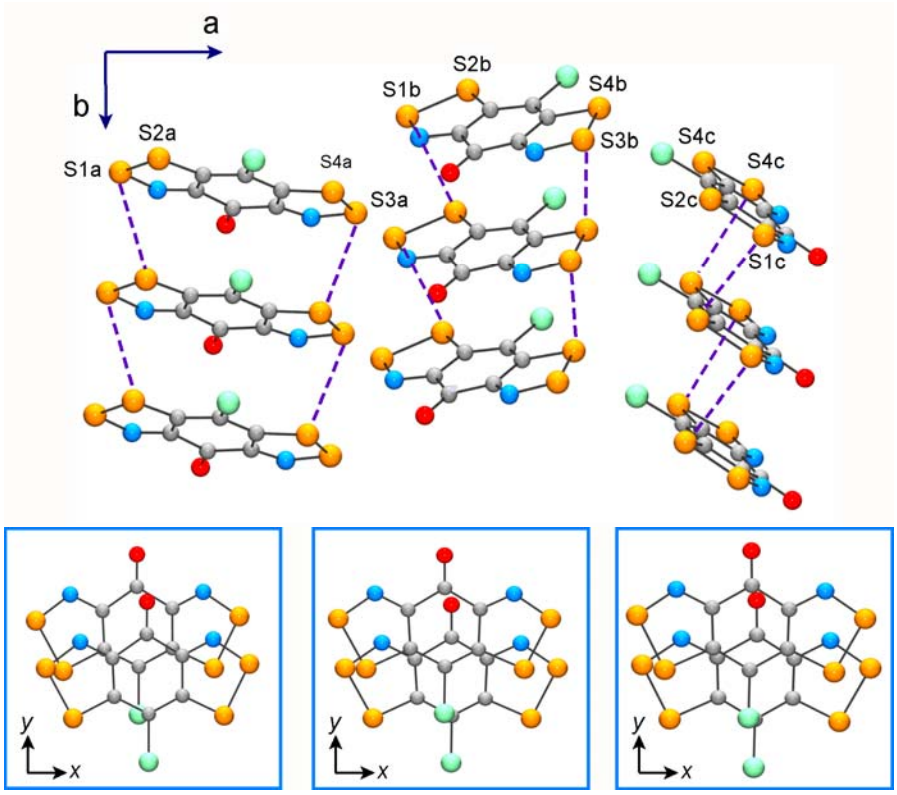

Figure 3.8. Slipped π-stacking of three symmetry independent radicals **A**, **B** and **C** in **3-1**. Staggering of radicals affords close intracolumnar S1···S2′ and S3···S4′ interactions. The views below illustrate the slippage of adjacent radicals along the local directions *x* and *y*.

Table 3.5. Structural Parameters [a] of π-Stacks in **3-1**.

	Radical **A**	Radical **B**	Radical **C**
S1···S2′	3.633	3.453	3.545
S3···S4′	3.574	3.625	3.575
δ [b]	3.374	3.359	3.368
dx [c]	0.300	0.249	0.231
dy [d]	1.771	1.808	1.792

[a] Distances in Å. [b] Interplanar separation along π-stacks. [c] Lateral slippage of neighbors along π-stacks. [d] Longitudinal slippage of neighbors along π-stacks.

3.3.3 Structure of 3-3

In the solid state **3-3** crystallizes in the non-centric space group $P2_12_12_1$. The intermolecular S···O′ contacts (2.828 Å) lace the radicals into sheets, as shown in Figure 3.9. These sheets are packed into an alternate ABABAB π-stack motif with the *a* axis as the stacking direction. Along the stack (*a* axis), the nearest radicals, which are related by the 2_1 screw axis, are separated by S1···S3′ interactions d_1 (3.680 Å) and d_2 (3.806 Å) which are longer than the sum of van der Waals radii of sulfur.[3] Moreover, the C=O bond length in the radical (1.225(4) Å) is elongated in comparison to the cation (1.204(2) Å).

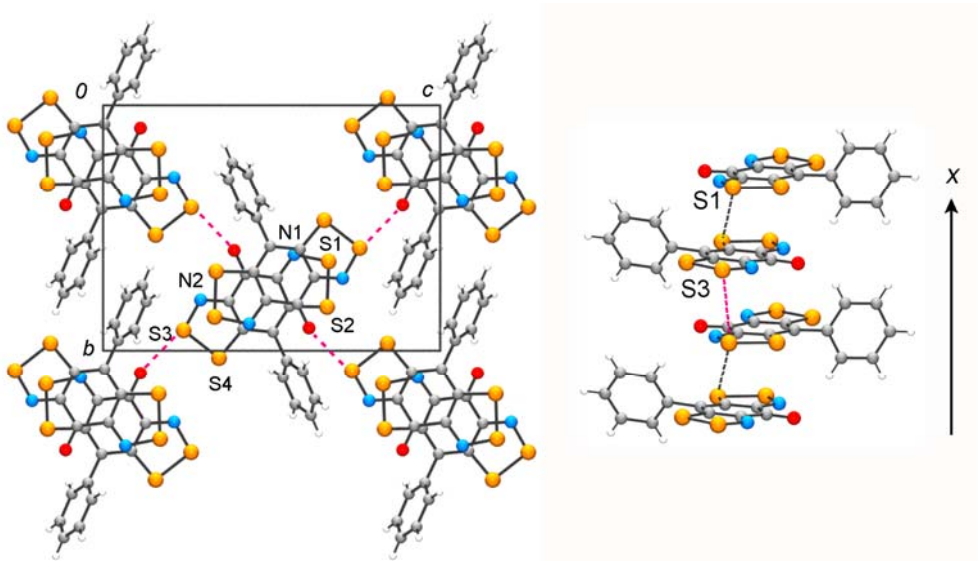

Figure 3.9. Unit cell of **3-3**, viewed perpendicular to the *yz* plane (left), with intermolecular S3···O′ contacts shown with dashed lines. The alternating ABABAB π-stacks, with intrastack S1···S3′ contacts d1 and d2 are shown on the right.

3.3.4 Structure of 3-4

The structural information for **3-4** originates from one of the single crystals gleaned from co-diffusion reductions, which structure and phase purity of the bulk material was confirmed by powder diffraction method (see section 3.4). Crystals of **3-4** belong to the monoclinic space group *C*2/*c*, with *Z* = 8. There are 1½ molecules in the asymmetric unit (as illustrated in Figure 3.3), with the **B** radicals occupying the Wyckoff position 4e, being bisected by the two-fold rotation axes at *x* = 0, ½; the **A** radicals are located in general positions. All of these molecules are laced together by a series of intermolecular S···O′, S···N′ and S···S′ contacts (d1 to d11) which are summarized in Table 3.6. The unit cell drawing shown in Figure 3.10 illustrates the packing of the radicals viewed parallel to the *c*-axis, and highlights the zig-zag ribbons of **A** molecules which are generated by the two-fold screw axes at *x* = ¼ and ¾. The **B** radicals at *x* = 0, ½ are located in the pockets formed by the out-of-register

ribbons, and locked in place by a complex network of intermolecular S···S′, S···O′ and S···N′ contacts d1-d5, all of which are within the respective van der Waals separation.

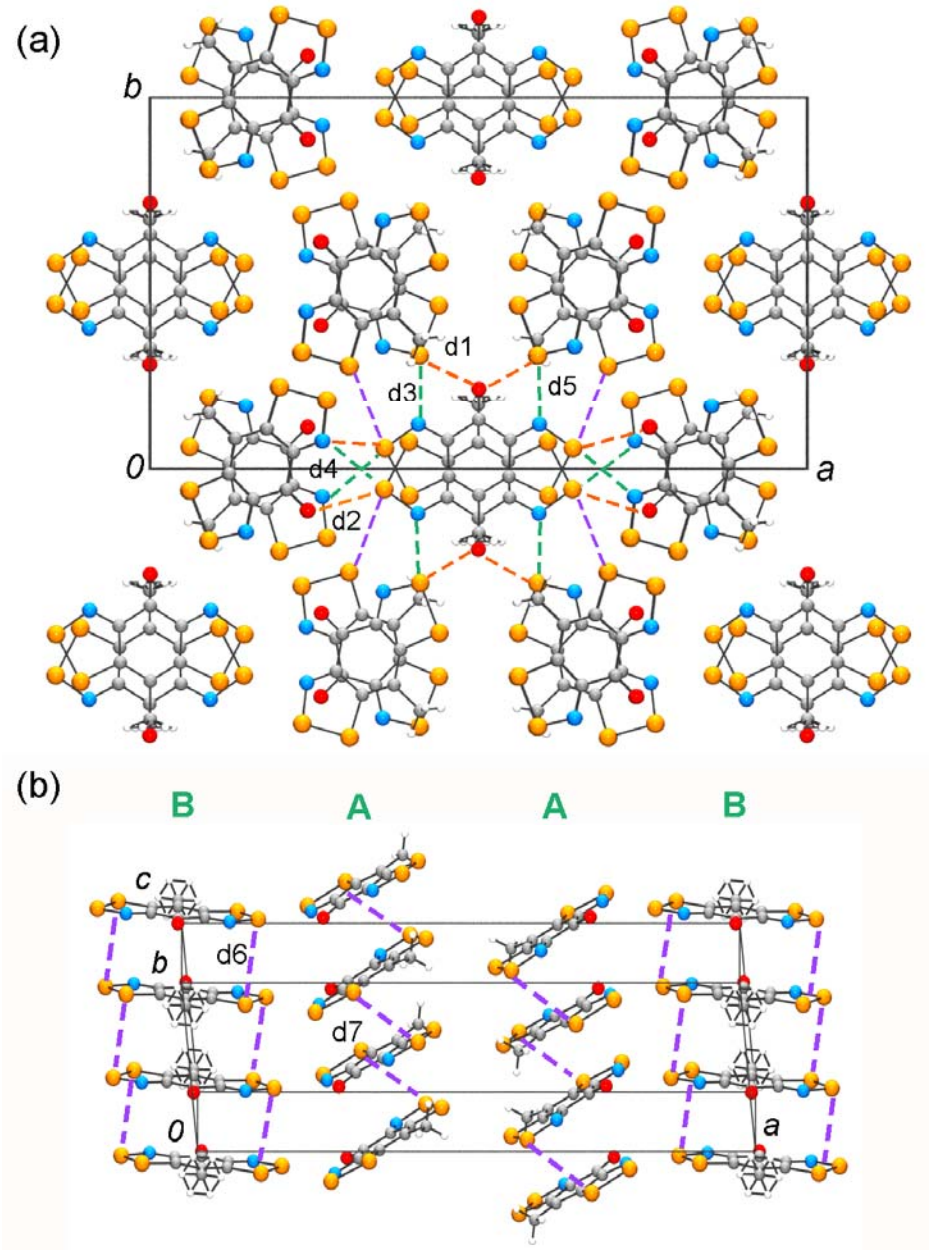

Figure 3.10. Packing of radicals in the unit cell of **3-4**, viewed parallel to the *c* axis in (a). Alternation of radicals along the **A** and **B** π-stacks is shown in (b). The **B** radicals lie on a two-fold rotation axis, and the methyl protons are disordered. Intermolecular S···S′ (purple), S···O′ (orange) and S···N′ (green) contacts shown with dashed lines.

Table 3.6. Intermolecular Contacts of **3-4** [a]

d1	S3a···O1b′	2.974
d2	O1a···S1b′	3.131
d3	S3a···N1b′	3.244
d4	N1a···S1b′	3.101
d5	S2a···S1b′	3.584
d6	S2b···S1b′	3.710
d7	S3a···S2a′	3.761
d8	O1a···S1a′	2.975
d9	O1a···S2a′	2.968
d10	N2a···S1a′	3.165
d11	S1a···S1a′	3.722

[a] Distances in Å; see Figure 3.10 and Figure 3.11 for definitions of d1-d11.

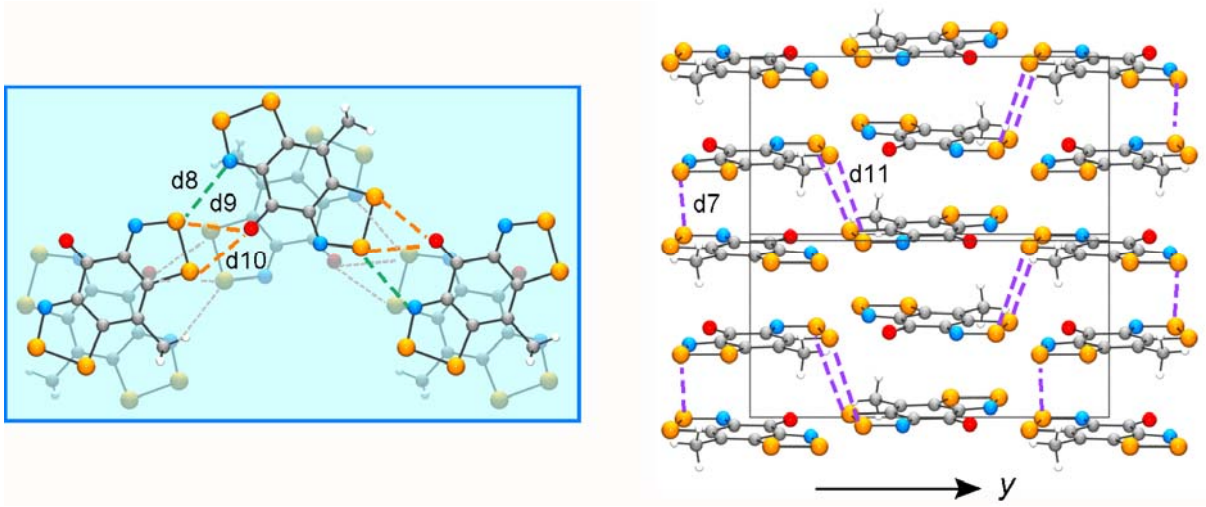

Figure 3.11. Ribbons of **A** radicals running parallel to *b* (left) and skewed π-stacking of **A** radicals (right); alternate layers are interconverted by a two-fold screw axis. Intermolecular S···S′ (purple), S···O′ (orange) and S···N′ (green) contacts are shown with dashed lines.

Both the **A** and **B** molecules form the basis for an alternating but evenly spaced π-stack, as illustrated in Figure 3.10. For the B-radicals, which lie on the two-fold rotation axes, the resulting head-over-tail overlay of neighboring radicals is centrosymmetric. By contrast, neighboring **A**-radicals along the π-stacks are related by two-fold screw axes, which produces a less superimposed overlay with consecutive radicals being rotated about the stacking c axis by angle of 89.8°. The stacks are also severely slipped, as a result of which there are no short intermolecular S···S′ contacts, the shortest approach being the rather oblique contact d7. The interplanar separation δ (3.413 Å) is, nonetheless, quite close. By contrast, δ = 3.627 Å in the more superimposed -radical π-stacks. The head-over tail arrangement found for the B-radicals is reminiscent of that found in **3-3** (Figure 3.12), while the twisted A-stacks are more nearly related to those seen in the pyrazine-bridge radical **3-7** (R = Me). It should be noted, however, that in **3-7** (R = Me) the mean planes of the radicals are (at room temperature) rigorously perpendicular to the stacking direction. The electronic consequences of these different stacking motifs is discussed below.

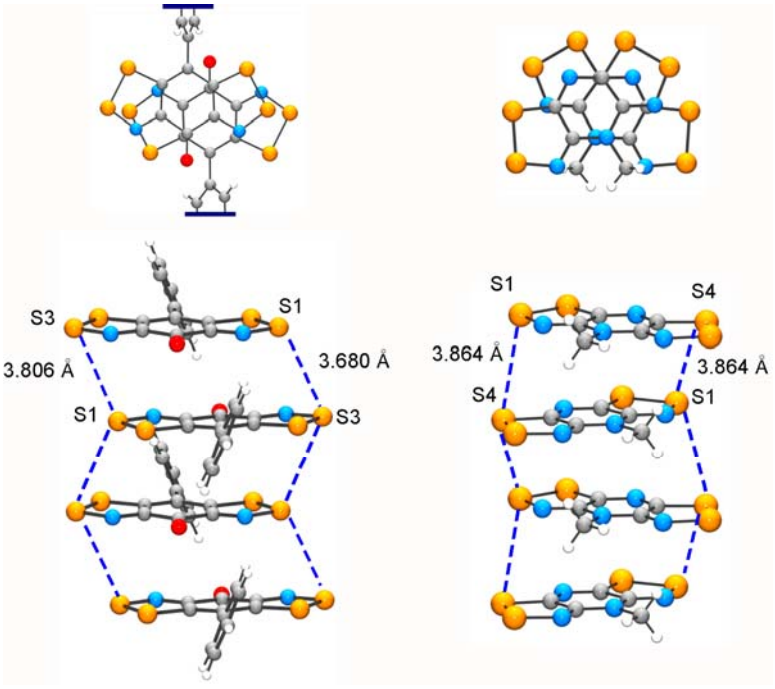

Figure 3.12. Alternating π-stacked architectures in **3-3** (left) and **3-8** (right), viewed from above and the side, with internolecular S···S′ shown with dashed lines.

3.4 Powder Crystallography

For some of the radicals whose crystals structures were determined by single crystal diffraction, powder diffraction analysis was also performed. In the case of radical **3-4**, the powdery appearance of the bulk material led to a concern that it might not be the same phase as the single crystals isolated for single crystal work. Indeed, the question arose as to whether the material might be amorphous. This, of course, would have serious consequences on the interpretation of the magnetic and conductive measurements, which were performed on the bulk material. A similar situation arose for **3-1**, which was invariably obtained as wispy needles. In addition, given the resulting poor resolution of the single crystal data, powder diffraction was undertaken to confirm the structural assignment. Figure 3.13 shows the observed and calculated powder patterns for these two materials.

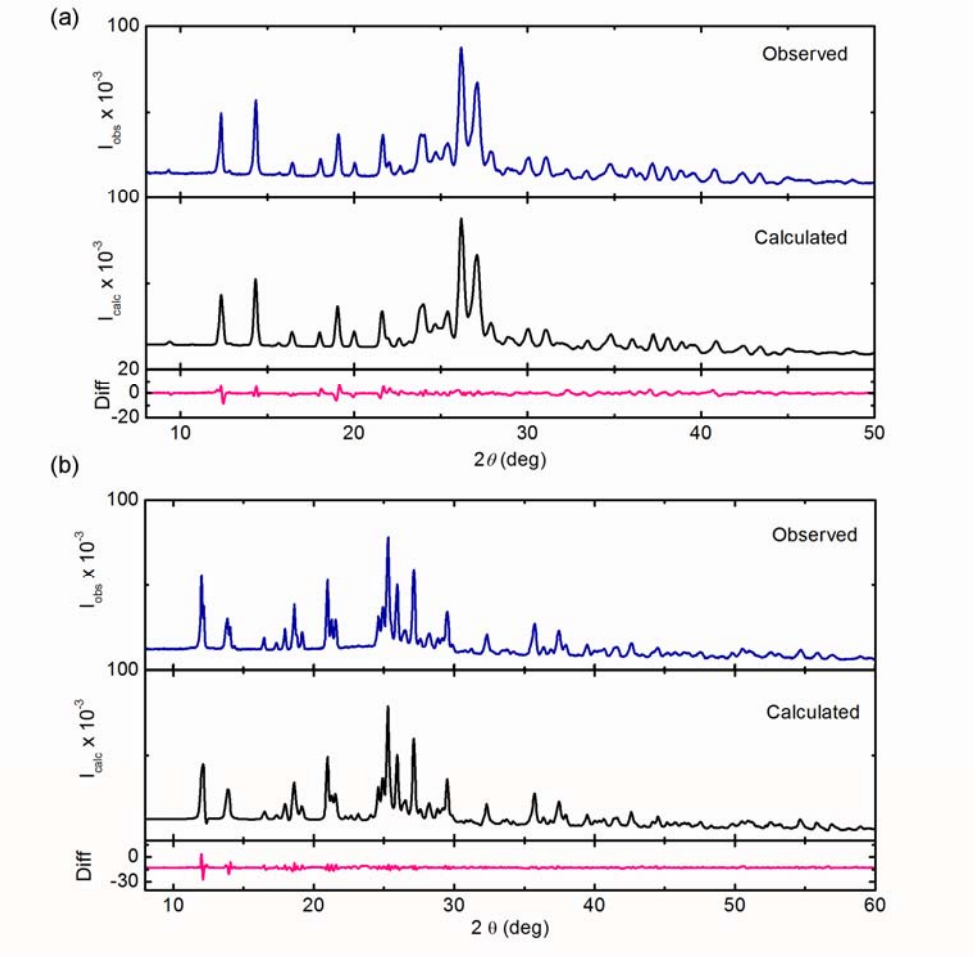

Figure 3.13. Observed and calculated powder X-ray diffraction pattern for (a) **3-1** and (b) **3-4**.

Powder diffraction methods were used to investigate the structure of **3-2**·MeCN, for which crystals suitable for single crystal work could not be obtained. The powder diffraction pattern obtained for this material was indexed in DASH, and the space group taken to be that previously found for **3-1**·MeCN. Subsequent modeling in DASH, using the coordinates of for **3-1**·MeCN as a starting point, and Rietveld refinement of the structure so obtained, gave the fit shown in Figure 3.14. As may be seen, there is no significant change in terms of the cell parameters; however the interplanar separation, δ, for **3-2**·MeCN (δ = 3.646 Å) is slightly larger than the **3-1**·MeCN (δ = 3.497 Å *vide supra*). This leads to a decreased overlap of the SOMO orbital which has a significant impact on the transport property (see Chapter 4).

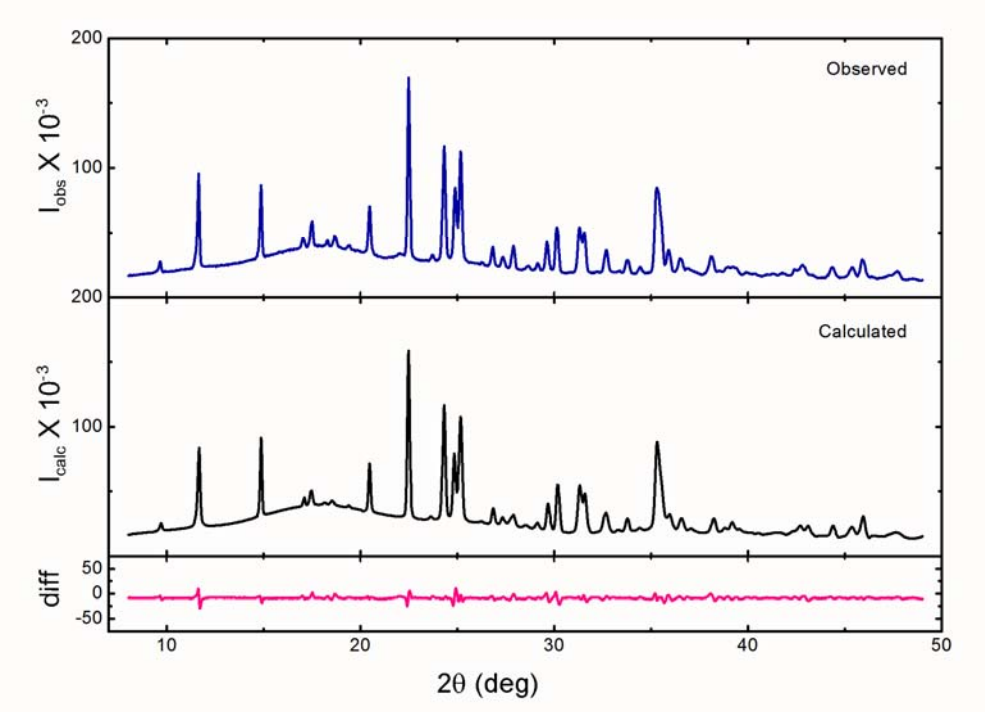

Figure 3.14. Observed and calculated powder X-ray diffraction pattern for **3-2**·MeCN.

3.5 Experimental

Single crystals were glued to glass fibers with epoxy. (i) X-ray data for [**3-1**][SbF_6]·MeCN, [**3-3**][OTf], **3-3** and **3-4** were collected using omega scans with a Bruker APEX I CCD detector on a D8 3-circle goniometer and Mo K_α (λ = 0.71073 Å) radiation. The data were scanned using Bruker′s SMART program and integrated using Bruker′s SAINT software.[6] The structures were solved by direct methods using SHELXS-90[7] and refined by least-squares methods on F^2 using SHELXL-97[8] incorporated in the SHELXTL[9] suite of programs. (ii) X-ray data for the radical **3-1**·MeCN and **3-5** were collected using omega scans with a Bruker Microstar Cu rotating anode (λ = 1.54178 Å) diffractometer equipped with a Proteum 135 CCD detector. The data were integrated with SAINT and scaled with X-SCALE which is part of the Bruker Proteum software package.[10] Structural solution and least square refinements were conducted using the Olex2 interface[11] to the SHELX suite. (iii) The X-ray data for the unsolvated radical **3-1** were also measured on a Bruker PROTEUM-135 CCD system equipped with a Cu MicroSTAR rotating anode (λ = 1.54178 Å). The frames were integrated with the Bruker SAINT software package and corrected for absorption effects using the multi-scan method SADABS. The structure was solved and refined using the Bruker SHELXTL Software Package. Given the small size of the crystal, and the resulting paucity of data, the final R (0.0808) and R_w (0.2027) are not unexpected. Confirmation of the solution obtained from single crystal work was provided by a powder diffraction analysis in which the experimentally observed powder pattern was matched by means of a Rietveld refinement (R_p = 0.44) of a model taken from the single crystal cell parameters and atomic coordinates.

Powder data was collected on a X-ray powder diffractometer with a position sensitive detector (INEL) at room temperature using Cu Kα radiation (λ = 1.5406 Å). The total 2θ range was 0-112°, measured in steps of 0.029°. Structures were solved using a single crystal structure model and the unit cell dimensions were refined by Rietveld methods[12] using the GSAS program package.

Chapter 4

Transport and Magnetic Properties

4.1 Introduction

In Chapter 3 the crystal structures of a new family of semiquinone-bridged *bis*-dithiazolyl radicals (**4-1**) were discussed in detail. In general there are three types of packing motif for these radicals, as illustrated in Figure 4.1. In this chapter, the correlation of the structure with the transport and magnetic properties will be discussed.

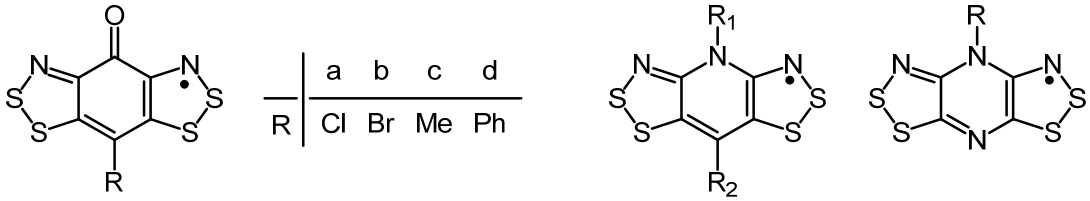

4-1 **4-2** **4-3**

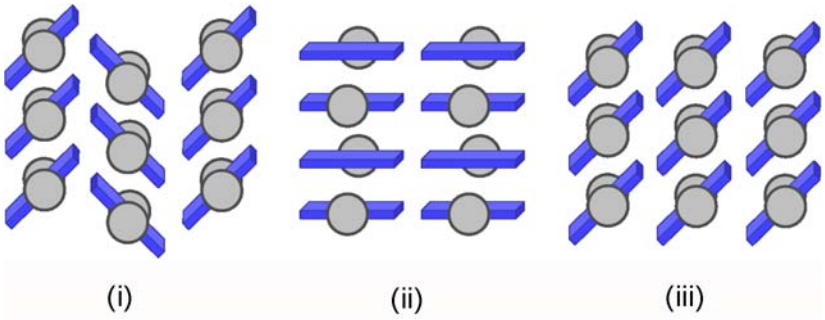

Figure 4.1. Three types of packing motifs: (i) herringbone π-stacks; (ii) alternating head-over-tail π-stacks; (iii) slipped ribbon π-stacks.

According to the literature, the pyridine-bridged *bis*-dithiazolyl radicals (**4-2**) typically adopt the herringbone packing motif (type i), which has good lateral overlap and relative high conductivity for molecular based radicals.[1] In the pyrazine-bridged *bis*-dithiazolyl radicals (**4-3**) type ii of packing was

observed, which gave larger conductivities due to better overlap. However, these radicals dimerized at low temperature.[2] In contrast, the semiquinone-bridged *bis*-dithiazolyl radicals (**4-1**) adopt a wide range of packing motifs (*i.e.,* type i, ii and iii). More interestingly the unique S···O′, S···N′ interactions provide better lateral overlap than pyridine-bridged *bis*-dithiazolyl radicals (**4-2**) and the alternating head-over-tail packing pattern (type ii) observed in **4-1c**, and **4-1d** do not dimerize, in contrast to the pyrazine systems (**4-3**). Both of these factors lead an increase in conductivity and interesting magnetic properties.

4.2 Band Structures

In order to explore and compare the electronic structures of the radicals **4-1,** a series of Extended Hückel Theory (EHT) band structure calculations have been carried out on the crystal structure geometries. The results must be viewed with caution, as the tight-binding approximation does not provide a proper description of the ground state of strongly correlated systems such as those reported here. The method nonetheless provides qualitative insight into the direction and extent of intermolecular orbital interactions within and between the radical π-stacks, and to this extent carries value. As in previous work, the focus was on the dispersion of the crystal orbitals (COs) arising from the interactions of the SOMOs along the π-stacking direction.[a] An idealized view of this antibonding SOMO is illustrated in Figure 4.2.

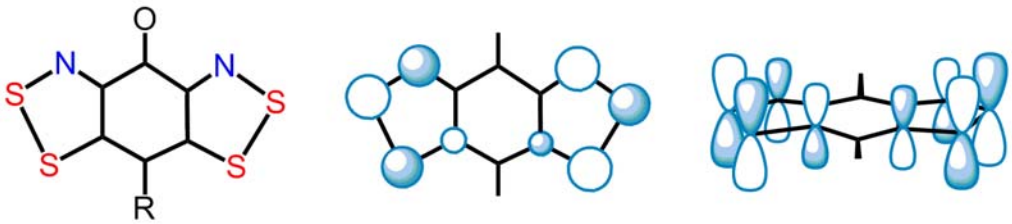

Figure 4.2. Idealized views of the π-SOMO of **4-1.**

[a] In the orthorhombic structures of **4-1a**·MeCN, **4-1a** and **4-1d** there is an absolute correspondence between the directions of the real and reciprocal unit cell vectors, while in the monoclinic structure of **4-1c** the correspondence is only approximate.

The results for **4-1a**, **4-1a**·MeCN and **4-1d** are summarized in Figure 4.3 in the form of dispersion curves for the SOMO-based COs (in the case of **4-1c**, its band structure will be discussed separately due to the complication of the crystal structure), which would constitute the $f = ½$ band if the ground state were metallic. The number of bands reflects the number of molecules in the unit cell and there are a total of twelve bands for **4-1a** and **4-1c**, but only four for **4-1a**·MeCN and **4-1d**. In each case the spread of the set across the Brillouin zone gives a qualitative estimate, within the tight-binding approximation, of the solid state bandwidth *W*. On this basis it is immediately apparent that the largest bandwidth is found for the acetonitrile adduct **4-1a**·MeCN (1.02 eV). The large dispersion observed along *a** and *c** also indicate a well-developed 2D-electronic structure, in accord with the slipped ribbon architecture illustrated in Figure 3.4 and 3.5. By contrast the unsolvated material **4-1a** shows only limited interactions along the π-stacks, and even weaker dispersion along the remaining two principal directions of reciprocal space. Overall, the bandwidth *W* is estimated to be 0.52 eV. The EHT electronic bandwidths for the radicals thus clearly indicate the ribbon-like π-stacked architecture of the solvated material **4-1a**·MeCN as having the most well-developed electronic structure, thus the most likely to display high conductivity. By contrast, in the unsolvated structure **4-1a** interactions are weaker, both in terms of magnitude and directionality, and indeed are reminiscent of those seen in the herringbone structures of pyridine-bridged radicals **4-2**. The remaining two structures (**4-1c** and **4-1d**) both possess alternating ABABAB π-stacked motifs. In the case of the phenyl derivative **4-1d** overlap along the head-over-tail π-stack sequence is quite strong, as indicated by the large dispersion along *a**, but the near absence of dispersion along *b** and *c** point to a highly 1D-system. Overall, the bandwidth (0.49 eV) is comparable to that found for **4-1a**.

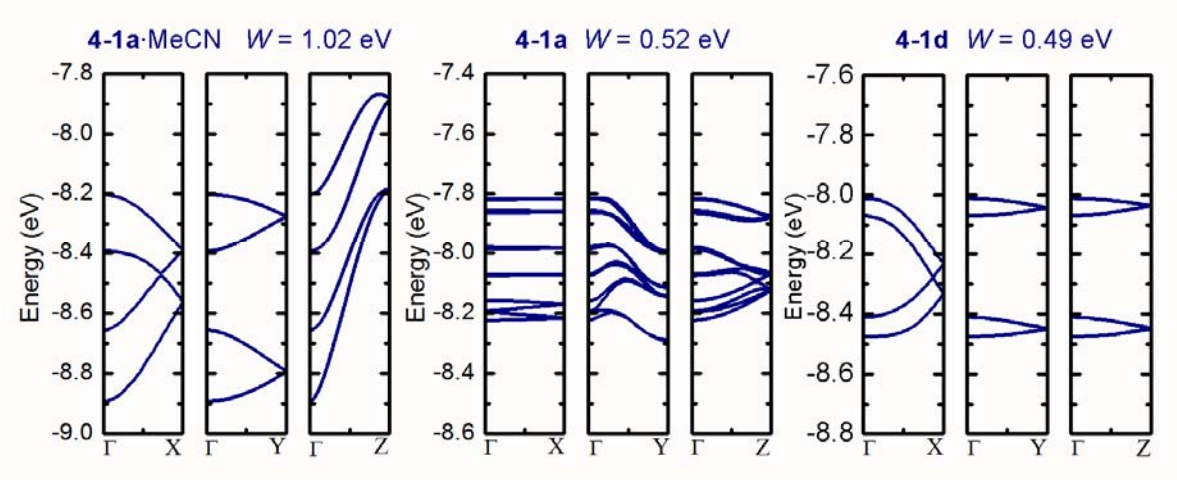

Figure 4.3. EHT crystal orbital dispersion curves for **4-1a**·MeCN, **4-1a**, and **4-1d**.

Given the unusual nature of the **4-1c** crystal structure, that is, the presence of two distinct sublattices, calculations were performed on several idealized structures, the first based on a single ribbon of **A** radicals, π-stacked along the *z* direction and running parallel to *y*; this is the architecture shown in Figure 3.10. The second model is the full 3D sublattice of **A** radicals, the honeycomb nature of which is illustrated by the space-filling superstructure in Figure 4.4. The effects of the inclusion of the sublattice of **B** radicals is then considered as a perturbation of the electronic structure of the **A** sublattice.

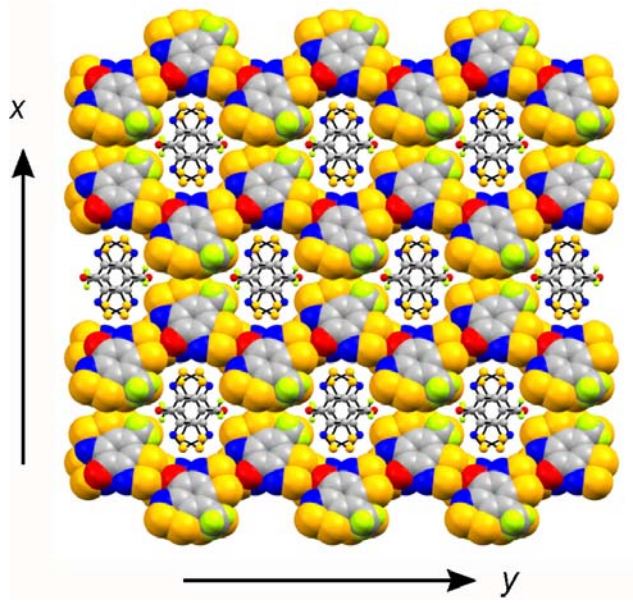

Figure 4.4. Two sublattices of **4-1c**, viewed parallel to the stacking direction, with **B** radicals occupying cavities generated between out-of-register ribbons of **A** radicals.

The results of the band structure calculations are summarized in Figure 4.5 in the form of dispersion curves along the direction Γ → Z for the SOMO-based COs. There are (i) four bands in the 2D lattice based on **A** radicals, (ii) eight bands for the full 3D lattice of **A** radicals, and (iii) twelve bands (8**A** + 4**B**) for the full 3D-lattice based on both radicals **A** and **B**. As may be seen in Figure 4.5 (i) the four COs are split into two pairs, an effect which can be traced back to the influence of the *trans*-antarafacial overlap (d11, Figure 3.11) which gave rise to the strong AFM exchange interactions $\boldsymbol{J}_1$ (which will be discussed in section 4.4.2). Nominally, and again speaking within the limits of the EHT model, this weak dimerization affords a very small band gap. On moving from the 2D to 3D lattice of **A** radicals, as in Figure 4.5 (ii), the band gap almost closes, as might be expected from the increase in dimensionality. Finally, when the cavities in the superstructure of **A** radicals are filled with π-stacks of **B** radicals (Figure 4.5 (iii)), a continuum of COs is generated, giving rise to an overall bandwidth W = 0.48 eV. That being said, the orbital interactions between the **A** and **B** radical π-stacks do not appear to be extensive, so that to a first approximation it is tempting to describe the overall structure in terms of the two separate sublattices, one being strongly antiferromagnetic or even diamagnetic, and the other open shell.

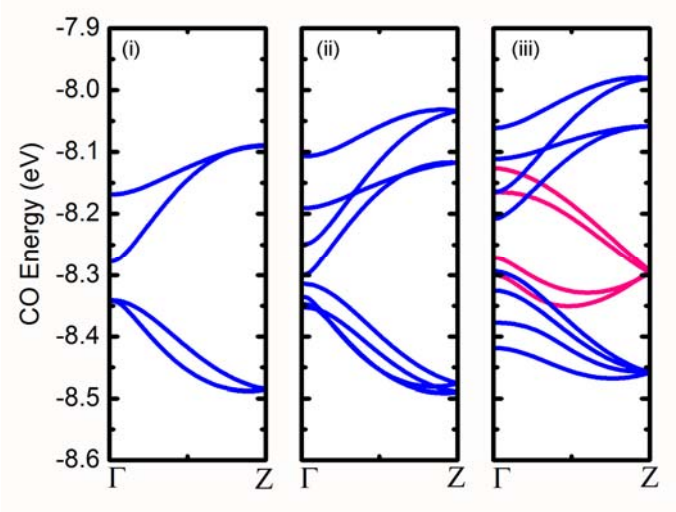

Figure 4.5. EHT band structure of different models of **4-1c**, showing (i) CO dispersion of a 2D array of **A** radicals, (ii) a 3D array of **A** radicals, and (iii) the full 3D structure with **A** and **B** radicals.

4.3 Conductivity

The crystal and band structures described above underscore the importance of both strong inter- and intrastack interactions between radicals in order to attain a high bandwidth. Variable temperature conductivity (σ) measurements have been performed on **4-1** over the temperature range 100-300 K using the 4-probe method on cold-pressed pellets. The results are illustrated in Figure 4.6, in the form of log plots of σ against $1/T$. Values of σ(300 K) and the Arrhenius activation energy E_{act} are summarized in Table 4.1. Comparison of the performance of the semiquinone-bridged radicals (**4-1**) with that of related pyridine-bridged materials (**4-2**), of which R_1 = Me, R_2 = Cl is representative[1] indicates that the semiquinone-bridged materials are generally superior, both in terms of enhanced conductivity and lowered activation energies. Indeed the values of σ(300 K) for **4-1a**, **4-1a**·MeCN are amongst the highest ever observed for a neutral f = ½ radical under regular pressure. Not only are they several orders of magnitude higher than in radicals of **4-2** for which σ(300 K) is generally in the range 10^{-6}-10^{-5} S cm^{-1}, they also rival the very best selenium-based variant, that is, 5×10^{-3} S cm^{-1} when R_1 = Me, R_2 = Cl.[3] And while the conductivity of these new radicals remains activated, indicative of a Mott insulating ground state, the value of E_{act} = 0.11 eV derived for **4-1a**·MeCN constitutes, to our knowledge, the lowest thermal activation energy ever reported for neutral f = ½ radical. By contrast, radicals **4-2** show E_{act} values in the range 0.40 - 0.50 eV,[1] while the best of their selenium analogues is lowered to 0.17 eV.[3]

Table 4.1. Conductivity parameters for **4-1** radicals.

	σ (300 K) (S cm^{-1})	E_{act} (eV)
4-1a·MeCN	1.0×10^{-3}	0.11
4-1a	4.0×10^{-3}	0.13
4-1b·MeCN	2.0×10^{-4}	0.16
4-1b	6.0×10^{-4}	0.13
4-1c	8.0×10^{-4}	0.12
4-1d	3.0×10^{-5}	0.20

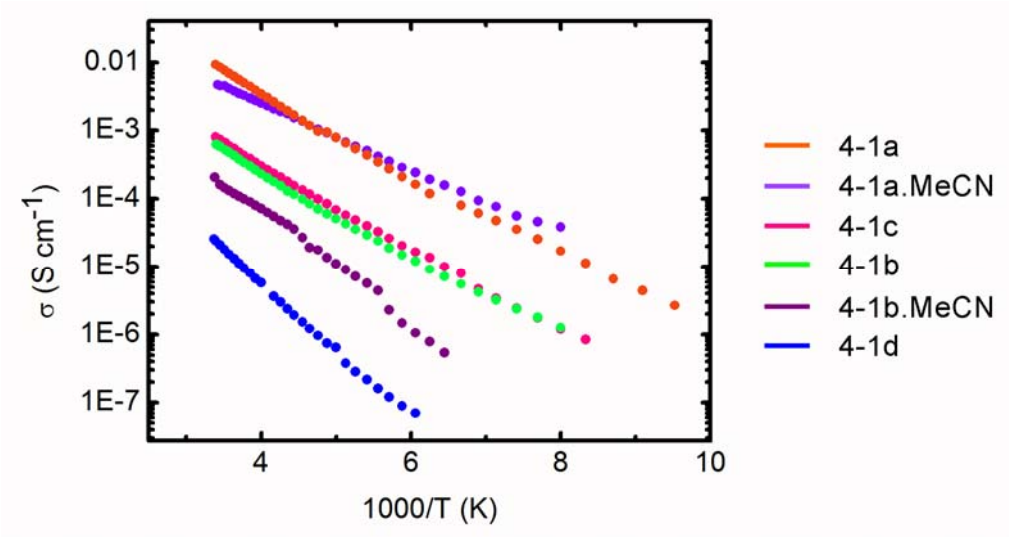

Figure 4.6. Variable temperature conductivity of **4-1** radicals.

4.4 Magnetism

Variable temperature DC magnetic susceptibility (χ) measurements (corrected for diamagnetic contributions)[4] from 300-2 K were performed on **4-1a**, **c**, **d** and the MeCN adduct of **4-1a** using an external field of H = 1 kOe. For all the non-solvated radicals (*i.e.,* **4-1a**, **c**, **d**) the results indicated bulk antiferromagnetic (AFM) coupling. The Curie constant (C) and Weiss constant (θ) values were obtained from Curie-Weiss fits, which are summarized in Table 4.2, with the exception of **4-1c** (see section 4.4.2). The subsequent zero-field cooled / field cooled (ZFC-FC) experiments at low field (*i.e.,* 100 Oe) on non-solvated materials revealed a sharp bifurcation in the χT for the ZFC and FC plots, which is indicative of a phase transition to a spin-canted AFM ordered state with Néel temperature (T_N). Field independent magnetization experiments were used to confirm the ordering temperature, and back-extrapolation of M to T = 0 K afforded a value of the spontaneous magnetization M_{spont} which was used to estimate the spin canting angle following equation 4.1. The saturation magnetization (M_{sat}) for a S = ½ ferromagnet with g = 2 was set arbitrarily at 1 Nβ, which can be calculated using equation 4.2. The calculated spin canting angles along with the T_N values are also summarized in Table 4.2.

$$\phi = \sin^{-1}\left(\frac{M_{spont}}{M_{sat}}\right) \quad \textbf{(4.1)}$$

$$M_{sat} = gNS\beta \quad \textbf{(4.2)}$$

Table 4.2. Magnetic parameters of **4-1a**, **d**, and **4-1a**·MeCN.

	4-1a·MeCN	**4-1a**	**4-1d**
C (emu K mol^{-1}) [a]	0.389	0.351	0.349
θ (K) [a]	-61.7	-27.0	+32.8
$\boldsymbol{J}$ (cm^{-1})	-32.4 [b]	-----	29.5 [c]
$z\boldsymbol{J}'$ (cm^{-1})	12.8 [b]	-----	-2.5 [c]
ϕ (°)	-----	0.14	-----
T_N (K)	-----	8.0	4.5

[a] From a Curie-Weiss fit to the 100-300 K data. [b] From a fit to the 50-300 K data using a molecular-field modified Bonner-Fisher 1D S = ½ AFM coupled chain model. [c] From a fit to the 6-30 K data using the Baker model for a Heisenberg 1D FM coupled chain of S = ½ centers.

4.4.1 Magnetism of 4-1a and 4-1a·MeCN

In the solid state **4-1a** adopts a slipped ribbon type of π-stack (type iii) while **4-1a**·MeCN adopts a herringbone motif (type i). The cooling curve plots of χT *vs.* T (as illustrated in Figure 4.7) indicated that both materials behave as AFM coupled paramagnets over the range 100-300 K; C and θ values obtained from Curie-Weiss fits are provided in Table 4.2. In the case of **4-1a**·MeCN the data was also fitted using a molecular-field modified Bonner-Fisher 1D S = ½ AFM coupled chain model[5] referenced to the Heisenberg Hamiltonian $H_{ex} = -2\boldsymbol{J}\{S_1 \cdot S_2\}$, from which we obtained values of exchange coupling constants $\boldsymbol{J}$ = -32.4 cm^{-1} for interactions along the π-stacks, and $z\boldsymbol{J}'$ = 12.8 cm^{-1} for the cumulative interstack (mean field) interactions. There is no evidence for a structural or magnetic phase transition on cooling the sample to 2 K. The data for the unsolvated material **4-1a** could not be fit to a simple 1D AFM chain model, a result which is perhaps not surprising given the complexity of the structure, with

three independent radicals in the asymmetric unit. That being said, this latter compound displays a rapid surge in χT on cooling below 10 K, an effect more easily observed in a plot of χ *vs.* T with H = 100 Oe (Figure 4.7b insert). According to the ZFC-FC experiments there is a phase transition to a spin-canted AFM ordered state at 8 K. Field independent magnetization experiments (Figure 4.7c) confirmed the ordering temperature, and the spontaneous magnetization M_{spont} = 2.5 mNβ was used to estimate the spin-canting angle ϕ = 0.14°. Measurements of M as a function of field were also performed, and these indicated a weak, quasi-linear M *vs.* H dependence up to 5 K. Cycling of the field revealed a subtle but distinct hysteretic response in M (Figure 4.7 (d)), giving rise (at 2 K) to a coercive field H_c = 80 Oe.

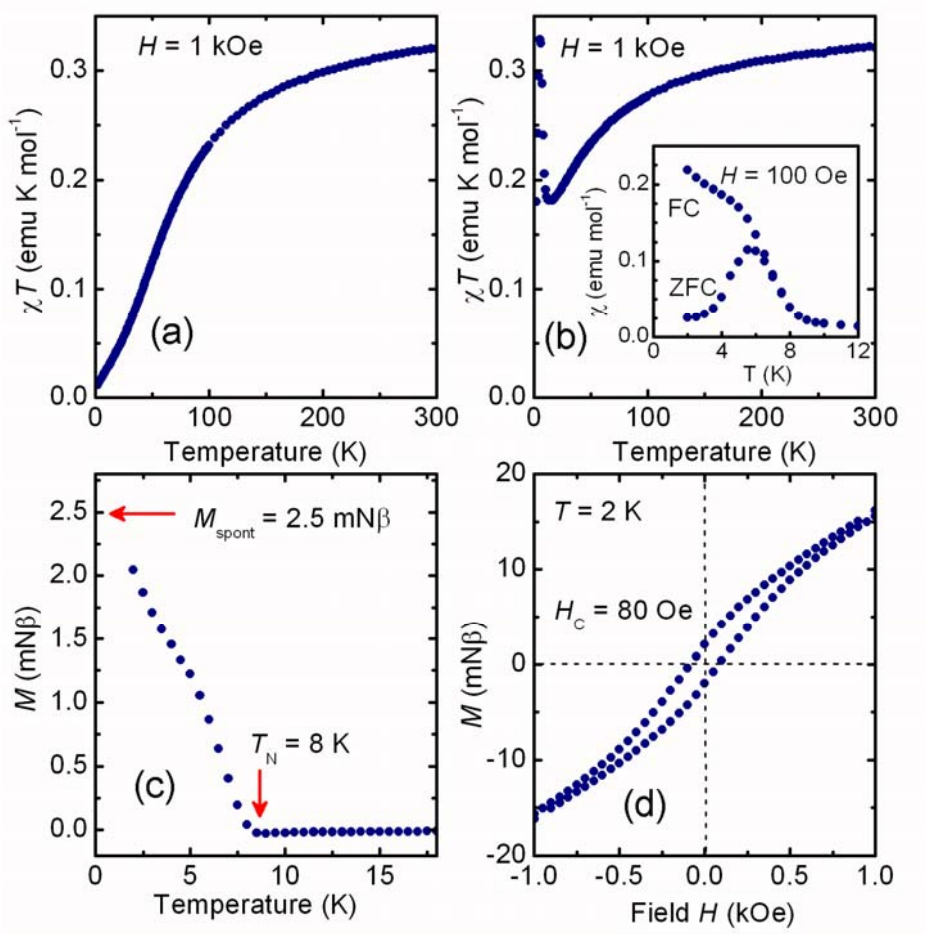

Figure 4.7. (a) Field-cooled χT *vs.* T plot at H = 1 kOe for **4-1a**·MeCN. (b) Field-cooled χT *vs.* T plot at H = 1 kOe for **4-1a**, with insert showing a ZFC-FC plot of χ *vs.* T at H = 100 Oe. (c) Decay in spontaneous magnetization M *vs.* T plot, and (d) hysteresis in cycling of M *vs.* H measurements at T = 2 K.

4.4.2 Magnetism of 4-1c

Similar variable temperature DC magnetic susceptibility (χ) measurements on **4-1c** have been carried out over the temperature range 300-2 K. The results are illustrated in Figure 4.8 in the form of cooling curve plots of χ and χT versus T measured using an external field of H = 1 kOe. Inspection of the χT versus T plot suggests a strong AFM response, since for a paramagnetic S = ½ system with a value of g ~ 2 the high temperature limit of χT should fall near 0.375 emu K mol^{-1}. In this case, χT(300K) is near 0.20 emu K mol^{-1}. However, attempts to perform even a Curie-Weiss fit to the high temperature data were completely unsuccessful, a finding that we attribute to the fact that crystal structure contains two different S = ½ sublattices, one based on **A** radicals, with eight spins per cell, and the other composed of **B** radicals, with four spins per cell. In addition, the large number of close intermolecular contacts between pairs of **A** radicals, pairs of **B** radicals, and hybrid **A-B** pairs suggests a complex array of strong magnetic interactions, and a consequent magnetic structure which is unlikely to conform to a description based on a 1D- or 2D-magnetic (chain or ladder) model, let alone follow Curie-Weiss behavior.

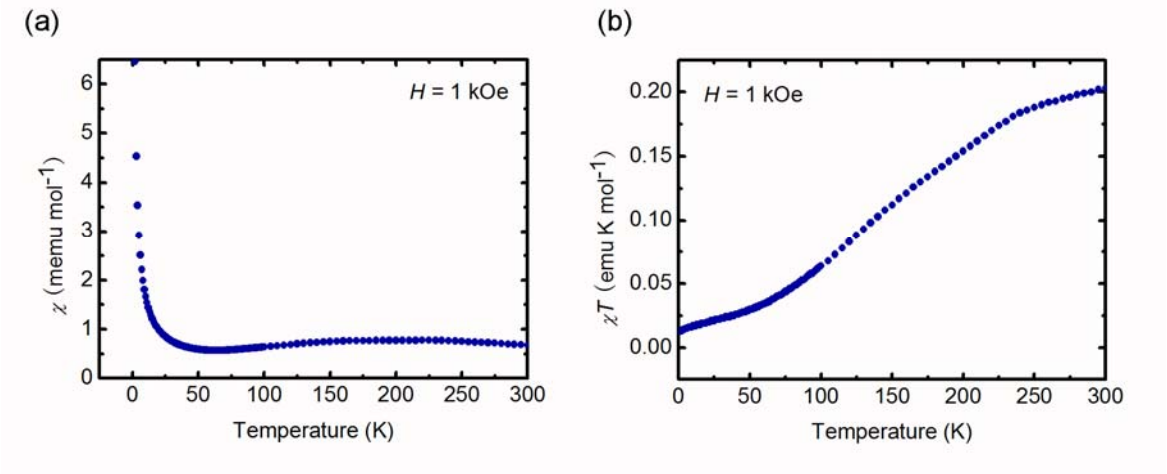

Figure 4.8. (a) Field-cooled χ versus T and (b) χT versus T plots for **4-1c** at H = 1 kOe.

That being said, some level of understanding of the dominant magnetic interactions of **4-1c** can be reached by using DFT calculations to estimate pairwise exchange energies ***J*** between radicals in the

A and **B** π-stacks, that is, the values of $\boldsymbol{J}_1$, $\boldsymbol{J}_2$ and $\boldsymbol{J}_3$ shown in Figure 4.9. These three dimers were previously defined respectively by the close contacts d11, d7 and d6 in Figure 3.10 and Figure 3.11. Based on the previous experience with π-stacked radicals of this type, it is these π-stack interactions, rather than those involving lateral interstack approaches, that are most likely to produce a strong AFM response. The computational approach, which has been successfully applied to a variety of nitrogen-centered radicals,[6] heterocyclic thiazyls[7] and phenalenyls,[8] employs exchange energies estimated from broken symmetry DFT methods developed by Noodleman and Yamaguchi.[9] Accordingly, and with reference to the Heisenberg Hamiltonian $H_{ex} = -2\boldsymbol{J}\ \{S_1 \cdot S_2\}$, the exchange energy $\boldsymbol{J}$ for any pair of interacting radicals (as shown in Figure 4.9) can be estimated from the total energies of the triplet (E_{TS}) and broken symmetry singlet (E_{BSS}) states and the respective expectation values $< S^2 >$ of the two states, according to equation 4.3. Single point total energies E_{TS} and E_{BSS} were calculated using the hybrid exchange correlation functional UB3LYP and polarized, split-valence basis sets with double-zeta (6-31G(d,p)) functions. Atomic coordinates were taken from the crystallographic data.

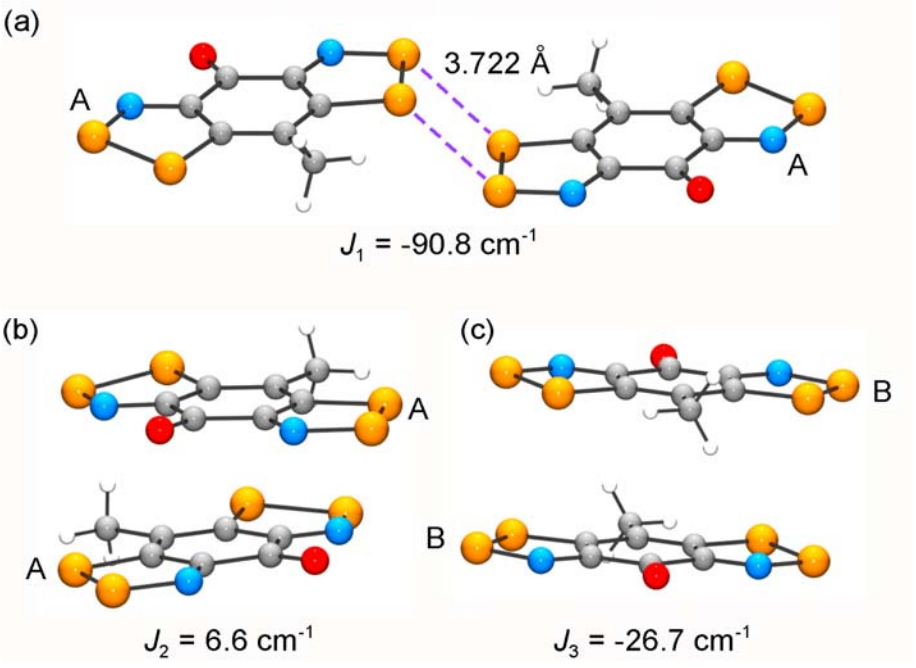

Figure 4.9. Unique pairwise magnetic exchange interactions in **4-1c**.

$$J = \frac{-(E_{TS} - E_{BSS})}{< S^2 >_{TS} - < S^2 >_{BSS}} \qquad \textbf{(4.3)}$$

In the pyrazine-bridged radical **4-3**,[2] which displays a similar alternating π-stack architecture (see Figure 3.12), with four-center, *trans*-antarafacial approaches of radicals akin to that which gives rise to $\boldsymbol{J}_1$ are also found (Figure 4.10a), with comparable S···S′ separations (3.831 Å) to those found here (d11 = 3.722 Å). The associated negative exchange energy ($\boldsymbol{J}$ = −108.4 cm^{-1}) may contribute to the strong antiferromagnetic response observed for this compound.[a] However, the magnitude of these exchange interactions falls far short of those seen in more localized radical dimers, such as the centrosymmetrically bridged *m*-cyanophenyl-dithiadiazolyl[10] and many salts of the binary cation $S_3N_2^+$, including $[S_3N_2][AsF_6]$.[11] In these systems (Figure 4.10b and 4.10c) the S···S′ bridges are much shorter, so that the electronic structures of the dimers should no longer be considered as an open shell singlets,[12] but rather as a closed shell singlets which are best described in terms of a classical 4-center 2-electron bond model.[13]

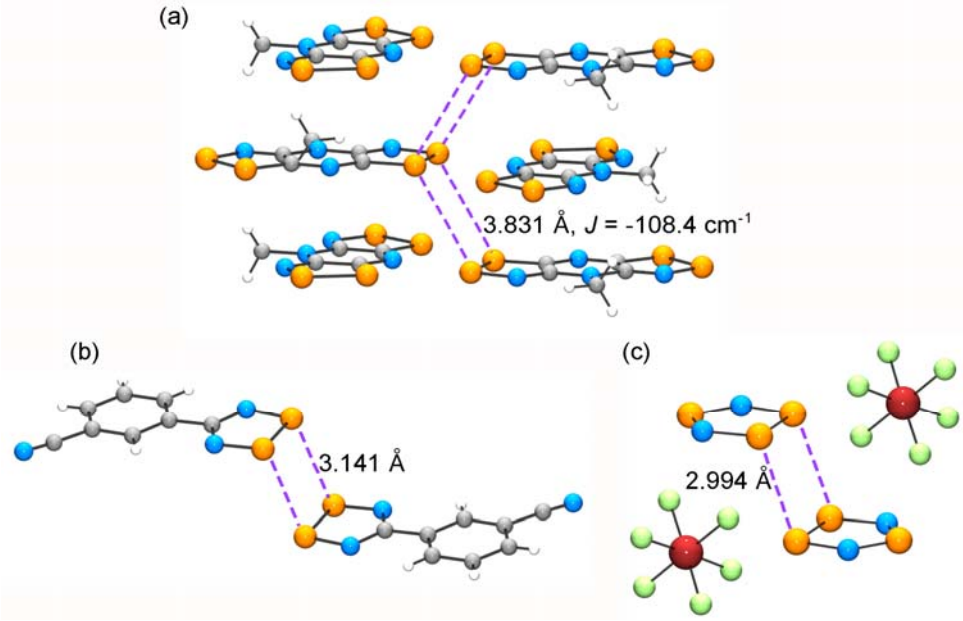

Figure 4.10. Centrosymmetric four-center S···S′ contacts in (a) the pyrazine-bridged bisdithiazolyl **4-3**, R = Me, (b) *m*-cyanophenyl-dithiadiazolyl and (c) $[S_3N_2][AsF_6]$. In the case of **4-3**, R = Me the estimated exchange energy is also provided.

[a] There is also a non-centric four-center interaction in **4-3**. At 295 K the two S···S′ distances are longer (3.936 and 4.093 Å), but the calculated exchange energy ($\boldsymbol{J}$ = 61.1 cm^{-1}) suggests strong AFM coupling.

4.4.3 Magnetism of 4-1d

The alternating π-stack motif (type ii) found for **4-1d**, coupled with the paucity of close intercolumnar S···S′ contacts, suggests a relatively one-dimensional electronic structure which might be considered susceptible to a symmetry-lowering, spin-pairing instability, as observed in related radicals with ABABAB π-stacked structures.[2] However, the variable temperature magnetic susceptibility (χ) measurements establish that this is not the case. The plot of χT (field cooled) *vs. T* (as shown in Figure 4.11) indicates paramagnetic behaviour, with strong local FM interactions; a Curie-Weiss fit to the data above 100 K affords C = 0.349 emu K mol^{-1} and θ = +32.8 K. Application of the Baker model[14] for a Heisenberg 1D FM coupled chain (π-stack) of S = ½ centers to the data over the range T = 6-30 K yields the $\boldsymbol{J}$ and $z\boldsymbol{J}'$ values of 29.5 cm^{-1} and -2.5 cm^{-1} respectively.

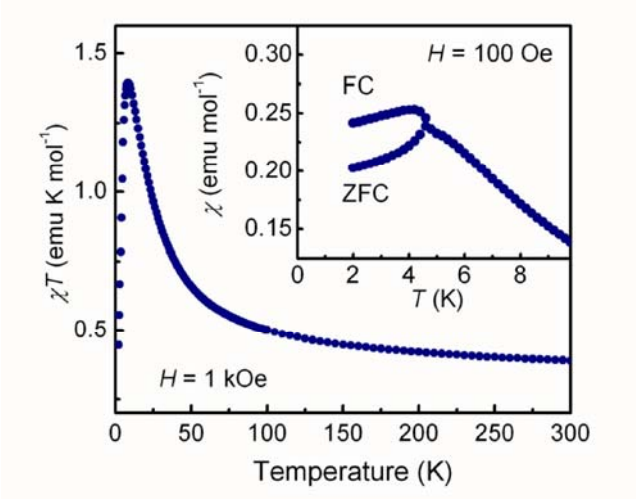

Figure 4.11. Plot of χT *vs. T* for **4-1d** at H = 1 kOe. Inset shows ZFC-FC plots of χ *vs. T* at H = 100 Oe.

Additional measurements at lower fields revealed the onset of a slight low temperature discontinuity in χ(T) for H < 200 Oe, and subsequent ZFC-FC experiments at H = 100 Oe (Figure. 4.11, inset) established a phase transition at 4.5 K. The resulting state may be viewed in terms of spin-canted AFM ordering based on the antiparallel alignment of the FM coupled chains (π-stacks). The degree of canting is, however, very small, as no spontaneous magnetization could be detected. The value of T_N =

4.5 K obtained from the ZFC-FC measurements nonetheless compares well with that (6.2 K) estimated using the expression $kT_C \approx 2S^2 (|\, z\boldsymbol{J}' \,| \cdot \boldsymbol{J})^{½}$,[15] which may be derived from mean field theory, with $S = ½$ and using values of $\boldsymbol{J}$ and $z\boldsymbol{J}'$cm^{-1} obtained from the Baker fit to the 1D FM chain model.

Magnetization (M) *vs* field (H) measurements (Figure 4.12, left) on **4-1d** at different temperatures have provided additional insight into its magnetic structure. At $T = 2$ K, for example, the value of M rises sharply with H, reaching a plateau at 1.00 Nβ, the saturation value expected for a $S = ½$ system with a nominal $g \approx 2$, just above $H = 20$ kOe. There is no evidence of hysteresis. At temperatures above T_N, M rises less steeply, and with decreasing dM/dH, so that saturation does not occur out to $H = 50$ kOe, the limit of the experiment. These results are broadly consistent with metamagnetic behavior,[16] in which the antiparallel alignment of the FM ordered radical π-stacks is parallel, producing a field-induced FM ordered material. However, a characteristic feature for such systems is an inflexion in the *M vs. H* plot, with dM/dH reaching a maximum at the field where magnetic realignment occurs. Several non-metallic radicals and radical ions displaying this behaviour have been reported.[7f,17] In this case, however, no inflexion is observed in the *M vs. H* plot, nor is any maximum apparent in the *dM/dH vs. H* plot (Figure 4.12, right) prior to saturation, even at $T = 2$ K. This result, plus the fact that ZFC-FC measurements establish that AFM ordering collapses above $H = 200$ Oe, is more consistent with a spin-flop transition.[18] The profiles of the *M vs. H* curves at $T > T_N$ are also in keeping with such a process.[18a,b]

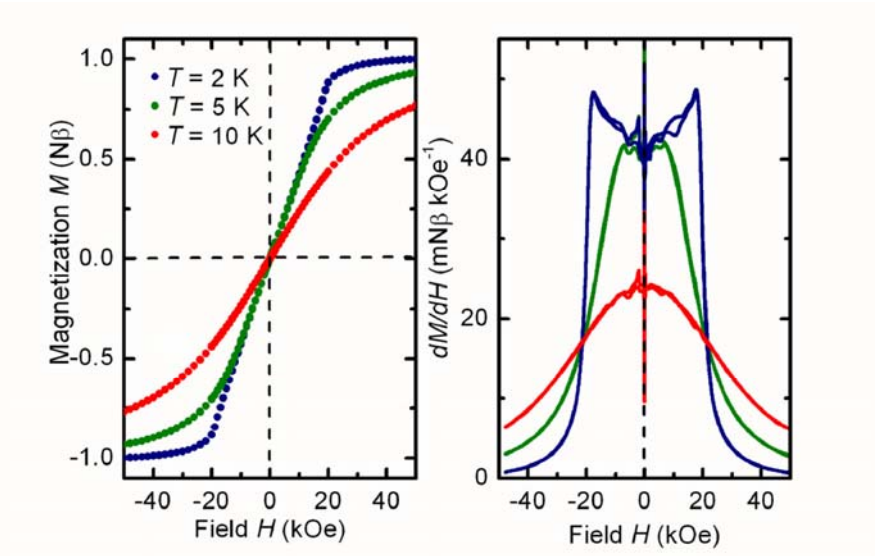

Figure 4.12. Plots of *M vs. H* (left) and *dM/dH vs. H* (right) for **4-1d** at $T = 2$, 5 and 10 K.

4.5 Discussion

The semiquinone-bridged *bis*-dithiazolyls (**4-1)** constitute the first members of a new class of resonance stabilized π-radical for use in the design of $f = ½$ conductors. Their electrochemical cell potentials, which are lower than those observed for the pyridine-bridged radicals **4-2**, augur well for an improved performance by virtue of a reduced onsite Coulomb repulsion term *U*. Moreover, in contrast to the pyridine-bridged systems, where the *N*-alkyl group creates an insulating buffer between neighboring molecules, the carbonyl oxygen atom in **4-1** plays an active structure-making role, giving rise to tightly packed structures linked by short intermolecular S···O′ and S···N′ contacts (as shown in Figure 4.13). These supramolecular synthons afford a rich variety of novel packing motifs, including the head-over-tail motif found for **4-1c**, **d** and the stacked ribbon architecture found in **4-1a**·MeCN (as illustrated in Figure 4.1). Only in the case of the unsolvated radical **4-1a** does the packing of the π-stacks resemble the herringbone pattern typically observed for pyridine-bridged radicals **4-2**.

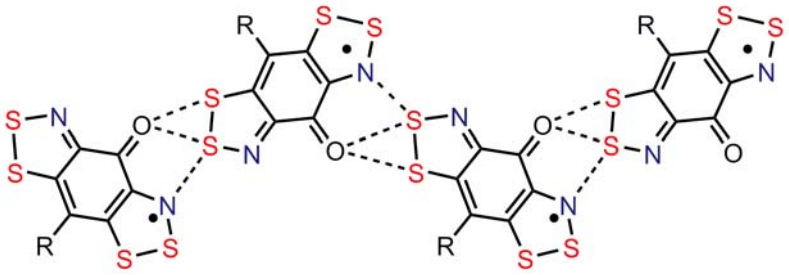

Figure 4.13. Ribbon-like arrays of radicals created by intermolecular S···O′ and S···N′ supramolecular synthons.

These new structural motifs give rise to interesting magnetic properties. The head-over-tail π-stacking previously found for **4-1d** affords remarkably strong FM interactions along the π-stacks, and upon cooling to 4.5 K the FM chains undergo AFM ordering. Similarly **4-1c** also adopts the head-over-tail π-stacking motif, however a fairly strong AFM interaction was observed along the π-stack. In the case of **4-1a** (unsolvated) AFM ordering is also observed, but the unusual crystal structure, with three independent molecules in the asymmetric unit, precludes a detailed interpretation of its magnetic structure. Attempts to model the $\chi(T)$ data above 100 K to either a 1D FM or AFM chain $S = ½$ model were unsuccessful. This is, perhaps, not unexpected, given that there are three distinct π-stacks (**A**, **B** and **C**), but given this structural complexity it is surprising that the bulk material is capable of ordering magnetically. The origin of the strong local AFM interactions in the solvated material **4-1a**·MeCN is a little clearer. The $\chi(T)$ data from 150-300 K could be fitted using a molecular-field modified Bonner-Fisher 1D $S = ½$ AFM coupled chain model[5] which, when referenced to the Heisenberg Hamiltonian $H_{ex} = -2\boldsymbol{J}\{S_1 \cdot S_2\}$, afforded values of $\boldsymbol{J}$ and $z\boldsymbol{J}'$ of −32.4 and 12.8 cm^{-1} respectively. However, modeling the 2-100 K data produced an equally acceptable fit, but with $\boldsymbol{J} = -38.1$ cm^{-1} and $z\boldsymbol{J}' = 45.2$ cm^{-1}. The variation in the mean field zJ' term perhaps indicates the inadequacy of the 1D model, or may simply reflect changes in exchange energies occasioned by contraction of the cell on cooling.

However, it is the charge transport properties of these semiquinone-bridged materials that are their most remarkable and appealing features. As a set the structures **4-1a**, **4-1a**·MeCN, **4-1b**, **c** and **d**

display room temperature conductivities several orders of magnitude higher than those of their pyridine-based counterparts **4-2**. Thermal activation energies are correspondingly much lower, lower indeed than those observed in selenium based variants of **4-2**, where the heavy atom effect affords improved orbital overlap (a larger *W*) and a softer core (a lower *U*). The question therefore arises as to the origin of this improved performance in the semiquinone materials. Is it a result of an intrinsically lower *U*, or an improved bandwidth *W*, or are there additional features which need to be considered? In essence the operational guidelines provided by Mott-Hubbard theory seem to work, at least qualitatively. As noted above, the electrochemical evidence suggests an intrinsically lower *U*, and the π-stacked slipped ribbon architecture for **4-1a**·MeCN clearly provides a significant enhancement in *W*.

Chapter 5

Ongoing and Future Work

5.1 Incorporation of Selenium

The conductivity of radicals is related to the ratio of the bandwidth, *W* to the on-site Coulomb repulsion energy, *U*, as previously discussed in Chapter 1. When *W* is larger than *U*, the material should exhibit metallic conductivity. Since *W* is equal to 4β, where β is the resonance integral, one way to increase the bandwidth is to enhance the orbital overlap, by incorporating the heavier chalcogen Se which has more diffuse orbitals (*ca.* covalent radius r_{cov} = 117 pm)[1] than S (*ca.* covalent radius r_{cov} = 103 pm)[1]. The effects of replacing S with Se on structure and transport properties were recognized early on in the development of charge transfer salts[2] and were also explored during early studies of dithiadiazolyl radicals (*i.e.*, **5-1** and **5-2**).[3] The incorporation of Se into sulfur-nitrogen ring systems has been shown to increase the bandwidth in the BP framework (**5-3**). The synthesis, structures and transport properties of Se containing radicals have been thoroughly investigated for this framework (**5-4** to **5-6**).

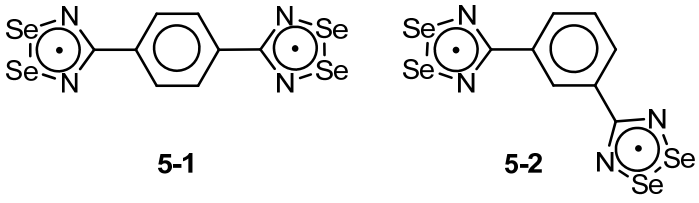

5-1

5-2

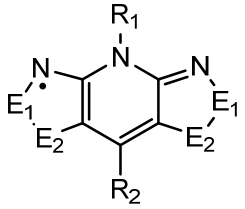

	5-3	5-4	5-5	5-6
E_1	S	S	Se	Se
E_2	S	Se	S	Se

Incorporation of Se at the E_1 position ([**5-5**]$^+$) can be achieved in a one-step reaction, by refluxing a soluble salt of **[5-3]**$^+$ (*e.g.,* OTf^-, SbF_6^- salt) and SeO_2 over several days (as shown in Scheme 5.1) in MeCN or acetic acid solution.[4]

Scheme 5.1

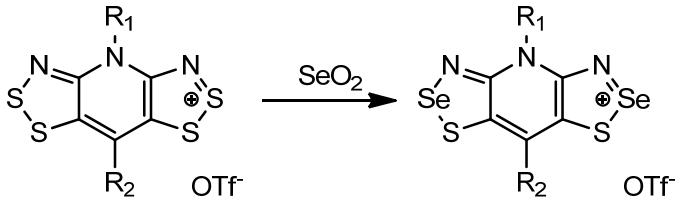

[5-3]$^+$ **[5-5]**$^+$

By contrast, the incorporation of Se at the E_2 position requires a multiple step synthetic methodology starting from 2,6-diaminopyridine (as illustrated in Scheme 5.2). The reduction of the *bis*-selenocyanate molecule **5-7** and subsequent methylation affords **5-8**, which undergoes a condensation reaction with $SOCl_2$ to give [**5-9**][Cl] with Se in the E_2 position. In addition, a series of reactions are required to incorporate different R_1 and R_2 groups to give a soluble OTf^- salt of [**5-4**]$^+$. The reaction of [**5-4**][OTf] with SeO_2 leads to the all Se analogue [**5-6**]$^+$ (see Scheme 5.2). The subsequent reduction of the cations [**5-4**]$^+$, [**5-5**]$^+$ and [**5-6**]$^+$ with a suitable reducing agent using the H-cell method leads to the corresponding radicals.[5]

In the case of R_1 = Et and R_2 = Cl, the Se analogues (**5-4** to **5-6**) are isostructural to the all-sulfur compound (**5-3**). These materials display a general trend of increasing conductivity and lower activation energies with increasing Se content. Compared with **5-3** (R_1 = Et and R_2 = Cl), the all Se compound **(5-6**, R_1 = Et and R_2 = Cl) exhibited an increase in conductivity of two orders of magnitude (as shown in Figure 5.1) with a significant decrease of the activation energy E_a (*i.e.,* 0.43 eV to 0.19 eV).[5]

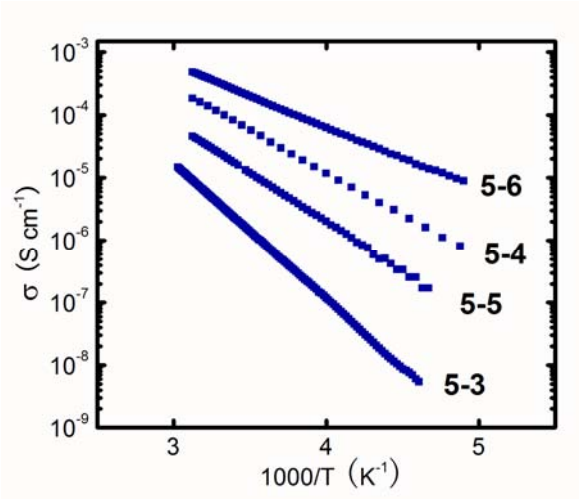

Figure 5.1. Log σ versus $1/T$ plots for **5-3** to **5-6**.

Scheme 5.2

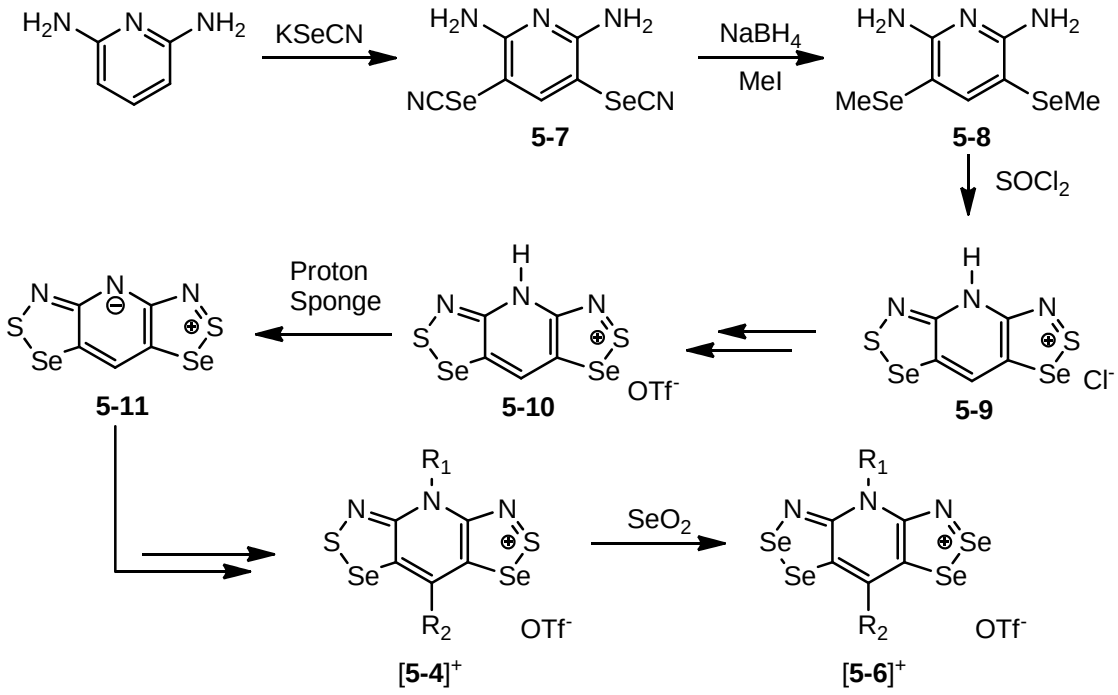

In the case of the **5-5** compound, where R_1 = Me, R_2 = H, F and Me the radicals crystallized as centrosymmetric σ dimers (as shown in Scheme 5.3).[4a,6]

Scheme 5.3

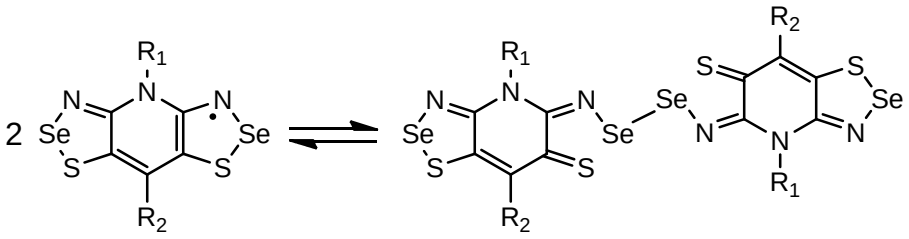

At room temperature, the σ dimers are diamagnetic species with low conductivity (10^{-6} S cm^{-1}), however under external pressures of over 5 GPa, the conductivity of **5-5** (R_1 = Me and R_2 = H, F, Me) increases by five to six orders of magnitude.[7] This is due to a phase change under pressure, which changes the solid state packing, as determined by XRD, and leads to a weakly metallic state.[8]

5.1.1 Synthetic Procedures

Applying a similar synthetic methodology previously described for the BP framework, the Se analogue of the semiquinone-bridged *bis*-dithiazolyl [**5-12**]$^+$ can be prepared in one step, as shown in Scheme 5.4. However, more forcing conditions *i.e.,* higher temperature and longer reaction times are often required.

Scheme 5.4

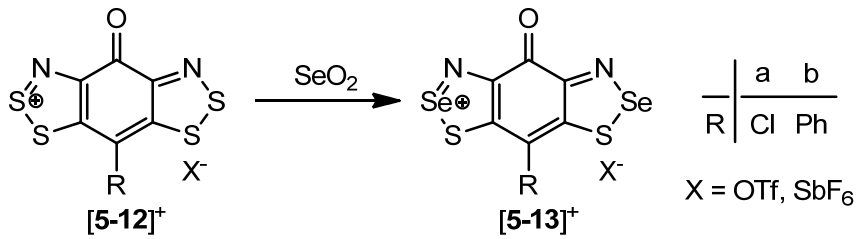

For example, in a typical reaction the cation [**5-12**]$^{+}$ as a OTf^{-} or SbF_6^{-} salt was refluxed with freshly ground SeO_2 in acetic acid or propionitrile (EtCN) solution for two hours (R = Cl) or two days (R = Ph) to yield a greenish blue solution, which upon cooling to room temperature, led to a copper-colored microcrystalline solid. The purity of the product ([**5-13**]$^{+}$) was high, which was checked by Electro-Spray Ionization Mass Spectroscopy (ESI-MS).

5.1.2 Preparation of [5-13a][X]

The Se insertion of [**5-12a**]$^{+}$ was initially performed in refluxing acetic acid . When ~ 2 mmol of [**5-12a**]$^{+}$ was refluxed with 2.5 equivalent of SeO_2 for 2 h, the product precipitated out of solution on cooling as a mixture of 85 % Se_2 and 15 % Se_1 (as shown in Scheme 5.5).

Scheme 5.5

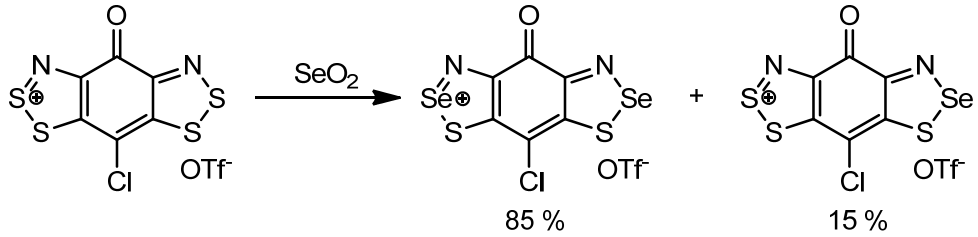

When the reaction was scaled up, the yield of the desired product was lower due to the poor solubility of the OTf^{-} salt in acetic acid. Therefore the more soluble SbF_6^{-} salt of [**5-12a**]$^{+}$ was employed and after refluxing for 2 h in acetic acid, the blue solution was gradually allowed to cool to room temperature over 24 h to afford a golden brown precipitate which was collected by filtration. An attempt to recrystallize [**5-13a**][SbF_6] from MeCN was unsuccessful, because of the high solubility of the salt in MeCN. Therefore the SbF_6^{-} salt was metathesized with ^{n}BuNOTf in MeCN to give [**5-13a**][OTf] as golden brown microcrystalline flakes and the purity was determined by ESI-MS.

5.1.3 Preparation of [5-13b][OTf]

In the case of R = Ph, a solution of [**5-12b**][OTf] in acetic acid was refluxed with SeO_2 for 16 h, but led only to the recovery of starting material. A prolonged reaction in acetic acid for 60 h gave the desired product [**5-13b**][OTf] as determined by ESI-MS. An attempt to recrystallize [**5-13b**][OTf] from hot MeCN led to a large amount of insoluble material and its infrared spectrum suggested significant decomposition had occurred during the Se insertion reaction in acetic acid. Therefore, the Se insertion reaction was carried out with 3 equivalents of SeO_2 in EtCN (bp = 97 °C, *c.f.* bp = 118 °C for acetic acid) at 140 °C. After 2 days the ESI-MS indicated a 50 / 50 mixture of starting material and a cation containing only one Se atom. An additional 40 h of heating did not change the reaction mixture composition. Therefore the reaction was performed with 6 equivalents of SeO_2 in EtCN at 140 °C for 40 h which led to a dark green-blue solution containing predominately [**5-13b**][OTf] and a small amount of cation containing only one Se atom and starting materials as determined by ESI-MS. The solution was allowed to slowly cool to room temperature and a crystalline precipitate was collected by filtration and subsequent recrystallization from MeCN led to red needles of [**5-13b**][OTf].

5.1.4 Bulk Reduction

A bulk reduction of [**5-13a**][OTf] salt using octamethylferrocene as the reducing reagent in MeCN gave a golden brown microcrystalline precipitate in nearly quantitative yield. Due to the low solubility of the **5-13a** radical, the solution EPR spectrum could not be obtained in common organic solvents. A two-probe conductivity measurement of this material indicated a high resistivity, ~ 10^5 Ω, which suggests this material is a poor conductor ($\sigma \leq 10^{-5}$ S/cm) and may form σ-dimers similar to **5-5** (*vida infra*). In addition, compared with **5-12a** the ν(CO) of **5-13a** was shifted significantly (*ca.* from 1600 cm^{-1} to 1500 cm^{-1}), which may be caused by strong Se···O′ interactions, which is associated with

the diamagnetic species. Therefore the structure and transport properties (*i.e.,* high pressure conductivity) of **5-13a** may be of interest in the future.

The reduction of pure [**5-13b**][OTf] with octamethylferrocene in degassed MeCN gave a dark grey powder and the two-probe conductivity measurements again indicated a very low conductivity for **5-13b**, similar to that observed for **5-13a**.

5.1.5 Experimental Details

Preparation of [5-13a][OTf]. [**5-12a**][SbF_6] (1.501 g, 2.91 mmol) was refluxed in 500 mL glacial HOAc and hot filtered to remove insoluble materials, and then powdered SeO_2 (1.109 g, 9.99 mmol) was added to the filtrate. After refluxing for 2 hrs, the solution was allowed to slowly cool to room temperature overnight and a copper-bronze microcrystalline solid (1.153 g, 1.89 mmol; 65.0 % yield) was collected by filtration. To a solution of [**5-13a**][SbF_6] in MeCN (80 mL), $^{n}Bu_4NOTf$ (0.745 g, 2.23 mmol) was added and the mixture was stirred at room temperature for 1 h, the [**5-13a**][OTf] precipitated out as golden brown flakes which were collected by filtration and washed with DCM to give 0.790 g (1.34 mmol, 71 % yield) of product. IR (cm^{-1}):1683 (m), 1422 (s), 1268 (m), 1230 (s), 1189 (w), 1168 (w), 1093 (w), 1026 (m), 899 (w), 843 (w), 751 (m), 737 (m), 633 (s), 573 (w), 519 (w).

Preparation of [5-13b][OTf]. In a glass bomb, [**5-12b**][OTf] (0.200 g, 0.425 mmol) was refluxed with powdered SeO_2 (0.304 g, 2.74 mmol) in 30 mL of EtCN at 140 °C for 42 h to give a greenish blue solution. Upon cooling, the products were precipitated out as red micro-crystals which were then collected by filtration to give 0.123 g (0.235 mmol, 55 % yield) of product. IR (cm^{-1}): 1668 (s), 1427 (s), 1407 (s), 1318 (w), 1307 (w), 1281 (s), 1233 (s), 12151 (s), 1183 (m), 1174 (m), 1165 (m), 1085 (w),

1048 (w), 1023 (s), 880 (w), 857 (w), 842 (w), 786 (m), 734 (m), 658 (m),643 (m), 637 (m), 574 (w), 523 (w), 512 (w), 494 (w), 448(w).

Preparation of 5-13a. Octamethylferrocene (30 mg, 0.10 mmol) was added to a bubble degassed (N_2) suspension of [**5-13a**][OTf] (36 mg, 0.069 mmol) in 25 mL of degassed MeCN at room temperature. After stirring for 5 h, the gold brown microcrystalline precipitate was collected by filtration and dried *in vacuo* (16 mg, 0.043 mmol, 62 % yied). IR (cm^{-1}): 1666 (w, b), 1519 (s), 1337 (s, b), 1228 (s, b), 1217 (s, b), 1133 (m), 1020 (m), 898 (m), 815 (w), 729 (m), 613 (m), 593 (m), 437 (m).

Preparation of 5-13b. **5-13b** was prepared the same way as **5-13a**, using [**5-13a**][OTf] (20 mg, 0.038 mmol) and octamethylferrocene (17 mg, 0.059 mmol) in 10 mL of degassed MeCN, yielded a dark grey precipitate (12 mg, 0.029 mmol, 76 % yield). IR (cm^{-1}): 1551 (s), 1503 (m), 1480 (s), 1305 (w), 1289 (w), 1272 (w), 1247 (w), 1232 (w), 1152 (m), 1123 (w), 1074 (w), 1025 (w), 996 (w), 968 (w), 921 (w), 878 (w), 846 (w), 784 (w), 735 (s), 698 (m), 666 (m), 653 (m), 615 (m), 547 (m), 527 (m), 484 (w).

5.2 Other R-Groups

Other on-going progress in this project involves modification of the R groups. Recently Dr. Aaron Mailman prepared a new radical (**5-12**) with R = F, which crystallized in the side-centered orthorhombic space group $Cmc2_1$ with four molecules per unit cell (Figure 5.2). According to the preliminary transport studies, its room temperature conductivity reaches 0.03 S/cm, which is the highest room temperature conductivity of sulfur-nitrogen based radicals known to date. From the magnetic data, this alternating π-stacked material behaves as antiferromagnetic coupled paramagnets over the range 100-300 K, which goes under a phase transition to spin-canted antiferromagnetically ordered state at 15

K. Under the ordering temperature the spin-canting angle (ϕ) is estimated to be 0.15°. Further magnetic studies (*i.e.*, neutron diffraction) are required to fully understand the magnetic structure of this material.

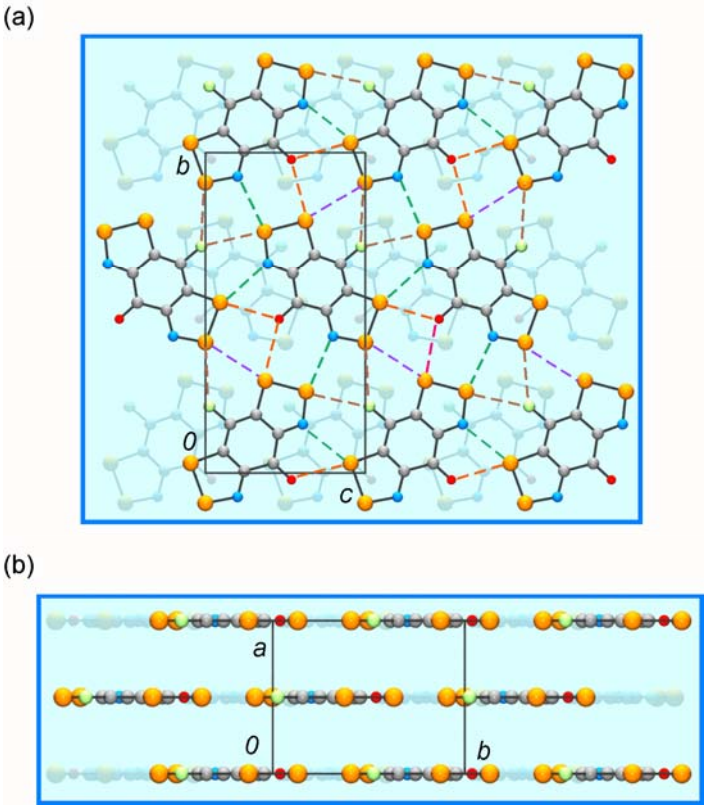

Figure 5.2. The unit cell of **5-12**, R = F viewed parallel to (a) the *a*-axis and (b) the *c*-axis. In (a) the layer at $x = 0.5$ is shaded, while in (b) the layer with $z > 0.5$ is shaded. The dashed lines represent the lateral intermolecular S···S′ (purple), S···O′ (orange), S···N′ (green) S···F′ (brown) contacts.

5.3 Future Work

In general, the crystallography and CV results presented in this thesis (See Chapter 2 and 3) have shown that the R group can have a dramatic effect on the crystal packing (*i.e.*, space group, π-stacks) and allows for 2D interactions, but has only a small influence on the solution cell potentials. The R group therefore could be modified, which could potentially change the bandwidth, even though the onsite Coulomb repulsion energy does not vary significantly and they may also exhibit interesting magnetic properties. In the case of the pyridine based systems, there are two beltline ligands (*i.e.*, R_1

and R_2 for **5-3**) which allow a wide range of different compounds to be prepared. However, in the semiquinone based system, replacing one of the beltline ligand with a carbonyl group has limited the possible variations which this framework can support however the intermolecular S···O′, and S···N′ interactions are the key to build the 2D architectures of the semiquinone-bridged systems.

The application of physical pressure, on the pyridine based systems has shown significantly enhanced conductivity[7,9] and magnetic ordering.[10] Therefore the high pressure powder crystallography, conductivity and magnetic measurements are of potential interest for compounds **5-12**, since the pressure and hence improved the overlap between the SOMO orbitals may lead to enhanced conductivity and increase the magnetic ordering temperature. Alternatively a phase change may be observed, which would lead to changes in its conductivity and magnetic properties.

Appendix A

Procedures and Techniques

A.1 Procedures

A.1.1 General Procedures

Due to the instability of reactants and/or products towards moisture, many reactions were performed under an inert atmosphere of nitrogen. Those reactions were carried out in solutions by standard or modified Schlenk techniques using a double-manifold glass vacuum line (nitrogen / vacuum) with an Edwards E2M series rotary vacuum pump. Air sensitive solids were handled and stored in a nitrogen-filled Braun MB-150 dry box.

A.1.2 Diffusion H-cell Crystallizations

For the highly insoluble and thermally unstable radicals, *i.e.* recrystallization and sublimation are not viable options for crystal growth; H-cell techniques are employed to grow analytical grade crystals. A typical H-cell apparatus is illustrated in Figure A.1 and the general experimental procedure is as follows; two solutions of each reactant are placed in each of the round bottom flasks and attached to the H-cell. Four freeze-pump-thaw cycles were performed to ensure all the oxygen has been removed from the solutions. Under the vacuum, the H-cell is inverted and tipped slightly to allow two solutions to mix slowly. As one solution diffuses through the glass frit into the other, the crystals of the product grow at the interface of the two solutions.

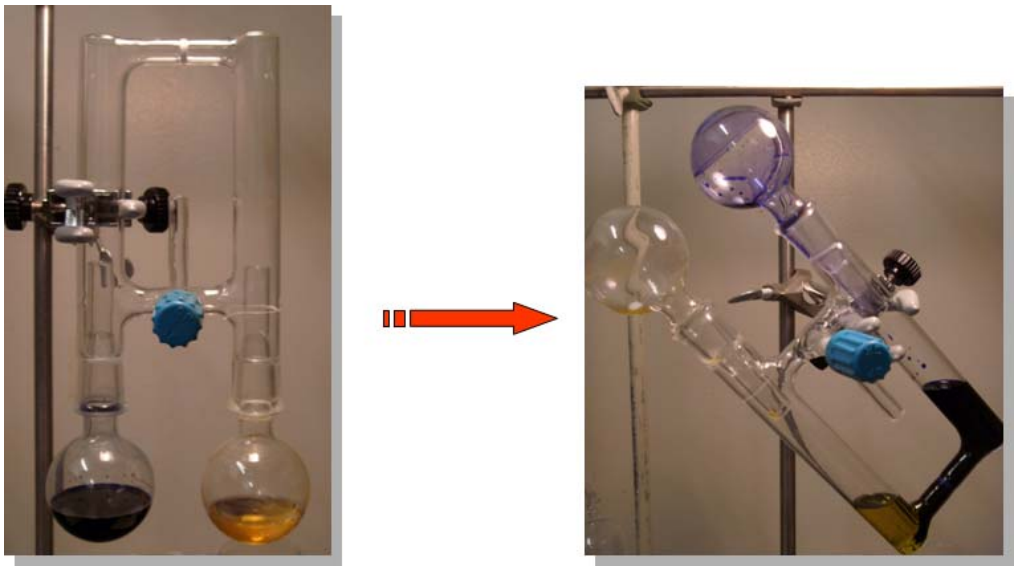

Figure A.1: Diffusion H-cell apparatus for single crystal growth.

A.2 Techniques

A.2.1 NMR Spectroscopy

^{1}H NMR spectra were collected on a Bruker Avance 300 MHz NMR spectrometer.

A.2.2 Infrared Spectroscopy

Infrared spectra were recorded at 2 cm^{-1} resolution as Nujol mulls on KBr plates, on a Nicolet Avatar 320 FT infrared spectrometer.

A.2.3 Mass Spectrometry

Low resolution mass spectra recorded at the WATSPEC Mass Spectrometry Facility.

A.2.4 Cyclic Voltammery

Solution cyclic voltammery experiments were performed in dry acetonitrile using PINE Bipotentiostat, model AFCCIBPI with scan rates between 50 and 100 mV s^{-1}. Potentials were scanned from -2.5 to 2.0 V with respect to the quasi-reference electrode in a single compartment cell fitted with Pt electrode. The potentials were referenced to the ferrocenium / ferrocene couple at 0.38 V *vs.* SCE.

A.2.5 UV-Visible Spectroscopy

UV-visible spectra were collected on a PerkinElmer Lambda 35 UV-visible spectrometer, in acetonitrile (anhydrous).

A.2.6 EPR Spectroscopy

The X-band EPR spectra of the radicals were recorded in dichloromethane or toluene solutions at ambient temperature using a Bruker EMX spectrometer. Hyperfine coupling constants were obtained by simulation using Simfonia and WinSim.

A.2.7 Elemental Analysis

Elemental analyses were performed by MHW Laboratories, Phoenix, AZ, USA.

A.2.8 Magnetic Susceptibility Measurements

DC magnetic susceptibility measurements were performed over the range 2 - 300 K on a Quantum Design MPMS SQUID magnetometer operating at H = 1000 Oe at Brockhouse Institute for Materials Research, McMaster University. Diamagnetic corrections were made using Pascal's constants.[1]

A.2.9 Conductivity Measurements

Four-probe temperature dependent conductivity measurements on cold pressed pellets were performed over the range 140-300 K using an Oxford Instruments MagLab EXA system. Silver paint (Leitsilber 200) was used to apply the electrical contacts. The system was cooled by a Lake Shore 330 controller and a Keithley 2400 unit was used as the voltage source and current meter. The pellet was prepared by a Weber Pressen (5 mm × 1 mm × 1 mm) pressing tool under 4 kN force (0.8 GPa).

A.2.10 Density Functional Theory (DFT) Calculations

All DFT calculations were performed with the Gaussian 09W suite of programs,[2] using the (U)B3LYP hybrid functional and polarized, split-valence basis sets with double-zeta (6-31G(d,p)) functions.

A.2.11 Band Structure Calculations

EHT Band electronic structure calculations were performed with the Caesar suite of programs[3] using the Coulomb parameters of Baasch, Viste and Gray[4] and a quasi-split valence basis set adapted from Clementi and Roetti.[5] The off-diagonal elements of the Hamiltonian matrix were calculated with

the standard weighting formula.[6] Atomic positions were taken from crystallographic data. In the case of **4-1b**·MeCN, the acetonitrile molecules were not included in the calculation.

A.3 Source of Starting Materials

A.3.1 Purchased Chemicals that were Used as Received

1,2-dichloroethane	Caledon
4-bromophenol	Alfa Aesar
4-chlorophenol	Alfa Aesar
4-ethylphenol	Aldrich / Alfa Aesar
4-methyl-2,6-dinitrophenol	Aldrich
4-phenylphenol	Alfa Aesar
acetic acid, glacial	Fisher
ammonia gas	Praxair
carbon disulfide	Aldrich
chloroform-d	Cambridge Isotope
decamethylferrocene	Aldrich
dichloromethane	Caledon
diethyl ether	EMD
dimethylferrocene	Strem Chemicals
dimethylsulfoxide-d	CDN Isotope
ethanol-95 %	Fisher
gallium (III) trichloride, anhydrous, beads, -10 mesh, 99.99 %	Aldrich
hydrochloric acid, 36 %	Fisher
nitric acid, 68 %	Fisher

nitrogen gas	In-house supply
nitrosonium hexafluoroantiminate	SynQuest
nitrosonium tetrafluoroborate	SynQuest
octamethylferrocene	Aldrich
silver trifluoromethanesulfonate	SynQuest
sulfuric acid, 98 %	Fisher
sulfur monochloride	Aldrich
tetra-*n*-butylammonium bromide	Aldrich
tetra-*n*-butylammonium chloride	Aldrich
tin (II) chloride dihydrate, 98 %	Alfa Aesar
tin powder, 100 mesh, 99.5 % (metals basis)	Alfa Aesar
triethylamine, 99 %	EMD

A.3.2 Solvent Purified Prior to Use

acetonitrile (Caledon)	distilled from P_2O_5 and CaH_2
propionitrile (Fluka / Alfa Aesar)	distilled from P_2O_5 and CaH_2 after purification
chloroform (Caledon)	distilled from $CaCl_2$

Purification of propionitrile.[7] Propionitrile (1 L) was stirred with 20 % HCl (200 mL) for 1 h, washed by water and neutralized with K_2CO_3. After the organic phase was collected and dried over molecular sieves and CaH_2, propionitrile was distilled from P_2O_5 and CaH_2.

A.3.3 Chemicals Prepared "In-House"

Preparation of Ag_2O.[8] KOH pallets were added to a solution of an aqueous solution of silver nitrate ($AgNO_3$) until the solution pH reaches ~ 12. The product was precipitated out of solution as black powder, which was collected by filtration and dried in air.

Preparation of iodobenzene dichloride.[9] In the dark, a solution of 1.5 mL (2.75 g, 13.5 mmol) of iodobenzene in 15 mL dichloromethane was cooled to 0 °C and Cl_2 gas was passed over for 20 min to give bright yellow precipitate. The solid was isolated by filtration, washed with cold dichloromethane and dried *in vacuo* to yield 3.40 g (12.4 mmol, 92 % yield) of iodobenzene dichloride.

References for Chapter 1

1. Hicks, R. G. *Stable Radicals: Fundamentals and Applied Aspects of Odd-Electron Compounds*; John Wiley & Sons, Ltd.: Wiltshire, 2010

2. McMurry, J. *Organic Chemistry*; 5th ed.; Brooks/ Cole Thomson Learning: New York, 2000.

3. Power, P. P. *Chem. Rev.* **2003**, *103*, 789.

4. Griller, D.; Ingold, K. U. *Acc. Chem. Res.* **1976**, *9*, 13.

5. Gomberg, M. J. *J. Am. Chem. Soc.* **1900**, *22*, 757.

6. Krause, E.; Polack, H. *Ber. Dtsch. Chem. Ges.* **1926**, *59*, 777.

7. Hudson, A.; Lappert, M. F.; Lednor, P. W. *J. Chem. Soc., Dalton Trans.* **1976**, 2369.

8. Gynane, M. J. S.; Hudson, A.; Lappert, M. F.; Power, P. P.; Goldwhite, H. *Chem. Commun.* **1976**, 623.

9. Berliner, L. J. *Spin Labeling: Theory and Applications*; Academic Press: New York, 1976; Vol. 1.

10. Borbat, P. P.; Costa-Filho, A. J.; Earle, K. A.; Moscicki, J. K.; Freed, J. H. *Science* **2001**, *291*, 1619.

11. Hawker, C. J.; Bosman, A. W.; Harth, E. *Chem. Rev.* **2001**, *101*, 3661.

12. (a) Sadadibara, T.; Miyazaki, Y.; Ishida, T.; Nogami, T.; Sorai, M. *J. Phys. Chem. B* **2002**, *106*, 6390; (b) Mito, M.; Deguchi, H.; Tanimoto, T.; Kawae, H.; Nakatsuji, S.; Morimoto, H.; Anzai, H.; Makao, H.; Murakami, Y.; Takea, K. *Phys. Rev. B* **2003**, *67*, 024427.

13. (a) Haddon, R. C. *Nature* **1975**, *256*, 394; (b) Cordes, A. W.; Haddon, R. C.; Oakley, R. T. *Phosphorus, Sulfur, Silicon and Related Elements* **2004**, *179*, 673.

14. (a) Ikuma, N.; Tamura, R.; Shimono, S.; Kawame, N.; Tamada, O.; Sakai, N.; Yamauchi, J.; Yamamoto, Y. *Angew. Chem. Int. Ed. Engl.* **2004**, *43*, 3677; (b) Zienkiewicz, J.; Kaszynski, P.; Young, V. G. *J. Org. Chem* **2004**, *69*, 2551.

15. (a) Kahn, O.; Martinex, C. J. *Science* **1998**, *279*, 44; (b) Itkis, M. E.; Chi, X.; Cordes, A. W.; Haddon, R. C. *Science* **2002**, *296*, 1443.

16. (a) Hicks, R. G.; Koivisto, B. D.; Lemaire, M. T. *Org. Lett* **2004**, *6*, 1887; (b) Hearns, N. G. R.; Preuss, K. E.; Richardson, J. F.; Bin-Salamon, S. *J. Am. Chem. Soc.* **2004**, *126*, 9942.

17. (a) Cordes, A. W.; Haddon, R. C.; Oakley, R. T. In *The Chemistry of Inorganic Ring Systems*; Steudel, R., Ed.; Elsevier Science: Amsterdam, 1992; (b) Cordes, A. W.; Haddon, R. C.; Oakley, R. T. *Adv. Mater.* **1994**, *6*, 798; (c) Oakley, R. T. *Canadian Chemical News* **1992**, *44*, 21.

18. Rozantsev, E. G.; Sholle, V. D. *Synthesis* **1971**, 190.

19. Osiecki, J. H.; Ullamn, E. F. *J. Am. Chem. Soc.* **1968**, *90*, 1078.

20. Kuhn, R.; Trischmann, H. *Monatsh. Chem.* **1964**, *95*, 457.

21. Robertson, C. M.; Leitch, A. A.; Cvrkalj, K.; Myles, D. J. T.; Reed, R. W.; Dube, P. A.; Oakley, R. T. *J. Am. Chem. Soc.* **2008**, *130*, 14791.

22. Robertson, C. M.; Leitch, A. A.; Cvrkalj, K.; Reed, R. W.; Myles, D. J. T.; Dube, P. A.; Oakley, R. T. *J. Am. Chem. Soc.* **2008**, *130*, 8414.

23. Hoffmann, R. *Solids and Surfaces: A Chemist's View of Bonding in Extended Structures*; VCH New York, 1988.

24. Kittel, C. *Introduction to Solid State Physics, 5th Ed.*; John Wiley & Sons, Inc.: New York, 1976.

25. Mott, N. F. *Metal-insulator Transitions*; Taylor and Francis: London, 1990.

26. Whangbo, M.-H. *J. Chem. Phys.* **1979**, *70*, 4963.

27. Torrance, J. B. *Acc. Chem. Res.* **1979**, *12*, 79.

28. Melby, L. R.; Harder, R. J.; Hertler, W. R.; Mahler, W.; Benson, R. E.; Mochel, W. E. *J. Am. Chem. Soc.* **1962**, *84*, 3374.

29. (a) Herbstein, F. H. In *Perspectives in Structural Chemistry*; Dunitz, J. D., Ibers, J. A., Eds.; Wiley: New York, 1971; Vol. IV, p 166; (b) Soos, Z. G. *Annu. Rev. Phys. Chem.* **1976**, *25*, 121; (c) Andre, J. J.; Bieber, A.; Gautier, F. *Ann. Phys* **1976**, 145; (d) Shchegolev, I. F. *Phys. Status Soloiso A* **1972**, *12*, 9; (e) Shibaeva, R. P.; Atomyan, L. O. *J. Struct. Chem.* **1972**, *13*, 514; (f) Dahm, F. J.; Horn, P.; Johnson, G. R.; Miles, M. G.; Wilson, J. D. *J. Cryst. Mol. Struct.* **1975**, *5*, 27.

30. Wudl, F.; Wobschall, D.; Hufnagel, E. J. *J. Am. Chem. Soc.* **1972**, *94*, 670.

31. (a) Ferraris, J.; Cowan, D. O.; Walatka, V.; Jr.; Perlstein, J. H. *J. Am. Chem. Soc.* **1972**, *95*, 948; (b) Coleman, L. B.; Chohen, M. J.; Sandman, D. J.; Yamagishi, F. G.; Gratio, A. F.; Heeger, A. J. *Solid State Commun.* **1973**, *12*, 1125.

32. Belluz, P. D. B.; Cordes, A. W.; Kristof, E. M.; Kristof, P. V.; Liblong, S. W.; Oakley, R. T. *J. Am. Chem. Soc.* **1989**, *111*, 9276.

33. Boeré, R. T.; Moock, K. H. *J. Am. Chem. Soc.* **1995**, *117*, 4755.

34. (a) Bryan, C. D.; Cordes, A. W.; Haddon, R. C.; Hicks, R. G.; Kennepohl, D. K.; MacKinnin, C. D.; Oakley, R. T.; Palstra, T. T. M.; Perel, A. S.; Scott, S. R.; Schneemeyer, L. G.; Waszczak, J. V. *J. Am. Chem. Soc.* **1994**, *116*, 1205; (b) Bryan, C. D.; Cordes, A. W.; Fleming, R. M.; George, N. A.; Glarum, S. H.; Haddon, R. C.; MacKinnin, C. D.; Oakley, R. T.; Palstra, T. T. M.; Perel, A. S.; Schneemeyer, L. G.; Waszczak, J. V. *J. Am. Chem. Soc.* **1995**, *117*, 6880; (c) Bryan, C. D.; Klapstein, D.; Haddon, R. C.; Kennepohl, D. K.; Oakley, R. T.; Goddard, J. D. *Inorg. Chem.* **1996**, *35*, 7626.

35. Rawson, J. M.; Aberola, A.; Whalley, A. J. *J. Mater. Chem.* **2006**, *16*, 2560.

36. Nyburg, S. C.; Faerman, C. H. *Acta Crystallogr., Sect. B: Struct. Sci.* **1985**, *B41*, 274.

37. Banister, A. J.; Lavender, I.; Rawson, J. M. *Adv. Heterocycl. Chem.* **1995**, *62*, 137.

38. (a) Barclay, T. M.; Beer, L.; Cordes, A. W.; Oakley, R. T.; Preuss, K. E.; Taylor, N. J.; Reed, R. W. *Chem. Commun.* **1999**, 531; (b) Oakley, R. T.; Reed, R. W.; Robertson, C. M.; Richardson, J. F. *Inorg. Chem.* **2005**, *44*, 1837.

39. Beer, L.; Brusso, J. L.; Cordes, A. W.; Haddon, R. C.; Itkis, M. E.; Kirschbaum, K.; MacGregor, D. S.; Oakley, R. T.; Pinkerton, A. A.; Reed, R. W. *J. Am. Chem. Soc.* **2002**, *124*, 9498.

40. Leitch, A. A.; McKenzie, C. E.; Oakley, R. T.; Reed, R. W.; Richardson, J. F.; Sawyer, L. D. *Chem. Commun.* **2006**, 1088.

41. Leitch, A. A.; Reed, R. W.; Robertson, C. M.; Britten, J. F.; Yu, X.; Secco, R. A.; Oakley, R. T. *J. Am. Chem. Soc.* **2007**, *129*, 7903.

42. (a) Beer, L.; Brusso, J. L.; Haddon, R. C.; Itkis, M. E.; Kleinke, H.; Leitch, A. A.; Oakley, R. T.; Reed, R. W.; Richardson, J. F.; Secco, R. A.; Yu, X. *J. Am. Chem. Soc.* **2005**, *127*, 18159; (b) Risto, M.; Asspid, A.; Winter, S. W.; Oilunkaniemi, R.; Laitinen, R. S.; Oakley, R. T. *Inorg. Chem.* **2008**, *47*, 10100.

43. (a) Beer, L.; Brusso, J. L.; Haddon, R. C.; Itkis, M. E.; Oakley, R. T.; Reed, R. W.; Richardson, J. F.; Secco, R. A.; Yu, X. *Chem. Commun.* **2005**, 5745; (b) Brusso, J. L.; Cvrkalj, K.; Leitch, A. A.; Oakley, R. T.; Reed, R. W.; Robertson, C. M. *J. Am. Chem. Soc.* **2006**, *128*, 15080.

44. Coey, J. M. D. *Magnetism and Magnetic Materials*; Cambridge University Press: New York, 2010.

45. Jiles, D. *Introduction to Magnetism and Magnetic Material, 2nd Ed.*; Chapman and Hall: London, 1998.

46. Brokate, M.; Sprekels, J. *Hysteresis and Phase Transitions*; Springer: New York, 1996.

47. Kollmar, C.; Kahn, O. *Acc. Chem. Res.* **1993**, *26*, 259.

48. (a) Chiarelli, R.; Novak, M. A.; Rassat, A.; Tholence, J. L. *Nature* **1993**, *363*, 147; (b) Nakazawa, Y.; Tamura, M.; Shirakawa, N.; Shiomi, D.; Takahashi, M.; Kinoshita, M. *Phys. Rev. B* **1992**, *46*, 8906; (c) Koivisto, B. D.; Hicks, R. G. *Coord. Chem. Rev.* **2005**, *249*, 2612.

49. Mito, M.; Nakano, H.; Kawae, T.; Hitaka, M.; Takagi, S.; Deguchi, H.; Suzuki, K.; Mukai, K.; Takeda, K. *J. Phys. Soc. Jpn.* **1997**, *66*, 2147.

50. Banister, A. J.; Bricklebank, N.; Lavender, I.; Rawson, J. M.; Gregory, C. I.; Tanner, B. K.; Clegg, W.; Elsegood, M. R. J.; Palacio, F. *Angew. Chem. Int. Ed. Engl.* **1996**, *35*, 2533.

51. Alberola, A.; Less, R.; Pask, C. M.; Rawson, J. M.; Palacio, F.; Oliete, P.; Paulsen, C.; Yamagushi, A.; Farley, R. D.; Murphy, D. M. *Angew. Chem. Int. Ed.* **2003**, *42*, 4782.

52. Winter, S. W.; Cvrkalj, K.; Robertson, C. M.; Probert, M. R.; Dube, P. A.; Howard, J. A. K.; Oakley, R. T. *Chem. Commun.* **2009**, 7306.

53. Leitch, A. A.; Brusso, J. L.; Cvrkalj, K.; Reed, R. W.; Robertson, C. M.; Dube, P. A.; Oakley, R. T. *Chem. Commun.* **2007**, 3368.

54. Robertson, C. M.; Myles, D. J. T.; Leitch, A. A.; Reed, R. W.; Dooley, B. M.; Frank, N. L.; Dube, P. A.; Thompson, L. K.; Oakley, R. T. *J. Am. Chem. Soc.* **2007**, *129*, 12688.

55. Mito, M.; Komorida, Y.; Tsuruda, H.; Tse, J. S.; Desgreniers, S.; Ohishi, Y.; Leitch, A. A.; Cvrkalj, K.; Robertson, C. M.; Oakley, R. T. *J. Am. Chem. Soc.* **2009**, *131*, 16012.

56. (a) Decken, A.; Mailman, A.; Mattar, S. M.; Passmore, J. *Chem. Commun.* **2005**, 2366; (b) Dechen, A.; Mailman, A. M.; Passmore, J. *Chem. Commun.* **2009**, 6077.

References for Chapter 2

1. Mayer, R.; Domschke, G.; Bleisch, S.; Bartl, A. *Z.Chem.* **1981**, *21*, 324.

2. Preston, K. F.; Sutcliffe, L. H. *Mag. Res. Chem.* **1990**, *28*, 189.

3. Herz, R. *Chem. Zent.* **1922**, *4*, 948.

4. Appel, R.; Janssen, H.; Siray, M.; Knoch, F. *Chemische Berichte* **1985**, *118*, 1632.

5. Barclay, T. M.; Beer, L.; Cordes, A. W.; Oakley, R. T.; Preuss, K. E.; Taylor, N. J.; Reed, R. W. *Chem. Commun.* **1999**, 531.

6. (a) Beer, L.; Brusso, J. L.; Cordes, A. W.; Haddon, R. C.; Itkis, M. E.; Kirschbaum, K.; MacGregor, D. S.; Oakley, R. T.; Pinkerton, A. A.; Reed, R. W. *J. Am. Chem. Soc.* **2002**, *124*, 9498; (b) Beer, L.; Britten, J. F.; Brusso, J. L.; Cordes, A. W.; Haddon, R. C.; Itkis, M. E.; MacGregor, D. S.; Oakley, R. T.; Reed, R. W.; Robertson, C. M. *J. Am. Chem. Soc.* **2003**, *125*, 14394; (c) Beer, L.; Britten, J. F.; Clements, O. P.; Haddon, R. C.; Itkis, M. E.; Matkovitch, K. M.; Oakley, R. T.; Reed, R. W. *Chem. Mater.* **2004**, *16*, 1564.

7. Robertson, C. M.; Leitch, A. A.; Cvrkalj, K.; Myles, D. J. T.; Reed, R. W.; Dube, P. A.; Oakley, R. T. *J. Am. Chem. Soc.* **2008**, *130*, 14791.

8. Decken, A.; Mailman, A. M.; Mattar, S. M.; Passmore, J. *Chem. Commun.* **2005**.

9. Mailman, A. Ph.D. Thesis, University of New Brunswick, 2011.

10. Kanamori, D.; Yamada, Y.; Onoda, A.; Okamura, T.-a.; Adachi, S.; Yamamoto, H.; Ueyama, N. *Inorg. Chim. Acta* **2005**, *358*, 331.

11. Olah, G. A.; Malhotra, R.; Narang, S. C. *Nitration: Methods and Mechanism*; VCH: New York, 1989.

12. Schofield, K. *Aromatic Nitrations*; Cambridge University Press: Cambridge, 1980.

13. Ono, N. In *Organic Nitro Chemistry Series*; Feuer, H., Ed.; A John Wiley & Sons, Inc., Publication: New York, 2001.

14. (a) Iranpoor, N.; Firouzabadi, H.; Heydari, R. *Phosphorus, Sulfur, Silicon and Related Elements* **2003**, *178*, 1027; (b) Zolfigol, M. A.; Madrakian, E.; Ghaemi, E.; Niknam, K. *Synth. Commun.* **2008**, *38*, 3366; (c) Iranpoora, N.; Firouzabadia, H.; AliZolfigolb, M. *Synth. Commun.* **1998**, *28*, 2773.

15. Clewley, R. G.; Cross, G. G.; Fischer, A.; Henderson, G. N. *Tetrahedron* **1989**, *45*, 1299.

16. Smith, C. J.; Ali, A.; Chen, L.; Hammond, M. L.; Anderson, M. S.; Chen, Y.; Eveland, S. S.; Guo, Q.; Hyland, S. A.; Milot, D. P.; Sparrow, C. P.; Wright, S. D.; Sinclair, P. J. *Bioorganic & Medicinal Chemiestry Letters* **2010**, *20*, 346.

17. Zolfigol, M. A. *Molecules* **2002**, *7*, 734.

18. van Erp, H. *Harlem. Rec. Trav. Chim.* **1910**, *29*, 187.

19. Tullos, G. L.; Powers, J. N.; Jeskey, S. J.; Mathias, L. J. *Macromolecules* **1999**, *32*, 3598.

20. Dutton, G. G. S.; Briggs, T. I.; Brown, B. R.; Powell, R. K. *Can. J. Chem.* **1953**, *31*, 837.

21. (a) Liu, K. G.; Lo, J. R.; Comery, T. A.; Zhang, G. M.; Zhang, J. Y.; Kowal, D. M.; Smith, D. L.; Di, L.; Kerns, E. H.; Schechter, L. E.; Robichaud, A. J. *Bioorg. Med. Chem. Lett.* **2009**, *19*, 1115; (b) Chen, B. K.; Tsai, Y. J.; Tsay, S. Y. *Polym. Int.* **2006**, *55*, 93.

22. Raju, B.; Ragul, R.; Sivasankar, B. N. *Indian J. Chem. Sect B-Org. Chem. Incl. Med. Chem.* **2009**, *48*, 1315.

23. Kanth, S. R.; Reddy, G. V.; Rao, V.; Maitraie, D.; Narsaiah, B.; Rao, P. S. *Synth. Commun.* **2002**, *32*, 2849.

24. Tyagi, Y. K.; Kumar, A.; Raj, H. G.; Vohra, P.; Gupta, G.; Kumari, R.; Kumar, P.; Gupta, R. *E. J. Med. Chem.* **2005**, *40*, 413.

25. (a) Tu, C.; Meng, C.; Ho, Y. *Acta Chim. Sinica* **1956**, *22*, 134; (b) Tingle, J. B.; Williams, L. F. *Am. Chem. J.* **1907**, *37*, 51; (c) Gamble, A. B.; Garner, J.; Gordon, C. P.; O'Conner, S. M. J.; Keller, P. A. *Synth. Commun.* **2007**, *37*, 2777; (d) Fromm, E.; Ebert, R. *J. Prakt. Chem.* **1924**, *108*, 75.

26. *Ammonium Chloride*; Science Lab: Houston, Texas, Nov. 1, 2010. http://www.sciencelab.com/xMSDS-Ammonium_chloride-9927431 (accessed 4/18/2011).

27. Warburton, W. K. *Chem. Rev.* **1957**, *57*, 1011.

28. Leitch, A. A.; Oakley, R. T.; Reed, R. W.; Thompson, L. K. *Inorg. Chem.* **2007**, *46*, 6261.

29. Aherne, C. M.; Banister, A. J.; Hibbert, T. G.; Luke, A. W.; Rawson, J. M. *Polyhedron* **1997**, *16*, 4239.

30. Boeré, R. T.; Roemmele, T. L.; Yu, X. *Inorg. Chem.* **2011**, *50*, 5123.

31. Rakitin, O. A. *ARKIVOC* **2009** *i*, 129.

32. Huheey, J. E.; Keiter, E. A.; Keiter, R. L. *Inorganic Chemistry: Principles of Structure and Reactivity, 4th Ed.*; Harper Collins College Publishers: New York, 1993.

33. Lehman, P. A. F.; Mceach, D. M. B. *J. Mol. Structure* **1971**, *7*, 253.

34. Rawson, J. M.; McManus, G. D. *Coord. Chem. Rev.* **1999**, *189*, 135.

35. Beer, L.; Brusso, J. L.; Cordes, A. W.; Haddon, R. C.; Itkis, M. E.; Krischbaum, K.; MacGregor, D. S.; Oakley, R. T.; Pinkerton, A. A.; Reed, R. W. *J. Am. Chem. Soc.* **2002**, *124*, 9498.

36. (a) Zou, C.; Wrighton, M. S. *J. Am. Chem. Soc.* **1990**, *112*, 7578; (b) Hobi, M.; Ruppert, O.; Gramlich, V.; Togni, A. *Organometallics* **1997**, *16*, 1384.

37. (a) Hoh, G. L. K.; McEwen, W. E.; Kleinberg, J. *J. Am. Chem. Soc.* **1961**, *83*, 3949; (b) Lemione, P.; Gross, M.; Braunstein, P.; Mathey, F.; Deschamps, B.; Nelson, H. H. *Organometallics* **1984**, *3*, 1301.

38. Noviandri, I.; Brown, K. N.; Flemming, D. S.; Gulyas, P. T.; Lay, P. A.; Masters, A. F.; Phillips, L. *J. Phys. Chem. B* **1999**, *103*, 6713.

39. Pavia, D. L.; Lampman, G. M.; Kriz, G. S. *Introduction to Spectrocopy, 3rd Ed.*; Thomson Learnning Inc.: Toronto, 2001.

40. Zolfigol, M. A.; Madrakian, E.; Ghaemi, E. *Synlett* **2003**, *14*, 2222.

41. Cai, L.; Xie, W.; Mahmoud, H.; Han, Y.; Wink, D. J.; Li, S.; O'Connor, C. *J. Inorg. Chim. Acta* **1997**, *263*, 231.

References for Chapter 3

1. Winter, S. M.; Roberts, R. J.; Mailman, A.; Cvrkalj, K.; Assoud, A.; Oakley, R. T. *Chem. Commun.* **2010**, *46*, 4496.

2. Decken, A.; Mailman, A.; Passmore, J.; Rautiainen, J. M.; Scherer, W.; Scheidt, E. W. *Dalton Trans.* **2011**, *40*, 868.

3. (a) Bondi, A. J. *A. J. Phys. Chem.* **1964**, *68*, 441; (b) Dance, I. *New. J. Chem.* **2003**, *27*, 22.

4. Laves, F.; Baskin, Y. Z. *Kristallogr. Kristallgeom. Kristallphys. Kristallchem.* **1956**, *107*, 337.

5. Beer, L.; Brusso, J. L.; Cordes, A. W.; Haddon, R. C.; Itkis, M. E.; Kirschbaum, K.; MacGregor, D. S.; Oakley, R. T.; Pinkerton, A. A.; Reed, R. W. *J. Am. Chem. Soc.* **2002**, *124*, 9498.

6. *SAINT*, Version 6.22; Bruker Advanced X-ray Solutions, Inc.: Madison, WI, 2001.

7. Sheldrick, G. M.; SHELXS-90. *Acta Crystallogr. A* **1990**, *46*, 467.

8. Sheldrick, G. M. *SHELXL-97*; Program for the Refinement of Crystal Structures, University of Gottingen: Gottingen, Germany, 1997.

9. *SHELXTL*, Version 6.12; Program Library for Structure Solution and Molecular Graphics, Bruker Advanced X-ray Solutions, Inc.: Madison, WI, 2001.

10. *Proteum2*, Version 2010.1-2; Bruker-AXS Inc.: Karlsruhe, Germany.

11. Dolomanov, O. V.; Bourhis, L. J.; Gildea, R. J.; Howard, J. A. K.; Puschmann, H. *J. Appl. Crystallogr.* **2009**, *42*, 339.

12. Rietveld, H. M. *J. Appl. Crystallogr.* **1964**, *2*, 65.

References for Chapter 4

1. Beer, L.; Brusso, J. L.; Cordes, A. W.; Haddon, R. C.; Itkis, M. E.; Kirschbaum, K.; MacGregor, D. S.; Oakley, R. T.; Pinkerton, A. A.; Reed, R. W. *J. Am. Chem. Soc.* **2002**, *124*, 9498.

2. Leitch, A. A.; Reed, R. W.; Robertson, C. M.; Britten, J. F.; Yu, X.; Secco, R. A.; Oakley, R. T. *J. Am. Chem. Soc.* **2007**, *129*, 7903.

3. Leitch, A. A.; Yu, X.; Winter, S. M.; Secco, R. A.; Dube, P. A.; Oakley, R. T. *J. Am. Chem. Soc.* **2009**, *131*, 7112.

4. Carlin, T. L. *Magnetochenistry*; Springer-Verlag: New York, 1986.

5. Bonner, J. C.; Fisher, M. E. *Phys. Rev. A.* **1964**, *135*, 640.

6. (a) Novoa, J. J.; Deumal, M. *Struct. Bonding* **2001**, *100*, 33; (b) Jornet, J.; Deumal, M.; Ribas-Ariño, J.; Bearpark, M. J.; Robb, M. A.; Hicks, R. G.; Novoa, J. J. *Chem. Eur. J.* **2006**, *12*, 3995.

7. (a) Rawson, J. M.; Luzon, J.; Palacio, F. *Coord. Chem. Rev.* **2005**, *249*, 2631; (b) Luzon, J.; Campo, J.; Palacio, F.; McIntyre, G. J.; Rawson, J. M. *Polyhedron* **2005**, *24*, 2579; (c) Deumal, M.; LeRoux, S.; Rawson, J. M.; Robb, M. A.; Novoa, J. J. *Polyhedron* **2007**, *26*, 1949; (d) Decken, A.; Mattar, S. M.; Passmore, J.; Shuvaev, K. V.; Thompson, L. K. *Inorg. Chem.* **2006**, *45*, 3878; (e) Leitch, A. A.; Oakley, R. T.; Reed, R. W.; Thompson, L. K. *Inorg. Chem.* **2007**, *46*, 6261; (f) Winter, S. W.; Cvrkalj, K.; Robertson, C. M.; Probert, M. R.; Dube, P. A.; Howard, J. A. K.; Oakley, R. T. *Chem. Commun.* **2009**, 7306.

8. Takano, Y.; Taniguchi, T.; Isobe, H.; Kubo, T.; Morita, Y.; Yamamoto, K.; Nakasuji, K.; Takui, T.; Yamaguchi, K. *J. Am. Chem. Soc.* **2002**, *124*, 11122.

9. (a) Noodleman, L.; Norman, J. G. *J. Chem. Phys.* **1979**, *70*, 4903; (b) Noodleman, L. *J. Chem. Phys.* **1981**, *74*, 5737; (c) Takano, Y.; Taniguchi, T.; Isobe, H.; Kubo, T.; Morita, Y.; Yamamoto, K.; Nakasuji, K.; Takui, T.; Yamaguchi, K. *Chem. Phys. Lett.* **2002**, *368*, 17; (d) *Self-Consistent Field Theory and Applications*; Yamaguchi, K., Ed.; Elsevier: Amsterdam, 1990; (e) Deumal, M.; Robb, M. A.; Novoa, J. J. *Prog. Theor. Chem. Phys.* **2007**, *16*, 271.

10. Cordes, A. W.; Haddon, R. C.; Hicks, R. G.; Oakley, R. T.; Palstra, T. T. M. *Inorg. Chem.* **1992**, *31*, 1802.

11. Gillespie, R. J.; Ireland, R.; Vekris, J. E. *Can. J. Chem.* **1975**, *53*, 3147.

12. Clarke, C. S.; Jornet-Somoza, J.; Mota, F.; Novoa, J. J.; Deumal, M. *J. Am. Chem. Soc.* **2010**, *132*, 17817.

13. (a) Small, R. W. H.; Banister, A. J.; Hauptman, Z. V. *J. Chem. Soc., Dalton Trans.* **1984**, 1377; (b) Gimarc, B. M.; Trinajstić, N. *Pure and Appl. Chem.* **1980**, *52*, 1443; (c) Gimarc, B. M. *Pure and Appl. Chem.* **1990**, *62*, 423.

14. Baker, G. A.; Rushbrooke, G. S.; Gilbert, H. E. *Phys. Rev.* **1964**, *135*, 186.

15. Murata, H.; Miyazaki, Y.; Inaba, A.; Paduan-Fiho, A.; Bindilatti, V.; Oliveira, N. F.; Delen, Z.; Lahti, P. M. *J. Am. Chem. Soc.* **2008**, *130*, 186.

16. (a) Kahn, O. *Molecular Magnetism*; VCH: New York, 1993; (b) Das, A.; Rosair, G. M.; S.El-Fallah, M.; Ribas, J.; Mitra, S. *Inorg. Chem.* **2006**, *45*, 3301; (c) Sutter, J. P.; Lang, A.; Kahn, O.; Paulsen, C.; Ouahab, L.; Pei, Y. *J. Magn. Magn. Mater* **1997**, *171*, 147.

17. (a) Chouteau, G.; Veyret-Jeandey, C. *J. Phys. (Paris)* **1981**, *42*, 1441; (b) Kobayashi, T.; Takiguchi, T.; Amaya, K.; Sugimoto, H.; Kajiwara, A.; Harada, A.; Kamachi, M. *J. Phys. Soc. Jpn.* **1993**, *62*, 3239; (c) Ishida, T.; Nogami, T.; Yoshikawa, H.; Yasui, M.; Iwasaki, F.; Takeda, N.; Ishikawa, M. *Chem. Phys. Lett.* **1995**, *247*, 7; (d) Nagashima, H.; Fujita, S.; Inoue, H.; Yoshioka, N. *Cryst. Growth Des.* **2004**, *4*, 19; (e) Fujita, W.; Takahashi, K.; Kobayashi, H. *Cryst. Growth Des.* **2011**, *11*, 575.

18. (a) Bogdanov, A. N.; Zhuravlev, A. V.; Rößler, U. K. *Phys. Rev. B: Condens. Matter Mater. Phys.* **2007**, *75*, 094425; (b) Coey, J. M. D. *Magnetism and Magnetic Materials*; Cambridge University Press: New York, 2010; (c) Sugano, T.; Goto, T.; Kinoshita, M. *Solid State Commun.* **1991**, *80*, 1021; (d) Teki, Y.; Itoh, K.; Okada, A.; Yamakage, H.; Kobayashi, T.; Amaya, K.; Kurokawa, S.; Ueno, S.; Miura, Y. *Chem. Phys. Lett.* **1997**, *270*, 573; (e) Kobayashi, T.; Takiguchi, M.; Amaya, K.; Sugimoto, H.; Kajiwara, A.; Harada, A.; Kamachi, M. *J. Phys. Soc. Jpn.* **1993**, *62*, 3239.

References for Chapter 5

1. Housecroft, C. E.; Sharpe, L. G. *Inorganic Chemistry* 3rd ed.; Pearson Prentice Hall: London, 2008.

2. (a) Bechgaard, K.; Cowan, D. O.; Bloch, A. N. *J. Am. Chem. Soc., Chem. Commun.* **1974**, 937; (b) Engler, E. M.; Patel, V. V. *J. Am. Chem. Soc.* **1974**, *96*, 7376; (c) Bendikov, M.; Wudl, F.; Perepichka, D. F. *Chem. Rev.* **2004**, *104*, 4891.

3. (a) Cordes, A. W.; Haddon, R. C.; Oakley, R. T.; Schneemeyer, L. F.; Waszczak, J. V.; Young, K. M.; Zimmerman, N. M. *J. Am. Chem. Soc.* **1991**, *113*, 582; (b) Andrews, M. P.; Cordes, A. W.; Douglass, D. C.; Fleming, R. M.; Glarum, S. H.; Haddon, R. C.; Marsh, P.; Oakley, R. T.; Palstra, T. T. M.; Schneemeyer, L. F.; Trucks, G. W.; Tycko, R.; Waszczak, J. V.; Young, K. M.; Zimmerman, N. M. *J. Am. Chem. Soc.* **1991**, *113*, 3559; (c) Cordes, A. W.; Haddon, R. C.; Hicks, R. G.; Oakley, R. T.; Palstra, T. T. M.; Schneemeyer, L. F.; Waszczak, J. V. *J. Am. Chem. Soc.* **1992**, *114*, 1729; (d) Cordes, A. W.; Haddon, R. C.; Oakley, R. T. In *The Chemistry of Inorganic Ring Systems*; Steudel, R., Ed.; Elsevier Science: Amsterdam, 1992; (e) Oakley, R. T. *Can. J. Chem.* **1993**, *71*, 1775.

4. (a) Brusso, J. L.; Derakhshan, S.; Itkis, M. E.; Kleinke, H.; Haddon, R. C.; Oakley, R. T.; Reed, R. W.; Richardson, J. F.; Robertson, C. M.; Thompson, L. K. *Inorg. Chem.* **2006**, *45*, 10958; (b) Robertson, C. M.; Leitch, A. A.; Cvrkalj, K.; Myles, D. J. T.; Reed, R. W.; Dube, P. A.; Oakley, R. T. *J. Am. Chem. Soc.* **2008**, *130*, 14791.

5. Robertson, C. M.; Leitch, A. A.; Cvrkalj, K.; Reed, R. W.; Myles, D. J. T.; Dube, P. A.; Oakley, R. T. *J. Am. Chem. Soc.* **2008**, *130*, 8414.

6. Beer, L.; Brusso, J. L.; Haddon, R. C.; Itkis, M. E.; Kleinke, H.; Leitch, A. A.; Oakley, R. T.; Reed, R. W.; Richardson, J. F.; Secco, R. A.; Yu, X. Y. *J. Am. Chem. Soc.* **2005**, *127*, 18159.

7. Leitch, A. A.; Yu, X.; Robertson, C. M.; Secco, R. A.; Tse, J. S.; Oakley, R. T. *Inorg. Chem.* **2009**, *48*, 9874.

8. Tse, J. S.; Leitch, A. A.; Yu, X. Y.; Bao, X. Z.; Zhang, S. J.; Liu, Q. Q.; Jin, C. Q.; Secco, R. A.; Desgreniers, S.; Ohishi, Y.; Oakley, R. T. *J. Am. Chem. Soc.* **2010**, *132*, 4876.

9. Lekin, K.; Winter, S. M.; Downie, L. E.; Bao, X. Z.; Tse, J. S.; Desgreniers, S.; Secco, R. A.; Dube, P. A.; Oakley, R. T. *J. Am. Chem. Soc.* **2010**, *132*, 16212.

10. Mito, M.; Komorida, Y.; Tsuruda, H.; Tse, J. S.; Desgreniers, S.; Ohishi, Y.; Leitch, A. A.; Cvrkalj, K.; Robertson, C. M.; Oakley, R. T. *J. Am. Chem. Soc.* **2009**, *131*, 16012.

References for Appendix A

1. Carlin, T. L. *Magnetochenistry*; Springer-Verlag: New York, 1986.

2. Frisch, M. J.; Trucks, G. W.; Schlegel, H. B.; Scuseria, G. E.; Robb, M. A.; Cheeseman, J. R.; Scalmani, G.; Barone, V.; Mennucci, B.; Petersson, G. A.; Nakatsuji, H.; Caricato, M.; Li, X.; Hratchian, H. P.; Izmaylov, A. F.; Bloino, J.; Zheng, G.; Sonnenberg, J. L.; Hada, M.; Ehara, M.; Toyota, K.; Fukuda, R.; Hasegawa, J.; Ishida, M.; Nakajima, T.; Honda, Y.; Kitao, O.; Nakai, H.; Vreven, T.; Montgomery, J., J. A.; ; Peralta, J. E.; Ogliaro, F.; Bearpark, M.; Heyd, J. J.; Brothers, E.; Kudin, K. N.; Staroverov, V. N.; Kobayashi, R.; Normand, J.; Raghavachari, K.; Rendell, A.; Burant, J. C.; Iyengar, S. S.; Tomasi, J.; Cossi, M.; Rega, N.; Millam, N. J.; Klene, M.; Knox, J. E.; Cross, J. B.; Bakken, V.; Adamo, C.; Jaramillo, J.; Gomperts, R.; Stratmann, R. E.; Yazyev, O.; Austin, A. J.; Cammi, R.; Pomelli, C.; Ochterski, J. W.; Martin, R. L.; Morokuma, K.; Zakrzewski, V. G.; Voth, G. A.; Salvador, P.; Dannenberg, J. J.; Dapprich, S.; Daniels, A. D.; Farkas, Ö.; Foresman, J. B.; Ortiz, J. V.; Cioslowski, J.; Fox, D. J. *Gaussian 09*, Revision A.02; Gaussian, Inc.: Wallingford CT, 2009.

3. *CAESAR*, Version 2; PrimeColor Software, Inc.: Cary, NC 1998.

4. Basch, H.; Viste, A.; Gray, H. B. *Theor. Chim. Acta* **1965**, *3*, 458.

5. Clementi, E.; Roetti, C. *At. Data. Nucl. Data Tables* **1974**, *14*, 177.

6. Ammeter, J. H.; Bürgi, H. B.; Thibeault, J. C.; Hoffmann, R. *J. Am. Chem. Soc.* **1978**, *100*, 3686.

7. Chai, C. L. L.; Armarego, W. L. F. *Purification of Laboratory Chemicals, 5th Ed.*; Butterwirth-Heinemann: New York, 2003.

8. Madsen, Z. *Z. Anorg. Allgem. Chem.* **1913**, *79*, 197.

9. Brauer, G. *Handbook of Preparative Inorganic Chemistry*; Academic: New York, 1963; Vol. 1.